Nanotribology investigations with classical molecular dynamics

Soheil Solhjoo

university of groningen / faculty of science and engineering / engineering and technology institute groningen

The research described in this thesis has been carried out at the Faculty of Science and Engineering, University of Groningen, The Netherlands, within the Advanced Production Engineering (APE) group of ENgineering and TEchnology institute Groningen (ENTEG).

ISBN 978-90-367-9921-8
eISBN 978-90-367-9920-1

Cover design: Soheil Solhjoo.
Description of the cover pictures: (***front***) The force-displacement curves of an adhesive contact between a spherical rigid cap (red) and a flat deformable substrate (blue). The displacement can be measured from the atoms' positions for, both, the indenter and the substrate. The solution of the JKR theory of adhesive contacts is shown for comparison. The details of the simulations can be found in Appendix B. (***back***) The atomistic contact between a randomly rough rigid surface, colored in blue-white-red based on the atoms' heights, and a flat deformable substrate, colored from blue (minimum value) to red (maximum value) based on the von Mises stress of the atoms. The vivid green and purple lines in the deformable substrate represent the generated dislocations. The details of the simulation can be found in Chapter 4.

university of groningen

Nanotribology investigations with classical molecular dynamics

PhD thesis

to obtain the degree of PhD at the
University of Groningen
on the authority of the
Rector Magnificus Prof. E. Sterken
and in accordance with
the decision by the College of Deans.

This thesis will be defended in public on

Friday 14 July 2017 at 11.00 hours

by

Soheil Solhjoo

born on 19 September 1984
in Shiraz, Iran

Supervisor
Prof. Y.T. Pei

Co-supervisor
Dr. A.I. Vakis

Assessment committee
Prof. E. van der Giessen
Prof. J.F. Molinari
Prof. L. Nicola

We strode and strolled, for years and years,
no matter how harsh the wind was.
As we reached the shores of the promised strand,
Mehri whispered
the names of the overseas butterflies.

No land in sight, I was on a boat,
gazing at the setting sun.
Sinking, I was, in my untapped desires.
A phoenix chanted,
and ever since, we're dancing as one.

This page is intentionally left blank.

Contents

This page is intentionally left blank.

Chapter 1

Introduction

1.1 Miniaturization of devices

Constructing and controlling devices at smaller scales has enabled much of the technological progress achieved in recent decades. For example, the invention of integrated circuits (ICs) enormously reduced the size of electronic devices, which, in turn, enabled the development of electronic devices such as laptops and smart phones with reduced size and weight, as well as vastly increased computational power. Moreover, advancements in constructing mechanical devices at the molecular and atomic scales, such as the famous nano-motor developed by the Groningen team of Ben Feringa [1], or nanoelectromechanical systems (NEMS), made it possible to have smaller machines for a number of potential applications, which are lighter, more accurate, more efficient, and, at the same time, cheaper and less power consuming.

Despite all the developments in system design at the nanoscale, however, contact, either normal or tangential, and other tribological phenomena, such as friction and wear that play a major role in the behavior of such systems, are less understood. The reason is essentially the different behavior of materials at the nanoscale relative to continuum descriptions. For instance, while surface forces are negligible at large scales, they become dominant at the nanoscale, and influence the functionality of nano-sized devices. Moreover, the detection of some of the systems' properties is beyond the resolution of current measuring devices, further restricting the applicability of continuum descriptions when considering atomistic level information. Surface roughness is a good example of this: a smooth surface could be considered as becoming increasingly rough as the scale becomes smaller and smaller.

1.2 Investigating nanocontacts

The system designing process can be extremely time consuming and expensive, if it is purely based on experimental results. Therefore, it is always useful to predict important system behavior before engaging in experiments. To do so, micro or larger length scale devices can be effectively modeled via continuum mechanics; however, as mentioned before, these models are not

the most suitable for studying atomic scale devices because of the discrete nature of atoms, which violates the assumption of continuity in continuum mechanics theories. This problem guided researchers towards atomistic computer simulation methods, and especially molecular dynamics (MD), which can be used for revealing the actual behavior of atomistic and molecular systems. In other words, these computer simulation methods can be considered as numerical experiments.

In the current work, the classical MD simulation method was utilized to explore the contact behavior of different types of nanocontacts, as well as the atomic scale roughness description of rough surfaces.

1.3 Continuum mechanics at the atomic scale

In early studies of nanocontacts, researchers tried to describe the contacts' behavior using continuum mechanics theories, e.g. see [2]. In 2005, Luan and Robbins [3] reported the breakdown of continuum mechanics contact theories at the atomic scale through examining the pressure distributions of different atomistic contacting tips. Since then, the applicability of continuum mechanics at the atomic scale has been under question. In another report, Mo et al. [4] showed that a new definition of contact area at the atomic scale is needed, which can also provide the same results as the continuum mechanics solutions.

Following the suggested approach by Mo et al. [4] for estimating the real contact area at the atomic scale, two new problems were exposed, namely the contact area of an individual atom, and the criterion for labeling two atoms as being in contact. These questions were addressed by different researchers [5-9]; however, no definitive answer has been provided so far.

In the current work, we have explored these issues, such as how the contacting atoms can be identified in fully adhesive and non-adhesive contacts, and how the contact area of an individual atom can be estimated. The results were compared with the corresponding continuum mechanics theories, and it was found that, as long as the systems are homogenous, and plastic deformation is not initiated, the contact behavior could be described using continuum mechanics.

1.4 Atomic scale roughness

The measured roughness of real surfaces cannot be directly used for

correctly describing atomic scale roughness, mainly because of the limitations on the lateral resolution of measuring devices. Due to this limitation, many studies on the contact of surfaces with nanoscale roughness adopted simplified deterministic surface topographies, while the contact of randomly rough surfaces was investigated as well by means of MD simulations. The topography of atomic scale roughness, however, has not been fully investigated in the literature.

In this work, we have investigated the surface roughness of atomistic gold substrates, and its dependence on different parameters, such as crystalline directions and temperature. The results showed the limitations and problems in defining surface roughness at the atomic scale. Moreover, possible remedies for generating pseudo-stable atomistic rough surfaces were introduced and discussed.

1.5 Limitations and errors in molecular dynamics

Molecular dynamics (MD) is an atomistic computer simulation technique for studying the time-evolution of N discrete interacting atoms and molecules in a given system. In classical MD, which is the tool used in this thesis, the trajectories of atoms and molecules are determined by numerically solving Newton's equations of motion, where forces between the particles are calculated using interatomic potentials and molecular mechanics force fields.

In MD studies, the systems typically consist of a vast number of interacting atoms, where each of atom can require up to 100 operations for the calculation of its force at each time step [10]. Considering a typical time step of 1~10 fs, MD simulations are computationally heavy. This limitation practically affects, both, the size of the designed system and the simulated time of the process, to be in the scales of nanometers and nanoseconds, respectively.

Moreover, the limitation on the computational resources affects the design of the system and process as well. For example, consider that approximately 1 μs can be simulated per day for a medium-size system with 10^5 atoms. In order to study the nano indentation process, one may try to mimic the nanoscale atomic force microscopy (AFM) experiment, in which the tip advances at a speed of ~1 μm/s. This results in ~1 pm of the tip's movement within a simulation day, which is shorter than the size of a single atom. This example [10] explains why the designed processes are significantly faster than the corresponding real experiments; for instance, in order to simulate a frictional process, the moving speed in MD is typically as high as 0.1~100 m/s, which cannot be easily compared with macroscopic sliding experiments.

Furthermore, the limitation on the number of atoms in a simulation results in finite-size effect: for example, in the simulation of an indentation test, the stress fields would exceed the depth of the substrate and interact with the rigid supporting layer. In order to solve this problem, different methods can be employed, such Green's function MD (GFMD) [11], smartblock MD [12], or by coupling classical MD with other techniques such as the finite element method (FEM). In this thesis, however, classical MD was the only tool used, and the analyses were limited prior to the point that the finite size started to affect the results.

In addition to the abovementioned limitations, MD simulation, which is a numerical method, inherently suffers from round-off and truncation errors. Moreover, a discretization error may be involved as well; for example, in order to save computational resources, tabulated versions of the interatomic potentials are commonly used in the simulations, instead of their continuous functions. These errors make long MD simulations mathematically ill-defined, due to cumulative errors; however, these errors can be minimized by a proper selection of algorithms and parameters.

1.6 Outline of the thesis

The core of this thesis can be divided into three parts, exploring different problems for describing and analyzing atomistic simulations of nanocontacts. In Chapters 2 and 4 and Appendices B and C, the applicability of continuum mechanics theories for describing nanocontacts is presented. In Chapter 3 and appendix A, measuring the contact area is exclusively discussed, although this problem has been addressed in almost all chapters. Finally, the surface roughness at the atomic scale is investigated in Chapter 5. The following is a detailed outline of the chapters and appendices of this thesis.

1.6.1 Chapters

- In **Chapter 2**, the nanocontacts of different single spherical asperities with fcc-nickel substrates were investigated. The single asperities were modeled in three different configurations/types: a non-atomistic repulsive particle and two atomistic particles generated from fcc-nickel, and bcc-iron. The mechanical behavior of the nanocontacts was studied, and the adhesive ones were compared with the corresponding continuum mechanical models. The non-adhesive

contact was compared with the Hertzian solution. The plastic deformations in the systems were also studied with characterizations of the dislocations generated in the processes. In this manner, this chapter explores further the breakdown of continuum reported in previous studies.

- In **Chapter 3**, different types of atomistic contacts were studied in order to present a reliable method of calculation for the real contact area in the presence of adhesion. Previously published methods, including those discussed in Chapter 2, were reviewed and their advantages and disadvantages were discussed. Based on this discussion, a number of critical parameters were redefined so as to find a more accurate answer to the critical question of how contact should be defined at the atomic scale.

- In **Chapter 4**, atomistic non-adhesive contacts were studied, and the results were analyzed and compared with relevant continuum models. First, a number of single asperity contacts were investigated, which resulted in a differentiation between the definitions of interacting and contacting atoms. Moreover, through analyzing the results in the context of continuum contact mechanics models, it was shown that, for indentations exceeding a finite indentation depth, the indentation responses tended to those described by continuum theories. Furthermore, two types of rough surface contacts were simulated, building on the single asperity contact investigation. The results showed that the simulation results were comparable to those of continuum mechanics models.

- In **Chapter 5**, the surface roughness of various randomly rough atomistic blocks of pure gold was investigated. Following the generation of the blocks, these were equilibrated, and the effects of different parameters, such as temperature and crystal orientation, on the equilibrated blocks were studied. The results showed that the atomistic substrates cannot retain their sharp steps and edges, and the surfaces were smoothened due to thermodynamic considerations. Moreover, two different methods were proposed for generating physically meaningful surface topographies at the atomic scale.

- In **Chapter 6,** the concluding remarks of the thesis were presented.

1.6.2 Appendices*

- In **Appendix A**, the frictional behavior of a pair of contacting rough surfaces with and without lubricant molecules was studied. The results showed the drop of shearing force by increasing the volume of the lubricant. Moreover, it was found that the stability of the system would be higher for a larger volume of lubricant.

- In **Appendix B**, the normal contact between an atomistic spherical cap and a flat substrate was investigated. The main difference between the studied system in this appendix with the ones in Chapters 2 and 4 was the description of the interacting forces between the contacting bodies. While Chapters 2 and 4 deal with fully adhesive and non-adhesive contacts, respectively, Appendix B addresses contacts with limited adhesion: the adhesion was low enough to prevent the plastic deformation and atom transfer process. The systems were analyzed with the methods discussed in Chapter 3, and the results were shown to be closely comparable to the continuum mechanics models. Moreover, a distinction between indentation and penetration was proposed, and its importance for analyzing nanocontacts was discussed.

- In **Appendix C**, the non-adhesive case of sphere-on-flat problem was studied by applying two different interacting potential energies between the bodies. The presented results verify the dependence of the indenter's response on the interacting potential energy.

- In **Appendix D**, a method for analyzing the contact-induced stress fields is introduced and discussed. The materials of Chapter 4 were used for analysis in this appendix. Using this method, the contacting systems were analyzed, and their contact behavior was studied only before the contact-induced stress fields reached the boundaries of the contacting bodies.

---

* Appendices A and B present some early results on frictional and adhesive normal contacts, respectively. Because our investigations on these topics are still ongoing, we have decided not to present them as separate chapters.

- In **Appendix E**, the relation between the fractal dimension (D_S), the Hurst exponent (H), and a two-segment formula for describing the power spectral densities (PSD) of rough surfaces was presented. This model was used in Chapter 5. Following the discussion in this appendix, the PSD exponents were not decomposed to D_S and H.

- In **Appendix F**, a simple formula for the calculation of spectral moments of a two-segment PSD model was derived. Moreover, it was discussed how the parameters of the two-segment PSD model can be defined in order to generate a rough surface with a desired value of RMS roughness. This method was directly used for generating most of the rough surfaces of Chapter 5.

- In **Appendix G**, the RMS gradient of a limiting case for {100} planes in an fcc crystal structure was calculated. The nominally flat rough surface was analyzed by applying a lateral resolution of a_0. This was done for comparison between this maximum limiting case and the calculated values of the rough surfaces in Chapter 5

- In **Appendix H**, the roughness of a molten gold substrate based on the capillary wave theory was calculated. Then, the result was compared with the findings of Chapter 5. Moreover, it was shown that the noted increase of roughness at higher temperatures was in agreement with this theory.

1.7 Nomenclature

The common notations in the field were used for the thesis; however, a number of new parameters were introduced, while, where necessary, new alternative symbols were used for known parameters. These parameters can be divided into the following types:

1- Parameters for atoms:
   - a_{c} contacting atoms (for identification)
   - a_{nc} non-contacting atoms (for identification)
   - N_{ca} number of contacting atoms

2- Parameters for area:
   - A_{real} real contact area
   - A_{nom} and A_0 nominal contact area
   - $A_{\mathrm{nc}a}$ projected area of all non-contacting atoms
   - A_{pc} projected area of all contacting atoms
   - A_{rpc} relative projected contact area ratio, defined as $A_{\mathrm{rpc}} = A_{\mathrm{pc}}/A_0$

3- Parameters for size and distances:
   - V_a, A_a, d_a, r_a volume, projected area, diameter, and radius of an individual atom, respectively
   - d_{c} contact distance

1.8 List of scientific output

1.8.1 Peer-reviewed journal papers

- Müser, M.H., W.B. Dapp, R. Bugnicourt, P. Sainsot, N. Lesaffre, T.A. Lubrecht, B.N.J. Persson, K. Harris, A. Bennett, K. Schulze, S. Rohde, P. Ifju, G.W. Sawyer, T. Angelini, H. Ashtari Esfahani, M. Kadkhodaei, S. Akbarzadeh, J.-J. Wu, G. Vorlaufer, A. Vernes, S. Solhjoo, A.I. Vakis, R.L. Jackson, Y. Xu, J. Streator, A. Rostami, D. Dini, S. Medina, G. Carbone, F. Bottiglione, L. Afferrante, J. Monti, L. Pastewka, M.O. Robbins & J.A. Greenwood, (2017) Meeting the contact mechanics challenge, Tribology Letters, 65:118.
- S. Solhjoo, A.I. Vakis, (2017) Surface roughness of gold substrates at the nanoscale: an atomistic simulation study, Tribology International, 115:165-178.
- S. Solhjoo, A.I. Vakis, (2016) Continuum mechanics at the atomic scale: Insights into non-adhesive contacts using molecular dynamics simulations, Journal of Applied Physics, 120:215102.
- S. Solhjoo, A.I. Vakis, (2015) Definition and detection of contact in atomistic simulations, Computational Materials Science, 109:172-182.
- S. Solhjoo, A.I. Vakis, (2015) Single asperity nanocontacts: comparison between molecular dynamics simulations and continuum mechanics models, Computational Materials Science, 99:209–220.

1.8.2 Peer-reviewed conference papers

- S. Solhjoo, A.I. Vakis, Molecular dynamics simulations of rough contact with fractal and statistical surface generation, ASME 12th Biennial Conference on Engineering Systems Design & Analysis (ESDA), Copenhagen, Denmark, 25-27 June 2014.

1.8.3 Conference (extended) abstracts

- S. Solhjoo, A.I. Vakis, Lubricated normal and sliding contact of fractal rough surfaces at the atomic scale, The international conference on understanding and controlling nano and mesoscale friction (COSTnanoTribo), Istanbul, Turkey, 22-26 June 2015.

- S. Solhjoo, A.I. Vakis, Normal contacts of lubricated fractal rough surfaces at the atomic scale, TriboUK 2015, Loughborough, England, 16-17 April 2015.

1.8.4 Presentations (oral/poster presentation)

- S. Solhjoo, A.I. Vakis, Atomic scale roughness of gold substrates, Micro/Nanoscale Models for Tribology workshop, Leiden, the Netherlands, 30 January – 3 February 2017. (Poster)
- S. Solhjoo, A.I. Vakis, Continuum contact mechanics theories at the atomic scale: an investigation on non-adhesive contacts, Micro/Nanoscale Models for Tribology workshop, Leiden, the Netherlands, 30 January – 3 February 2017. (Poster)
- S. Solhjoo, A.I. Vakis, Non-adhesive contacts: the application of continuum theories at the atomic scale, 2nd ENTEG autumn meeting, Haren, the Netherlands, 6 October 2016. (Poster)
- S. Solhjoo, A.I. Vakis, The Area of Contact for Non-Adhesive Rough Surfaces: Comparison between MD and Persson's Model, 8th International Conference on Multiscale Materials Modeling, Dijon, France, 9-14 October 2016. (Oral Presentation)
- S. Solhjoo, A.I. Vakis, Lubricated normal and sliding contact of fractal rough surfaces at the atomic scale, The international conference on understanding and controlling nano and mesoscale friction (COSTnanoTribo), Istanbul, Turkey, 22-26 June 2015. (Oral Presentation)
- S. Solhjoo, A.I. Vakis, Normal contacts of lubricated fractal rough surfaces at the atomic scale, TriboUK 2015, Loughborough, England, 16-17 April 2015. (Oral Presentation)
- S. Solhjoo, A.I. Vakis, Nanotribology: a molecular dynamics simulation approach, 1st ENTEG autumn meeting, Haren, the Netherlands, 8 October 2015. (Invited Talk)
- S. Solhjoo, A.I. Vakis, Investigations of atomic scale contacts with classical MD, Forschungszentrum Jülich, Germany, 25 September 2015. (Invited Talk)
- S. Solhjoo, A.I. Vakis, Dry sliding contact between fractal and statistical rough surfaces at the atomic scale, DGM European Symposium on Friction, Wear & Wear Protection, Karlsruhe, Germany, 6-8 May 2014. (Poster)

Chapter 2 *

Single asperity nanocontacts: comparison between molecular dynamics simulations and continuum mechanics models

Using classical molecular dynamics, atomic scale simulations of normal contact between a nominally flat substrate and different atomistic and non-atomistic spherical particles were performed to investigate the applicability of classical contact theories at the nanoscale, and further elucidate the phenomena that govern the perceived breakdown of continuum in nanocontacts. The Hertz elastic contact model was shown to sufficiently capture the results of molecular dynamics simulations prior to the onset of plastic deformation for non-adhesive contacts. Moreover, the results show that the slipping of dislocations was the deformation mechanism responsible for force drops during loading; prior to slipping, however, the plastic deformation was identified to be reversible. For adhesive contacts, the corresponding surface energies were calculated via molecular dynamics simulations and validated with values reported in the literature. The contact force and radius, as well as the contact stress distribution and dislocation propagation were then investigated in detail. Moreover, the results were compared to the limiting cases of the Johnson-Kendal-Roberts and Derjaguin-Muller-Toporov continuum models. The atomistic systems showed deviations from the classical models, which could be related to energy loss and changes in the effective work of adhesion, as well as the anisotropic properties of the atomistic systems. The findings of this chapter support the published literature on the subject, and further contribute to our understanding of discrepancies between atomistic and continuum descriptions of contact.

* This chapter has been originally published in Computational Materials Science **109** (2015) 172–182.

2.1 Introduction

Nanotribology is an interdisciplinary field of research that studies the friction, adhesion, lubrication and wear of nanocontacts. At the nanoscale, surface forces become dominant and they can influence the functionality of micro- and nano-sized devices. Similarly, contact is initiated at the atomic scale and is particularly important in modern technologies such as micro- and nano-electro mechanical devices, atomic force microscopy, and magnetic storage devices. Therefore, studying nanocontacts is a key step towards understanding the multiscale properties of contact phenomena.

In general, the structure of surfaces is random at the atomic scale with roughness occurring even for highly smooth surfaces. In order to isolate surface roughness from other physical parameters that affect tribology, many studies have focused on the contact of individual asperities with perfectly smooth surfaces [13]. A reason why single asperity studies have been so widely used is that deformations at the contacting interface can be described by continuum mechanics models [4]. In the present chapter, the focus is on classical single asperity studies to investigate whether these remain valid at the atomic scale. More specifically, the results were compared with the limiting cases of Johnson-Kendall-Roberts (JKR) [14] and Derjaguin-Muller-Toporov (DMT) [15] models.

Through the last decades, many researchers have applied theories of continuum contact mechanics to nanotribology measurements in order to determine fundamental parameters and processes at play in nanoscale contacts via experiments [16-19] and simulations [20-22]. Luan and Robbins [3, 23] examined nanocontacts via molecular dynamics (MD) simulations for different contacting tip geometries. They showed that there are deviations between atomistic behavior and continuum theory. In summary, they discussed that any realistic interactions lead to a gradual increase in repulsion with separation rather than an idealized hard-wall interaction. Also, surface roughness, which always exists in any discrete atomistic surface, results in pressure distributions on the surface that deviate from those described in continuum theory. Moreover, roughness has an influence on the work of adhesion. Besides these deviations, they also showed that friction theories do not hold at the nanoscale and, therefore, concluded that continuum models cannot correctly capture the behavior of nanocontacts. Later, Mo et al. [4, 5] showed that the break-down of single-asperity theories of friction depends on the method with which the contact area is measured. In continuum mechanics, the contact area is defined by the edge of the contact zone, or the area of the

asperity A_{asp}. However, because of the roughness at the atomic scale, the real contact area is different than A_{asp}. They defined the real contact as:

$$A_{\mathrm{real}} = N_{ca} A_a, \tag{2.1}$$

where N_{ca} is the number of contacting atoms defined by the atomic distances between the substrate and the tip, and A_a being the average surface area per atom [4, 5]. The conditions in which continuum models break down are still under investigation, and this chapter aims to add to the study of the correspondence between continuum theory and atomistic behavior.

This chapter presents the results of the contact between different single spherical asperities and fcc-nickel substrates.

2.2 A short review of elastic contact theories

The first model for non-adhesive elastic contacts was published by Hertz [24] (e.g., see [25] for a review). This model describes the contact behavior of two contacting parabola, resulting in an elliptical contact area. For a simpler case of contact between a sphere of radius R and a half-space penetrated by a depth d_p, which forms a circular contact area of radius r, the Herz model is still valid. Assuming $d \ll R$, the following holds: $r^2 = Rd$. Hertz derived the pressure distribution of the form $p_{(l)} = p_0(1 - (l/r)^2)^{1/2}$, where p_0 is the maximum compressive pressure, with l being the radial distance between 0 (at the center the contact) and r (the contacting radius). Figure 2.1 (a) schematically illustrates a deformed sphere and pressure distribution for the Hertzian solution. The contact area radius r can be obtained as a function of normal load $F_\perp$:

$$r^3 = \frac{3}{4}\frac{RF_\perp}{E^*}, \tag{2.2}$$

with

$$E^* = \left(\frac{1-\nu_1^2}{E_1} + \frac{1-\nu_2^2}{E_2}\right)^{-1}, \tag{2.3}$$

where E_1 and E_2 are the elastic moduli, and ν_1 and ν_2 are the Poisson's ratios associated with each body. E^* is known as the reduced Young's modulus or contact elastic modulus. This model has been extensively studied in Chapter 4.

In 1971, Johnson et al. [14] proposed a new theory (JKR) that accounted for adhesion between the contacting bodies. This work was motivated by

experimentally measured contact areas that were larger than the areas predicted by Hertzian theory at low loads, and by the observation of a finite contact area at zero applied loads. In this approach, it was suggested that a tensile pressure distribution can be maintained at the contact area at zero separation, while neglecting the adhesion force outside the contact circle. They then proposed a pressure distribution of $\acute{p}_{(l)} = -\acute{p}_0(1-(l/r)^2)^{-1/2}$, corresponding to the attractive adhesive force. This term was added to the pressure $p_{(l)}$ given by Hertzian theory. The deformation and pressure distribution of an elastic sphere in contact with a rigid plane are shown in Figure 2.1 (b), for the JKR solution. Johnson et al. [14] derived the contact radius as:

$$r^3 = \frac{3}{4}\frac{R}{E^*}\left(F_\perp + 3\pi R\Gamma + \sqrt{6\pi R\Gamma F_\perp + (3\pi R\Gamma)^2}\right), \tag{2.4}$$

where Γ is the work of adhesion. This theory predicts a maximum tensile force of $-3/2\,\pi R\Gamma$, known as the pull-off force (F_{po}), necessary to detach the bodies.

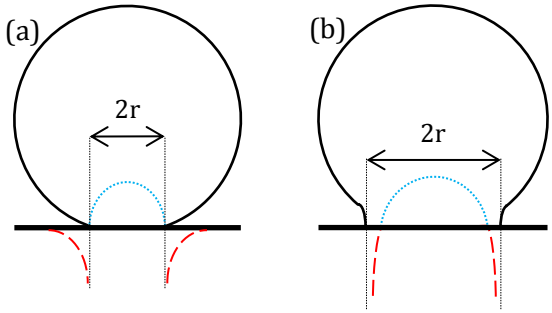

Figure 2.1 Surface traction and the pressure distribution of a elastically deformed sphere regarding (a) Hertz and DMT, and (b) JKR solutions. The dotted blue lines (above the flat surface) show the compression, and the dashed red lines (under the flat surface) show the tension. The tension lines in (a) are based on DMT solution.

Subsequently, Derjaguin et al. [15] formulated their theory (DMT) to incorporate the effect of adhesion in contact by introducing the attractive forces outside the contact area (Figure 2.1 (a)). They showed that the deformed contact profile remained the same as in Hertzian theory, but with an overall higher load due to the adhesion force (F_{ad}) acting as a dead weight. They showed that the pull-off force is equal to $-2\pi R\Gamma$, and is reached at zero contact radius; the same conclusion was reached with the Bradley model for

rigid contacts [26]. Also, they found that the adhesive force gradually decreases to $-\pi R\Gamma$ as a function of displacement. Muller et al. [27] later showed that the contact radius under a zero load can be calculated for the DMT model by:

$$r_0^3 = \frac{3}{2}\frac{\pi R^2 \Gamma}{E^*}, \tag{2.5}$$

where r_0 is the contact radius at $F_\perp = 0$. Assuming constant adhesive force ($F_{\text{ad}} = F_{\text{po}}$), Maugis [28] showed that the DMT theory can be estimated by:

$$r^3 = \frac{3}{4}\frac{R}{E^*}(F_\perp + 2\pi R\Gamma). \tag{2.6}$$

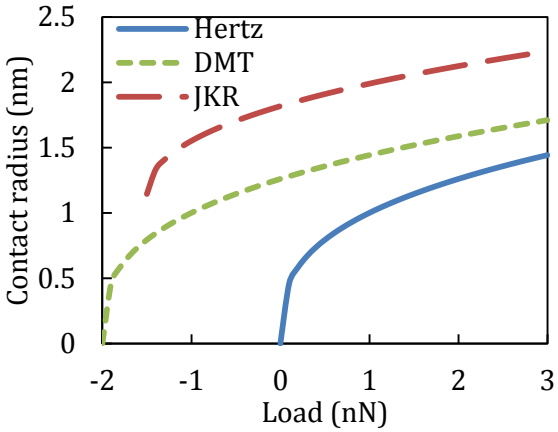

Figure 2.2 The contact radius vs load curves, for Hertz, DMT and JKR models, plotted by setting $E^* = 3/4$ GPa, $R = 1$ nm, and $\Gamma = \pi^{-1}$ N/m.

Figure 2.2 illustrates the different values of the contact radius between a spherical asperity and a flat surface with the Hertz, JKR and DMT solutions. In 1976, Tabor [29] analyzed both adhesive models, and suggested the following relation for the pull-off force:

$$F_{\text{po}} = -3/2\,\pi R\Gamma\phi(\mu), \tag{2.7}$$

where ϕ is a function of $\mu = \left(R\Gamma^2/E^{*2}\, r_{\text{E}}^3\right)^{1/3}$, with r_{E} being the equilibrium interatomic distance. The variable μ, thereafter known as the Tabor parameter, is the ratio of the neck height formed in the JKR model over the equilibrium interatomic distance. Higher values of μ imply the applicability of

the JKR model, while the DMT model holds for small values of μ. After some debate [30-33], Muller et al. [34] concluded that the two theories are limiting cases of a more general approach. It is known that the function $\phi(\mu)$ changes monotonically in the range between 1 (for the JKR limit) and $4/3$ (for the DMT limit); however, the function itself is not rigorously defined. It is possible to rewrite (2.7) as $\chi = -F_{\mathrm{po}}/\pi R\Gamma$, and for the DMT and JKR limits, χ would be 2 and 1.5, respectively. Muller et al. [27] used the Lennard-Jones potential [35] to formulate the first elastic solution of adhesive contact (MYD) for a continuous variation of μ between the limits of the JKR and DMT models via a numerical method. Maugis [28] was the first to model elastic adhesive contacts for the whole range between the JKR and DMT limits.

All the above theoretical models deal with the contact of two homogenous, isotropic, axisymmetric contacting bodies. In addition, the solutions are driven by the following simplifying assumptions [25]:

a- surfaces are continuous and perfectly smooth,
b- strains are small enough for linear elasticity to be valid, and
c- surfaces are frictionless.

It should be noted that any deviation from these assumptions has an impact on the correlation between the models and experiments. For instance, for general anisotropic materials, there is no straightforward formula to estimate the value of the reduced Young's modulus which is an essential part of continuum contact theories [36].

2.3 Simulation methodology

2.3.1 Overview of numerical experiments

A series of classical molecular dynamics (MD) simulations were utilized to study the nanocontacts between spherical single asperities and an atomically flat substrate, performed using the large-scale atomic/molecular massively parallel simulator (LAMMPS) [37]. The equations of motion were numerically solved using the velocity-Verlet algorithm [38] with an integration step size of 10 fs. This was selected from NVE-ensemble pre-test simulations as the largest time step that did not exhibit energy drift. Using the Berendsen thermostat algorithm [39], the temperature was kept constant at 300 K. Also, the [100], [010], and [001] crystallographic directions were selected as the x, y, and z axes for the generation of all atomistic bodies. Moreover, the visualizations, dislocation analyses, and other atomistic related post processing steps were

done by the open visualization tool (OVITO) [40], and the crystal analysis tool (CAT) [41-44]. The various simulations performed in this study are summarized in Table 2.1.

The systems were generated from fcc-nickel and bcc-iron atoms. The integrated embedded-atom method potential database formulated and developed by Zhou et al. [45] was used for calculating the potential energy of the system. The elastic constants of the potential energies at 300 K were calculated via LAMMPS, and used for estimating the values of Young's modulus and Poisson ratio via Hill's approximation [46]. The results are summarized in Table 2.2.

Two categories of simulations were performed: one called forced particles (see section 2.3.2), and the other called free particles (see section 2.3.3). The systems with forced particles were simulated to extract the force-displacement and force-contact area data, while the systems with free particles were simulated to measure the contact area under zero externally applied force. All particles had a radius of 30 Å. The particles were made by cutting a sphere from a crystal that was aligned with the substrate, resulting in a terraced geometry. This geometry can be seen in Figure 2.3, which shows the "forced particles" described in more detail below. This kind of stepped atomic structure for nanoparticles has a good correspondence to experiments reported in the literature [47]. It should be mentioned that a slight tilt in the steps could result in a very different pressure distribution [23].

2.3.2 Forced particles

Three different single asperities were simulated: a non-atomistic repulsive asperity, and two atomistic ones with different crystal structures. In the non-atomistic case, the asperity was placed adjacent to the top of the substrate. However, for the atomistic asperities, the clearance between each asperity and the substrate was slightly larger than the potential's cutoff radius. After equilibration, the particles were moved along $[00\bar{1}]$ toward the substrate in a displacement control mode. The movement for the non-atomistic asperity was 10 Å from its center with a velocity of 1 m/s. In the case of atomistic asperities, the rigid layer was moved for 15 Å from its initial position with a velocity of 10 m/s; the latter was imposed due to the processing time limitations of MD. Then, the particles moved upward until the force between the particle and the substrate became zero. There was no relaxation time during or between the loading and unloading processes.

Table 2.1 A schematic summary of the numerical experiments, and their placement in the chapter:

Non-atomistic indenter: contact with no adhesion	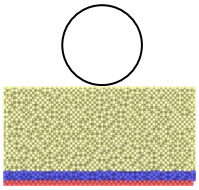	2.5.1 Contact with no adhesion
Surface energy: for both Ni and Fe along the {100} planes.	Phase A: 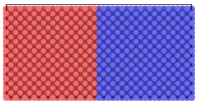 Phase B: 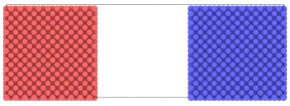	2.5.2 Contacts with adhesion
Free particle: for both Ni and Fe.	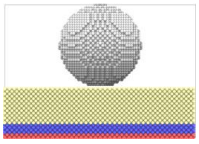	2.5.2.1 Contacts of free particles
Forced particle: for both Ni and Fe	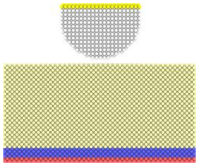	2.5.2.2 Contacts of forced particles: Iron 2.5.2.3 Contacts of forced particles: Nickel

Table 2.2 The calculated elastic properties for nickel and iron for the used EAM potentials [45]. All values but the Poisson ratios are reported in the scale of GPa.

	C_{11}	C_{12}	C_{14}	E	ν
Ni	216.7	145.1	117.9	218.1	0.30
Fe	221.2	146.6	104.1	182.6	0.32

The geometric non-atomistic asperity was modeled as a purely repulsive soft (in reference to its force field) sphere. The interaction potential between the asperity and the substrate atoms was limited to distances $r \leq R$, where r is the distance from the atom to the center of the asperity, and R is the radius of the asperity. The geometrical asperity exerts a force of magnitude $-K(r-R)^2$ [48], where K is a force constant related to the effective stiffness of the asperity that was set to 5 eV $\cdot$ Å^{-3} [49].

The other two asperities were generated from atomistic nickel and iron. Each asperity was divided into two regions: the highest two atomic layers were laterally fixed and were only allowed to move along the z axis, thereby controlling the movement of the asperities. Below this section, a cylinder with a height of four atomic layers connected to a hemisphere was filled with non-constrained atoms. Figure 2.3 illustrates the geometry and atomistic representation of these two asperities.

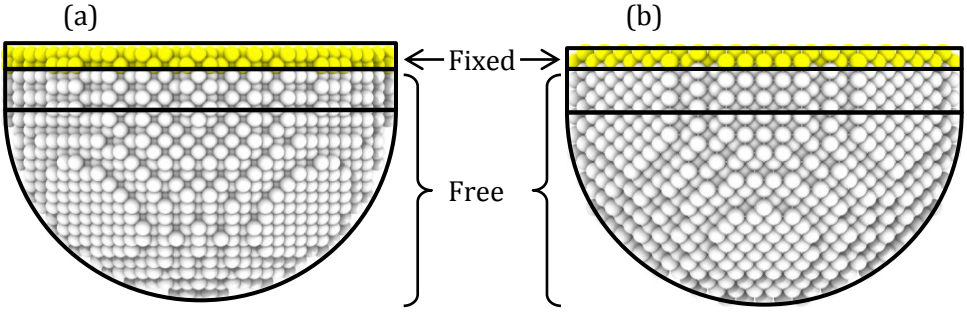

Figure 2.3 Atomistic representation of the (a) fcc-nickel, and (b) bcc-iron particles.

2.3.3 Free particles

Using the continuum models, it is possible to predict the contact area between two bodies at a zero external load. To do this, two spherical particles were generated from nickel and bcc-iron and were allowed to come into contact with the substrate under zero external force. The atoms were not constrained, and each particle was placed 2 Å above the substrate. Since the EAM potentials' cutoff radii were ~6 Å, the particles were within the range of interatomic interactions with the substrate. The simulations were run for1 ns

with zero applied external force. The results are discussed in section 5.2.2, and used through the discussion of forced adhesive particles.

2.3.4 Substrates

Different nanocontacts were simulated with various single asperity representations, and using two different substrates comprised of a single fcc crystal generated from nickel atoms. The substrates have dimensions of $40a_0 \times 40a_0 \times 20a_0$ and $40a_0 \times 40a_0 \times 10a_0$, for forced and free particles, respectively, where $a_0 = 3.52$ Å is the lattice constant for nickel. The size was validated through pretest simulations as being large enough to obtain reliable results; specifically, it was verified that the resulting stress fields were fully enclosed within the substrate material volume. Periodic boundary conditions (PBCs) were applied in the lateral directions. At the bottom, the last two atomic layers were fixed, resembling a rigid substrate. The next four atomic layers were assigned to be the thermostatic layer, and the remaining atoms were not constrained.

2.3.5 Evaluation of work of adhesion

The work of adhesion Γ is the energy change of bringing a unit area of a phase A into contact with a unit area of a phase B in vacuum [50]. These two phases may be the same or correspond to different materials. By definition, $\Gamma = \gamma_A + \gamma_B - \gamma_{AB}$, where γ_A and γ_B are the surface energies of phases A and B, respectively, and γ_{AB} is the energy of their interface. If the phases are the same, then $\gamma_{AB} = 0$.

Continuum models require a value for Γ. This value can be calculated via MD simulations by subtracting the energy per unit area of the two atomically flat substrates in equilibrium with zero applied force (phase A) from the energy per unit area of the two substrates at infinite separation (phase B). To do so, a set of two simulations is needed [51]. In the first, two cubic atomic blocks, each with a size of $10a_0 \times 10a_0 \times 10a_0$, were constructed side by side. In the second simulation, there was a gap of $10a_0$ between the two blocks. The PBCs were applied in lateral directions. Each simulation was run for 150 ps. It should be noted that in these simulations, (001) surfaces formed both the interface and the generated free surfaces.

The above simulations were done for nickel and iron systems. However, in order to construct a system for a nickel/iron pair in the defined coordinate

system, the lateral lengths of the simulation box should be equal to the length of 287 unit cells of nickel and 352 unit cells of iron to ensure that the two are equal†; otherwise, the PBCs cannot be applied in the lateral directions without introducing crystallographic defects to the system. Instead of running such a huge simulation, it is possible to estimate the value of γ_{AB} from $(\sqrt{\gamma_A} - \sqrt{\gamma_B})^2$ [50]. Therefore, in general, the work of adhesion can be expressed as $\Gamma = 2\sqrt{\gamma_A \gamma_B}$. If A = B, then $\Gamma = 2|\gamma_A|$, where the $|\gamma_A|$ is the absolute value of the surface energy.

2.4 Contacting atoms and contact area

Mo et al. [4, 5] showed that the calculation of the real contact area is important in the study of contacts at the atomic scale. However, the calculation of the contact area is very challenging at this scale. The difficulty comes from various reasons, the most important of which are the detection of contacting atoms, and the definition of the area of contacting atoms.

Assuming that atoms can be represented as rigid spheres, their radii can be defined based on their crystallographic packing factors. There are 4 and 2 atoms in each fcc and bcc unit cell with packing factors of 0.74 and 0.68, respectively. Therefore, the atomic volume (V_a) in these two crystal structures can be defined as $0.74 \times a_0^3/4$ and $0.68 \times a_0^3/2$ for fcc and bcc, respectively. The projected atomic real area then can be defined as $A_a = \left(3\sqrt{\pi}/4\, V_a\right)^{2/3}$. Interaction forces between neighboring atoms vary with distance. In this work, a contact distance d_c was used to define atoms that were in contact; that is $d_c = a_0/2 + r_a$, where $r_a = (3/(4\pi)\, V_a)^{1/3}$ is the atomic radius. For the system with nickel and iron atoms, the mean value of the contact distances of nickel and iron was adopted as the contact distance between those different atoms. Hence, two atoms whose distance was equal to or smaller than the corresponding were defined as being in contact. The average of the contact areas of the contacting particle and substrate was reported as the contact area.

† The number of necessary unit cells can be found from $N_{Ni}\, a_{0,Ni} = N_{Fe}\, a_{0,Fe}$. Furthermore, it should be noted that N should be an integer, and not a fraction.

2.5 Results and discussion

2.5.1 Contact with no adhesion

The force-displacement ($F-d$) curves of the contact of the non-atomistic asperity are shown in Figure 2.4. The curve shows a sequence of drops that are directly related to plastic deformations. The first drop occurred at a depth of ~4.8 Å, and is an indication of the onset of plasticity. At this point, the elastic stress under the indenter was partially relieved by plastic deformation.

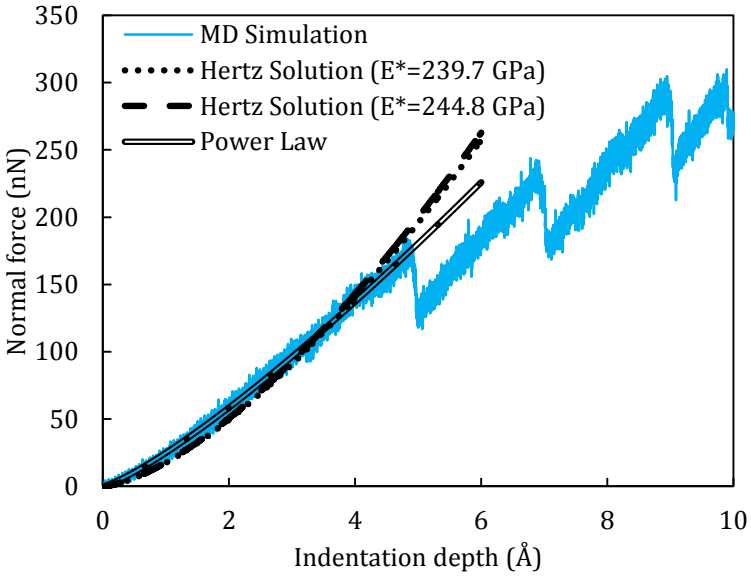

Figure 2.4 The force-displacement curve of the non-atomistic repulsive contact. For the Hertz solutions, $E^* = 239.7$ GPa and $E^* = 244.8$ GPa were obtained from the calculated elastic properties and fitting the Hertz formula to the simulation results, respectively.

In order to confirm that the deformation before the indentation depth of 4.8 Å was reversible, the crystal structure of the system was analyzed via an additional simulation. In this simulation, the non-atomistic particle indented the substrate to a depth of 4.5 Å, and was then returned to its original position. All other parameters of the system were the same as before. Figure 2.5 shows the dislocation generations during this process. It is found that, at a depth of

3.5 Å, the nucleation of dislocations was started, and the process was continued to a depth of 4.5 Å. These generated dislocations were mainly Shockley partials with Burgers vectors $\vec{\mathbf{b}} = (a_0/6)[\bar{2}\bar{1}1]$ and $\vec{\mathbf{b}} = (a_0/6)[2\bar{1}1]$. In two points, these dislocations interacted with each other as follows:

$$\frac{a_0}{6}[\bar{2}\bar{1}1] + \frac{a_0}{6}[2\bar{1}1] = \frac{a_0}{3}[0\bar{1}1]. \quad (2.8)$$

The newly generated dislocations are stair-rod sessile, known as Lomer-Cottrel locks [52] with their Burgers vectors on, both, (111) and $(\bar{1}11)$ planes. These locks act as strong barriers; however, their disappearance in further indentations can be explained by the unzipping mechanism [53]. As the next step, the indenter was moved to its initial position, in which all dislocations were removed from the crystal structure at an indentation depth of 2.5 Å, as shown in Figure 2.5 (h). By analyzing the crystal structure at the end of the unloading process, it was found that the system returned to a perfect crystal structure; a side view in Figure 2.5 would only show surface atoms. This process indicated that the performed plastic deformation was reversible [54].

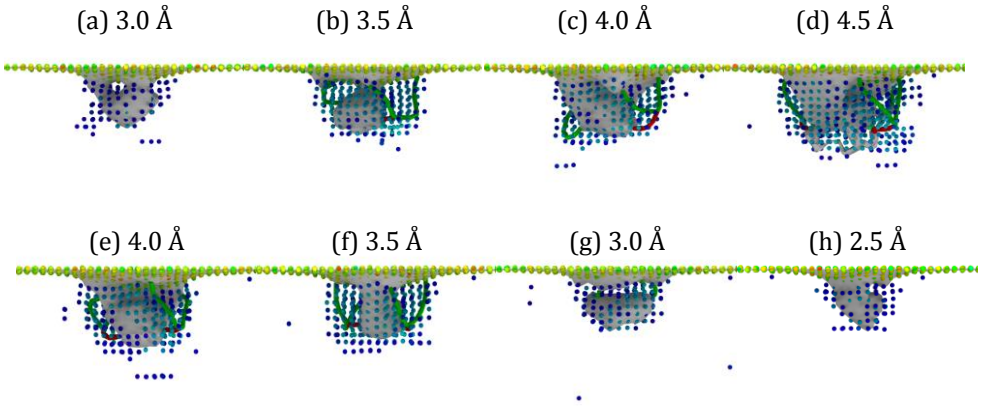

Figure 2.5 Dislocation evolutions during (a-d) the loading and (e-h) unloading processes. The green dislocations are Shockley partials, and the red ones are stair-rods. The surface of the deformed part including undefined defects is also shown. The atoms are colored based on their centrosymmetry parameter values.

In fcc crystal structure, the smallest Burgers vector has a length of $a_0/\sqrt{2}$. In Figure 2.6, the displacement vectors of the atoms, whose magnitudes were larger than the smallest Burgers vector, are depicted at four different indenter

depths of 4.5 Å and 5.0 Å, before and after the onset of plastic deformation, respectively, and at 9.5 Å and 10.0 Å, representing the final snapshots of the loading process. As can be seen, during the reversible regime of deformation, the atomic movements were restricted to those atoms that were adjacent to the indenter. By the initiation of plastic deformation, the slipping process was activated mainly in $(\bar{1}\bar{1}1)[0\bar{1}1]$ and $(1\bar{1}1)[0\bar{1}1]$ slip systems. Figure 2.6 shows that the process was continued until a depth of 9.5 Å; however, at the depth of 10.0 Å the movement of the atoms reached the edges of the simulation box and the simulation, at least for purposes of mechanical analysis, was no longer valid. The surface profile of the indentation at the depth of 9.5 Å, and its corresponding von-Mises stress field are shown in Figure 2.7. The edges of the pile-up profile align with [110], $[\bar{1}10]$, and [100].

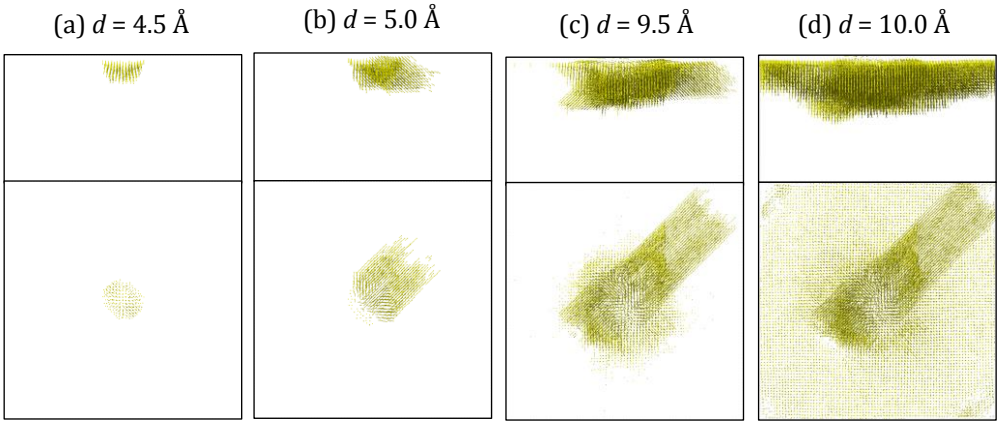

Figure 2.6 The displacement vectors (colored yellow) of the atoms which their movement were larger than the smallest Burgers vector, at different indentation depths. The figures are shows the system from (upper row) side view and (lower row) top view.

Because in fcc crystal structures the main slipping plane is {111}, the substrate was sliced along one of these planes, and the von-Mises stress field during the simulation was extracted as illustrated in Figure 2.8. As soon as the plastic deformation was initiated, the shape of the stress field was changed slightly, and a considerable amount of local stress was released at the depth of 5.5 Å due to dislocation slips, as shown in the figure. From the top view, a stress field becomes visible at the corners of the simulation box. This field is the result of slipping dislocations in the system.

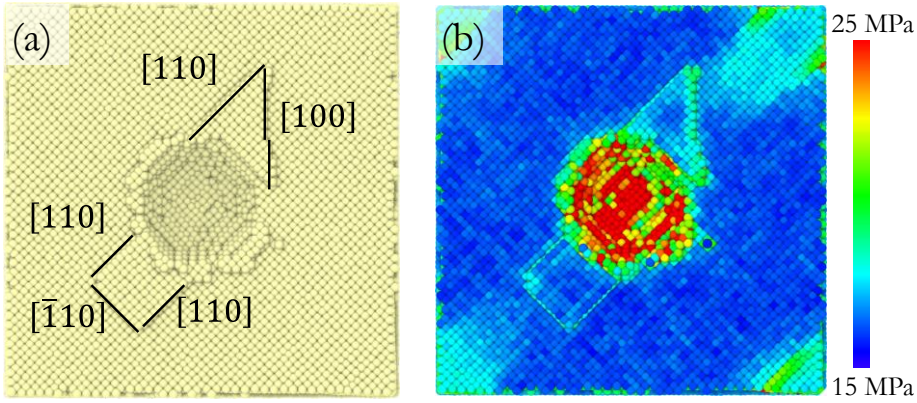

Figure 2.7 (a) Surface profile, and (b) surface stress distribution of the substrate at an indentation depth of 9.5 Å.

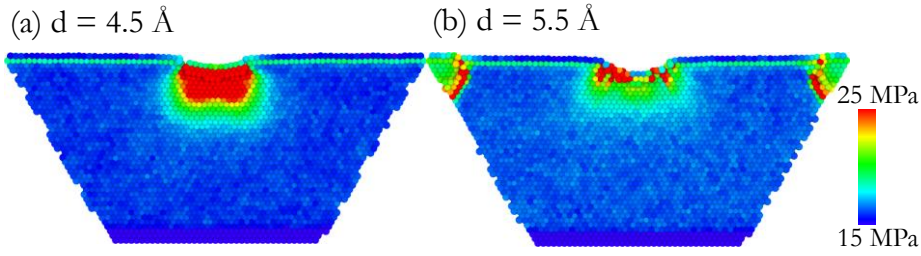

Figure 2.8 The von Mises stress field during the loading process along a ⟨111⟩ plane. The fields are depicted from an atomic slice of the substrate beneath the indenter.

The movement of the dislocations at the depths of 5.0 Å, and 5.5 Å is depicted in Figure 2.9. Moreover, it should be noted that the stress field of the system is higher along the slipping planes, as can be seen in Figure 2.10.

The reversible part of the $F-d$ curves is well described by the power law relation $F = Cd^m$, where C and m are fitting constants. The value of m was found to be 1.23, which is close to 1.5, the value reported for spherical indenters [55]. This force estimation of the elastic deformation part was also plotted in Figure 2.4, and shows a very good correlation to the simulation results.

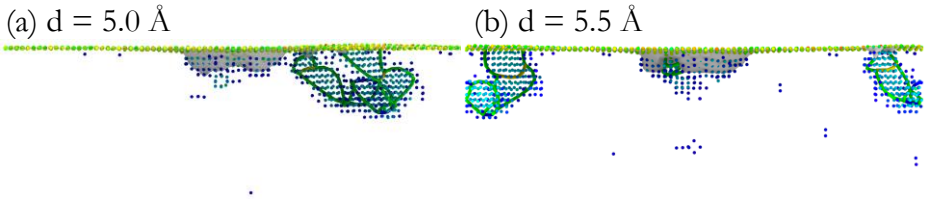

Figure 2.9 The dislocation lines after the initiation of the plastic deformation.

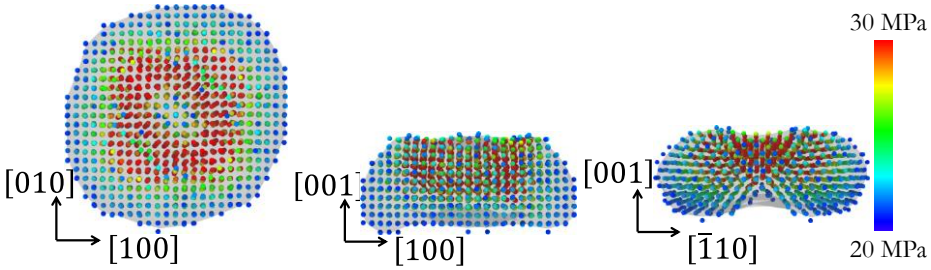

Figure 2.10 The stress field of the system with non-atomistic indenter at a depth of 4.5 Å. Only those atoms with a stress higher than 20 GPa are illustrated. The atoms are colored based on their stress values.

Because the particle had no adhesive force, the Hertzian formulation is expected to apply when modelling the elastic deformation region. In this model, the normal applied force can be calculated by:

$$F_{\perp} = 4/3\, E^{*} R^{0.5} d^{1.5}. \qquad (2.9)$$

Assuming the particle to be a rigid body, its Young's modulus would be infinity; in other words, the value of the reduced Young's modulus would be only a function of the mechanical properties of the substrate, i.e. $E = 218.1$ GPa and $\nu = 0.3$ (see Table 2.2). The elastic contact modulus, by means of (2.3), would be calculated to be $E^{*} = 239.7$ GPa. By fitting the Hertz solution to the MD results, the value of the reduced Young's modulus was found to be 244.8 GPa, which barely changes the Hertzian solution, as plotted in Figure 2.4. The slight discrepancy between the Hertzian solution and MD results could be partly due to the fact that, although the deformation was reversible, it was not purely elastic. It should be noted that higher values of the force constant of the particle would increase the reduced Young's modulus [56]. Also, increasing the indenter's radius results in higher values of E^{*} [57].

Moreover, the temperature of the substrate, and the moving velocity of the particle might have their own influence on the results; however, this is not the focus of the current investigation.

2.5.2 Contacts with adhesion

Figure 2.11 demonstrates the contacts at the beginning of the simulation, at their highest compression pressure, and after detachment, for both forced particles. The metal transfer in the system with the iron particle was small. On the other hand, the nickel particle had a very significant amount of metal transfer to the surface of the substrate. Such behavior was expected [21], and indicates high adhesion between the two surfaces. Although it is clear that the system with the nickel particle exhibited ductile rupture, unlike the detachment in the system with the iron particle, it was examined whether the contact behavior of the systems prior to sever plastic deformations can be described by continuum contact theories.

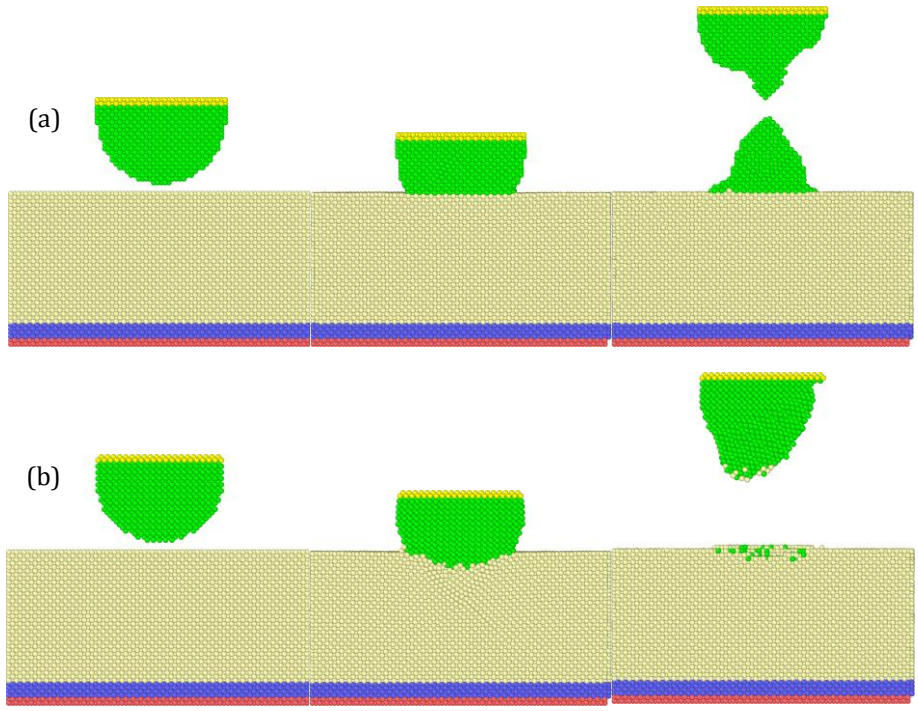

Figure 2.11 The sliced side view of the atomistic configurations of (a) nickel and (b) iron forced particles contacts with the substrate.

As the first step, the work of adhesion for each contacting systems was calculated. The potential energies of the systems when the blocks were side by side (phase A), and when they were far from each other (phase B) are reported in Table 2.3. In order to calculate the real contact area of the interface, the number of contacting atoms should be calculated first. Using the (001) plane density for fcc ($2/a_0^2$) and bcc ($1/a_0^2$) structures, it can be found that in an area of $10a_0 \times 10a_0$ with a (001) plane, there are 200 and 100 atoms in fcc and bcc crystal structures, respectively. It should be mentioned that the same results can be obtained also by using the corresponding contact distances for the calculation of the number of contacting atoms. The values of $A_{\text{real}} = N_{ca}A_a$ were obtained, and the surface energies were calculated by dividing these two values as reported in Table 2.3. The calculated surface energies are close to experimental values reported by other researchers [58].

Considering the two kinds of adhesive contacts in this study, the values of the work of adhesion would be as follows: for the pure nickel system, the work of adhesion could be defined as $\Gamma_{\text{Ni/Ni}} = 2|\gamma_{\text{Ni}}| = 4.32$ N/m; similarly, the nickel/bcc-iron contact would have $\Gamma_{\text{Fe/Ni}} = 2\sqrt{\gamma_{\text{Fe}}\gamma_{\text{Ni}}} = 4.54$ N/m.

Table 2.3 The potential energies of the systems with two identical blocks besides each other (phase A) and far from each other (phase B) are measured via MD simulations. The free surface energy values are reported in Jm^{-2}.

	Energy A	Energy B	A_{real} (Å^2)	$\gamma_{(100)} = \Delta\text{Energy / Area}$	γ_{exp} [58]
Ni/Ni	−35858.8	−35569.6	2144	−2.16	−2.45
Fe/Fe	−17245.6	−17071.9	1164	−2.39	−2.48

2.5.2.1 Contacts of free particles

The free particles were attracted toward the substrate because of the interatomic forces. Figure 2.12 shows the systems at the end of the simulations. The nickel particle was deformed at the contact, while the iron particle largely preserved its initial shape. Both systems were analyzed for crystallographic defects. It was found that no dislocation was generated in the substrate in the system with the nickel particle, while the particle itself experienced plastic deformation via generation and sliding of dislocations.

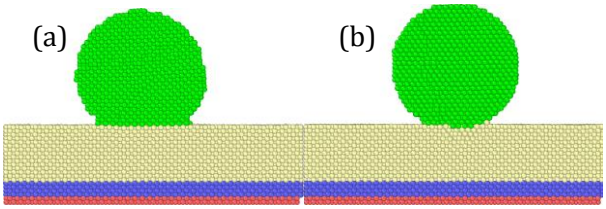

Figure 2.12 Atomistic configurations of (a) nickel and (b) iron free particles resting on the substrate.

These observations agree with experimental investigations that showed that plastic deformation may occur during adhesive interaction even with no external load [16]. In the system with the iron particle, it was only the substrate that experienced a limited number of dislocation generations: there were two Shockley partials, which stopped as soon as they interacted, and a stair-rod partial generated in the system.

The contact areas were calculated by measuring the number of contacting atoms as summarized in Table 2.4. Assuming the contact areas as perfect circles, the values of contact radii were obtained to be $r_{0,\mathrm{Ni/Ni}} = 2.09$ nm, and $r_{0,\mathrm{Fe/Ni}} = 1.73$ nm. These results are compared to the corresponding values of JKR and DMT models in Table 2.5. The comparison shows that both of the models underestimate the nickel/nickel contact area; however, the contact area of iron/nickel was correctly described by the JKR model.

Table 2.4 The number of contacting atoms and area of the free particles rested on the substrate.

	Particle atoms	Substrate atoms	Average contacting area (Å^2)
Ni/Ni	260	304	1371.5
Fe/Ni	199	187	937.5

Table 2.5 The contact modulus for the contacting systems, and the contact radius estimated from simulation and JKR and DMT models. The radii are reported in nm.

	E^* (GPa)	$r_{0,\text{simulation}}$	$r_{0,\text{JKR}}$	$r_{0,\text{DMT}}$
Ni/Ni	119.8	2.09	1.66	1.15
Fe/Ni	110.0	1.73	1.74	1.21

2.5.2.2 Contacts of forced particles: Iron

Figure 2.13 shows the force-displacement ($F-d$) curve of the iron/nickel system. The force drops at the very beginning corresponding to pull-in adhesion. This pull-in force was found to be $F_{\text{pi}} \cong -35$ nN. The drops in the adhesion force are stepped because of the terraced geometry of the particle. Then, the force increases smoothly up to its maximum value with no sign of plastic deformation. As the unloading starts, the force drops suddenly to its minimum value. Although the particles did not experience a sudden pull-off in this simulation, the minimum force was referred to as the pull-off force in this chapter. The pull-off force was found to be $F_{\text{po}} \cong -105$ nN. Then, the force increases up to the point where its slope starts to change. This change relates to plastic deformations in the system. As the unloading process continues, the particle separates and the force jumps to zero.

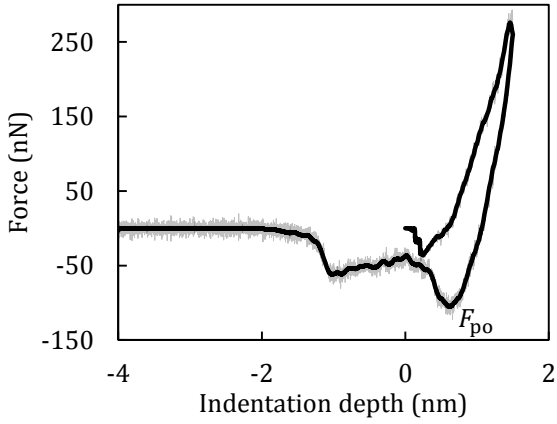

Figure 2.13 The normal force versus displacement curve of the iron forced particle system.

The analysis of the atomic configuration shows that there was no dislocation in the system during the unloading process until the force reached its minimum (point F_{po} in Figure 2.13). Following that point, however, the particle experienced plastic deformation. Figure 2.14 shows the deformed particle and the dislocation lines in it at the end of the simulation. The entire lower part of the particle was deformed, and experienced deformation twinning along the $(11\bar{2})$ plane to obtain the coherent twin. The angle between the twin-surface intersection and the fixed layer of the particle was found to be $\sim 32^{\circ}$. This value is very close to its ideal angle, i.e. $\theta \approx 35^{\circ}$ (e.g., see [59] for a review).

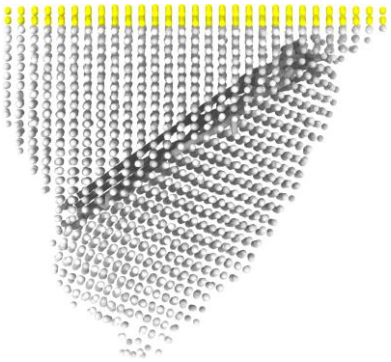

Figure 2.14 Atomistic configurations of the deformed bcc-iron forced particle at the end of the simulation.

Considering that JKR and DMT models do not describe the hysteresis of the $F - d$ curves, both pull-in and pull-off forces were used for calculation of χ. The values of χ, which are reported in Table 2.6, were found to be out of the JKR-DMT limits: $\chi_{(F=F_{\mathrm{pi}})} = 0.82$ was lower than $\chi_{\mathrm{JKR}} = 1.5$, and $\chi_{(F=F_{\mathrm{pi}})} = 2.45$ was higher than $\chi_{\mathrm{DMT}} = 2$.

Table 2.6 The pull-in and pull-off forces, and the corresponding values of $\chi = -F/\pi R\Gamma$ for the iron/nickel forced particle system.

F_{pi} (nN)	$\chi_{(F=F_{\mathrm{pi}})}$	F_{po} (nN)	$\chi_{(F=F_{\mathrm{po}})}$
-35	0.82	-105	2.45

The simulation shows that the contact area decreases until the particle is separated from the substrate; however, because of the transferred atoms between the particle and the substrate, the calculated contact area would be unacceptably overestimated if it were measured after the pull-off. Therefore, it was measured for the system during the loading and the unloading processes only up to the pull-off. The simulation results and the JKR and DMT solutions are shown in Figure 2.15. Two values of the contact area were obtained from the simulations: the real contact area A_{real} based on (2.1), and the projection of the contacting atoms A_{pc}.

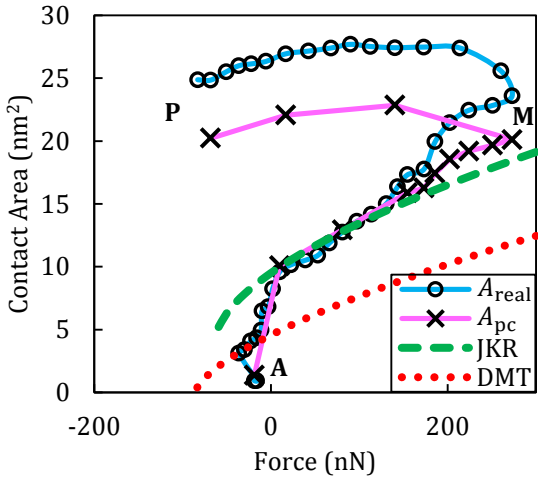

Figure 2.15 Changes of the contact area as a function of the applied normal force in the system with the iron forced particle. The loading step begins from point **A**, and continues to its maximum load at point **M**. By the unloading step, the force reduces to its pull-off value at point **P**.

The inception of contact occurs at point A. Then, the contact area increases while the force drops because of the pull-in adhesion force. It can be seen that when the force reaches zero again, the contact area is very close to the JKR prediction, which was expected from the results of the free particle simulations. Moreover, as the loading increases the system's behavior was very close to the JKR model, till the substrate start to generate dislocations. As a consequence, the simulated system's behavior deviated from the JKR model. Then, the unloading step begins, but the contact area increases slightly; this might be a result of the kinetic energy of the particle's atoms: i.e., after changing the direction of the force, atoms were still moving in their previous

direction for a brief time. As the unloading continues, the force drops but the contact area remains almost unchanged until pull-off occurs. The comparison between A_{real} and A_{pc} shows that the A_{pc} is not that sensitive to the generation of dislocations. Moreover, the analyses of the contact showed that the contacting atoms had a bowl shape, noticeable during the unloading process; while the 3D shape of the contact cannot be reflected in the 2D projection of the contacting atoms, the actual shape of the contact affects the real contact area. Therefore, as soon as the dislocations were generated, the values of A_{pc} were smaller than of A_{real}. Moreover, it was found that, during the loading process, the results of the projection of the contacting atoms were closer to the JKR model than to A_{real}.

2.5.2.3 Contacts of forced particles: Nickel

The $F - d$ curve of the system is shown in Figure 2.16. At the beginning of the loading process the force drops to $F_{\mathrm{pi}} \cong -22$ nN because of the adhesion force between the asperity and the subject. The adhesion-caused drops are shown to occur more than once; that is because of both the stepped geometry of the particle and the high value of the adhesion force. As the loading process was continued, there were abrupt force drops as indications of plastic deformations. By starting the unloading process, the force drops suddenly to a minimum of -190 nN. Then, the curve continues with a saw-like shape, indicating a number of plastic deformations, until the final rupture.

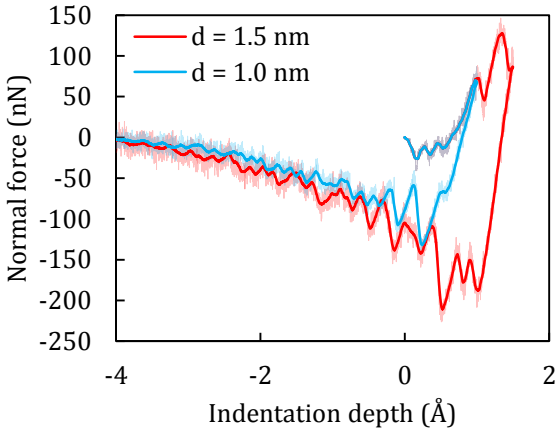

Figure 2.16 The vertical force vs displacement curve of the bcc-iron forced particle systems with the displacements of 1.0 and 1.5 nm.

An additional MD simulation was run to avoid inducing plastic deformation during the loading process by reducing the displacement of the particle to 1.0 nm. The $F - d$ curve of this additional simulation is also shown in Figure 2.16. During the unloading process, the force reached its first local minimum, referred as the pull-off force in this chapter, with a value of $F_{\mathrm{po}} \cong -67$ nN. The atomic configuration analysis of the system showed no dislocation line in the system at pull-off. As the unloading process was continued, instead of an abrupt detachment, the particle experienced a series of plastic deformations along {111} planes, which resulted in the saw-like shape of the curve.

The values of χ using, both, the pull-in and pull-off forces were calculated to be 0.54 and 1.65, respectively. The results (summarized in Table 2.7) indicates the applicability of the JKR model for describing the contact.

Table 2.7 The pull-in and pull-off forces, and the corresponding values of $\chi = -F/\pi R\Gamma$ for the nickel/nickel forced particle system.

F_{pi} (nN)	$\chi_{(F=F_{\mathrm{pi}})}$	F_{po} (nN)	$\chi_{(F=F_{\mathrm{po}})}$
-22	0.54	-67	1.65

The evolution of the contact area between the particle and the substrate was measured and is depicted in Figure 2.17. As the loading begins, the adhesion force becomes increasingly dominant at the interface. The contact area increases until the force reaches its maximum. For the force ranging between zero and its maximum (point M), the JKR model compares favorably as opposed to the DMT. As the unloading process starts, the contact area remains unchanged.

2.6 Conclusions

The results presented in this chapter address some discrepancies between the continuum models and atomistic simulations for the contact of simple geometries. For contacts with no adhesion, it was shown that Hertzian theory can describe the force-displacement behavior of the system for the reversible regime of deformation. Also, it was shown that the stress field of the substrate beneath the indenter in the slipping plane was similar to that predicted by continuum models; however, it should be noted that the stress field is

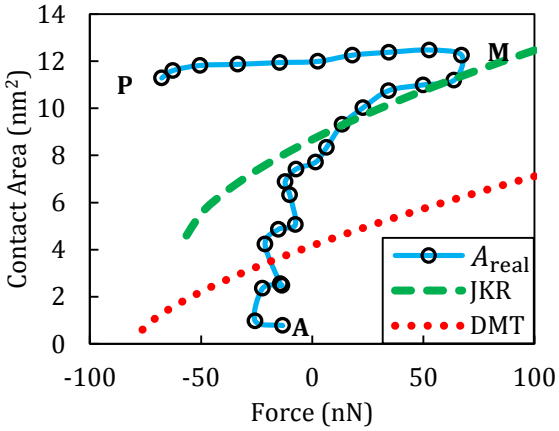

Figure 2.17 Changes of the contact area vs. the applied vertical force in the system with the nickel forced particle. Point **A** indicates the beginning of the simulation which goes up to point **M**, corresponding to the maximum load. The force drops to its pull-off value (point **P**) as the unloading starts.

directional in crystalline atomic systems, and therefore, not the same as what is assumed in continuum models.

Although the results were in general agreement with Hertzian theory, continuum adhesive models (JKR and DMT in this study) were unable to correctly describe atomic scale contacts when adhesion was introduced to the system. One of the difficulties in the comparison between MD simulations and continuum models was the elastic/plastic deformation of the particles after the systems reached pull-off; in comparison, continuum mechanics models predict that the particles suddenly detach from the substrate at pull-off. It was also shown that both systems experienced some plastic deformation after pull-off. The iron particle detached from the substrate and exhibited twinning behavior. On the other hand, the nickel particle formed extensive necking at the interface with the substrate, and experienced ductile rupture instead of detachment.

Analyzing the free particles, it was found that the JKR model could correctly predict the contact area of the iron particle; however, both, JKR and DMT models underestimated the contact area of the nickel free particle. Considering the plastic deformations of the nickel free particle during the process, this discrepancy could be justified.

Comparing the contact area of the forced particles as a function of force, it

was found that during the initial stage, i.e. pull-in and for $F_{\perp} \leq 0$ nN, the contact area increases suddenly, but in an stepped manner. This stepped behavior, which could also be recognized in the $F - d$ curves, was a direct consequence of the terraced geometry of the forced particles. While this geometry affected the contact's behavior to deviate from continuum models, the loading contact could be correctly described using the JKR theory, as long as no dislocation line was generated in the system; the substrate experienced dislocation generation in the contact with the iron particle, which increased the contact area, and resulted in a deviation from the JKR model.

Although the JKR and DMT models are reversible, MD simulation results show an adhesion hysteresis for both atomistic asperities. This behavior is related to energy dissipation because of inelastic deformation in the contact, which affects the work of adhesion [60]. Considering the energy loss, the effective work of adhesion is reduced during the loading step; reducing the load necessary to separate the surfaces, in turn causes the effective work of adhesion to be increased. Therefore, the contact area remains unchanged until the force can overcome the increased effective work of adhesion.

Deviations from continuum models, as demonstrated in this chapter and as suggested in the literature [3, 23], are to be expected when studying atomistic systems since many fundamental assumptions of those models are neglected: for example, materials are not necessarily homogenous, and the contact surfaces are not frictionless. However, the results show that atomistic contacts, during the loading process, can be correctly described by the continuum models as long as the system has not experienced dislocation generation. The reason is that the generated dislocations introduce extra atomic steps at the contact's interface, which results in an unpredictable increment in the contact area. It should be noted that the generation of dislocations at their early stage leads to reversible plastic deformation; therefore, the reversibility of the deformation is not enough for claiming the applicability of the continuum models.

Chapter 3 *

Definition and detection of contact in atomistic simulations

In atomistic simulations, contact depends on the accurate detection of contacting atoms as well as their contact area. While it is common to define contact between atoms based on the so-called 'contact distance' where the interatomic potential energy reaches its minimum, this discounts, for example, temperature effects on atomic vibrations and, correspondingly, the spatial distributions of atoms. In this chapter, classical molecular dynamics was used for investigating the definition and detection of contact between a spherical particle (made of either silver, lead, or platinum) and a flat substrate (silver). Total contact areas were estimated via three previously published methods for the detection of atoms in contact: the first method detected contacting atoms based on their potential energy values; the second method utilized interatomic distances; and, the last method was based on the interacting potential energy values between the contacting atoms of the counterpart interfaces. Each method was examined in detail with our findings suggesting that the use of interatomic distances is the most suitable way to define and detect the real area of contact in atomistic simulations of normal contact. Our results suggest that the minimum of the radial distribution function after the first peak can be defined as the contact distance. Also, a temperature-dependent empirical equation was proposed to estimate the contact distance for Lennard-Jones potential. Moreover, the atomic diameter was defined as the distance between the origin (i.e. the center of the reference atom) and the first peak in the radial distribution function, allowing for an estimation of the atomic contact area.

3.1 Introduction

The knowledge of the real contact area (A_{real}) between contacting surfaces plays an important role in tribological studies. It is well known that

* This chapter has been originally published in Computational Materials Science **109** (2015) 172–182.

macroscopic contacts are rough and consist of a large number of smaller contacts between peaks (asperities) [61], so that their total area ($\sum A_{\mathrm{asp}}$) is much smaller than the apparent macroscopic contact area. Experimentally, the real contact area can be found via $\sum A_{\mathrm{asp}} = F_{\parallel}/\bar{\tau}$, where $F_{\parallel}$ and $\bar{\tau}$ are the friction force and effective shear strength of the contacting bodies, respectively. In the absence of surface forces, the real contact area rises linearly with the load irrespective of whether the surfaces deform elastically or plastically [25, 62]. With the miniaturization of devices, however, surface forces become dominant and can highly influence device performance. Therefore, the understanding of nanocontacts is crucial in the design of nano-devices with the accurate characterization of the real contact area becoming a critical issue.

Carpick et al. investigated the frictional behavior of a Pt-coated atomic force microscope tip in contact with a mica surface cleaved in ultrahigh vacuum [2]. These early experiments found that the Johnson-Kendall-Roberts (JKR) theory [14] and an extended version of it [2] could be used to describe nanocontacts, assuming a constant shear stress at the interface. Nonetheless, continuum mechanics models are not the most suitable method for the study of tribological behavior at the atomic scale, essentially because of the discreet nature of atoms. This problem guided researchers towards atomistic computer simulation methods, and especially molecular dynamics (MD) [13], to study contacts at the atomic scale. At the time, it was assumed that the MD simulation results should match with continuum models; however, this notion was challenged by Yang and Persson, for example, who reported that the contact area estimated via detection of the contacting atoms does not show satisfactory results compared to the Hertz theory [12]. Furthermore, when Luan and Robbins published their MD simulation results of single asperity contacts for different tip geometries [3, 23], they showed that atomistic surface roughness, which always exists in any discrete atomistic surface, has profound effects on the results: roughness yields deviations from the predictions of continuum theories for the local stresses, contact areas, the work of adhesion, friction and lateral stiffness. While Luan and Robbins concluded the breakdown of continuum models for atomistic mechanical contacts, Mo et al. found that the accurate calculation of contact area at a given length scale should yield reliable results [4]. Later, Cheng and Robbins explored the effects of the atomic thermal fluctuations on the estimated contact area [6], and suggested an averaging of the contacting atoms over time to overcome the atomic thermal fluctuations.

This chapter addresses the definition of contact at the atomic scale for

adhesive contacts. The non-adhesive case of contact is treated in Chapter 4.

3.2 A short review of contact at the atomic scale

Regarding the definition of contact in an atomistic system, two concerns should be addressed: the detection of contacting atoms (a_c), and their conversion into contact area. One way to define the contacting atoms is based on their forces, i.e. an atom is in contact if it has a nonzero force in the loading direction from the counterpart. For instance, Knippenberg et al. [63] simulated sliding contact between a spherical fullerene tip (composed of 720 carbon atoms) and a nominally flat, amorphous carbon surface covered with a self-assembled monolayer. Applying the abovementioned method, they found that on average there are 32 atoms of the tip responsible for ~96% of the load; they found that the contact radii calculated using the 32 atoms that support the majority of the load are close to the results of the thin-coating contact mechanics developed by Reedy [64]. Although this definition seems to be straightforward, its usage is ambiguous in adhesive contacts. Moreover, an averaging of force over time is needed to yield reliable results [6].

The most common way to consider two atoms in contact, which is also utilized in the current study, is to see if their centers are closer to each other than a contact distance (d_c). A common definition for d_c is the atomic distance at the onset of direct repulsion between atoms, i.e. where the potential energy reaches its minimum value (r_E) [6, 7]. Another method is based on the crystal structure of the materials. Spijker et al. [8] defined the contact distance based on the neighboring distances of atoms, and used the second neighbor distance for d_c. Solhjoo and Vakis ([65], see Chapter 2) defined the contact distance as being slightly larger than the first neighbor distance based on crystallographic packing factors. See the previous chapter for the details. Eder et al. [9] suggested that, in the case of an amorphous structure, a statistical value could be used for the definition of the contact distance, namely the radial distribution function.

The radial distribution function (RDF) in a particulate system describes the density distribution of particles around a reference particle as a function of distance. In a homogeneous and isotropic system, an average of all RDF values could be used to describe the density distribution of the whole system. Figure 3.1 (a) illustrates a 2D atomistic system: a ring of radius r and thickness dr could be used to calculate the RDF. Varying the radius encloses a different number of atoms in the annulus between r and $r + dr$, yielding a new point on the RDF curve. Dividing the calculated radial density $\rho(r)$ by the average

density (ρ_0 = No. of atoms / Volume of the system) results in a $g(r)$ plot, which could be used to characterize the crystallographic properties of the system. This plot could be obtained, both, from experiments (e.g. by means of X-ray diffraction) and simulations (e.g. using molecular dynamics).

Typical $g(r)$ plots (Figure 3.1 (b)) correspond to two categories of atomistic systems: crystalline and amorphous. These curves have a number of important features. Firstly, at short separations, the value of $g(r)$ is zero, indicating that atoms cannot be closer than some specific value corresponding to the appearance of the first peak: the beginning of the first peak is indicated in Figure 3.1 (b) by d_{s}. Moreover, there are a number of peaks related to the neighbor distances, which could be used to distinguish between different crystal structures. The width of the peaks, for a crystalline system, are broad if the atoms are allowed to vibrate to a high extent, e.g. at higher temperatures. By confining the vibration of the atoms, e.g. by lowering the temperature, the peaks tend to be sharp. In an extreme situation, if the atoms cannot vibrate at all, i.e. at a temperature of absolute zero, $g(r)$ peaks would appear as lines. Furthermore, in a system with amorphous structure, the peaks are by definition not related to any specific crystal structure, demonstrating the randomness of the atoms' positions in the system. For an amorphous system, Eder et al. [9] suggested that a value slightly smaller than the first minimum in the $g(r)$ plots can be assigned as the contact distance.

In yet another approach to detect atoms at contact based on the potential energy of each atom, Solhjoo and Vakis [66] showed that surface atoms have higher potential energies than atoms in the bulk. Therefore, by defining a cutoff for the potential energy (PE_{c}), it is possible to distinguish between the atoms on the surface and those in the bulk. Upon the initiation of contact between the counterpart surfaces, surface atoms are distinguished into contacting (a_{c}) and non-contacting (a_{nc}) based on their potential energies.

The next step, once contacting atoms have been identified, is the estimation of the contact area. One method would be the direct conversion of data from the contacting or non-contacting atoms into an area. To do so, one may define the contact area as the area enclosed by the edges of the contact zone. Mo et al. [4] showed that this approach does not hold at the atomic length scale; instead, the real contact area should be $A_{\mathrm{real}} = N_{\mathrm{c}a} A_a$, where $N_{\mathrm{c}a}$ is the number of the contacting atoms of the sample, and A_a is the average surface area per atom [4]. Mo et al. [5] calculated A_a by dividing the nominal surface area of a sample (A_{nom}) by the number of atoms at that surface. Solhjoo and Vakis ([65], see Chapter 2) defined A_a based on the atomic radius in a perfect crystal structure, and assuming that atoms are equal-sized hard spheres.

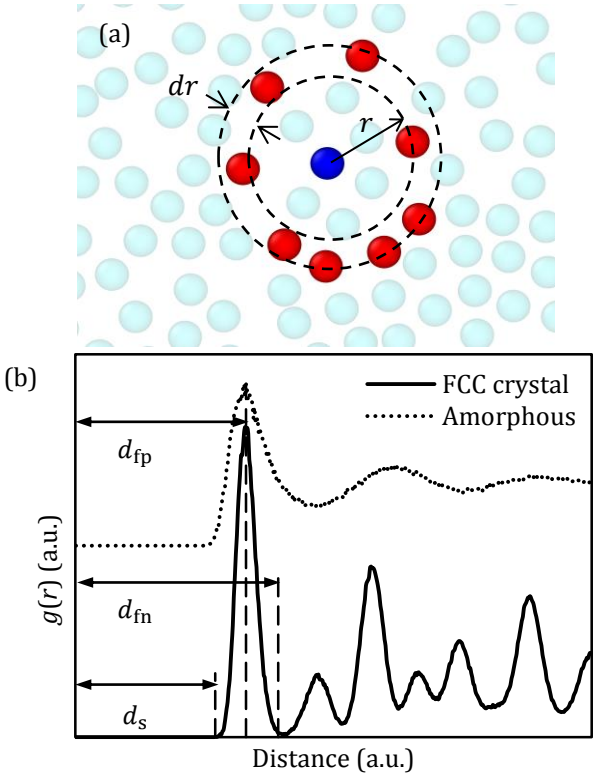

Figure 3.1 (a) A 2D particulate system, where a ring of radius r and thickness dr around a reference particle (dark blue atom) contains number of atoms (red atoms), and (b) the typical $g(r)$ plots for a crystalline and amorphous structures. The beginning of the first peak, the distance where the first peak occurs, and the first minimum are denoted as d_s, d_{fp}, and d_{fn} in the figure, respectively.

In another approach, Spijker et al. [8] projected the contacting atoms on a surface grid normal to the applied force, with each grid cell on the projection surface measuring 2.5 times the atomic distance at the minimum of the potential energy. A summation of the area of the occupied grid cells is defined as the projected contact area. Finally, Solhjoo and Vakis [66] projected the non-contacting atoms on a surface normal to the applied force, and calculated their area (A_{nca}); then, they defined the real contact area via $A_{real} = A_{nom} - A_{nca}$.

Although all abovementioned methods estimate the contact area by some method of identification of contacting atoms, there is yet another

methodology. Wenner [67] estimated A_{real} without considering individual atoms in the system, but by calculating the pair potential energy between the atoms of the two counterparts ($E_{\mathrm{a,b}}$) and dividing this value by the interfacial energy per area between the counterparts, Δ. In short, the previously published methods regarding the contact area under a normal force could be divided into three categories, summarized in Table 3.1.

Table 3.1 Three different methods for the estimation of the real contact area, and their placement in the discussion section.

Method		Detection of the contacting/non-contacting atoms	Estimation of A_{real}	Section
A	Projection of the non-contacting atoms	Based on the potential energies	$A_{\mathrm{real}} = A_{\mathrm{nom}} - A_{\mathrm{nc}a}$	3.6.1
B	Counting the contacting atoms	Based on the pair atomic distances	$A_{\mathrm{real}} = N_{ca} A_a$	3.6.2
C	Measuring the contact energy		$A_{\mathrm{real}} = E_{\mathrm{a,b}}/\Delta$	3.6.3

Moreover, during tribological processes, it is very probable to have some atoms leave their original part and transfer to the counterpart. Detection of these transferred atoms is crucial, because failure to do so results in a higher number of contacting atoms; therefore, the estimated contact area could be unreasonably higher than the actual one. In order to solve this problem, Eder et al. [9] suggested that these atoms could be identified from their mean velocities in the sliding direction over a span of time. In another method, Spijker et al. [8] stored the atoms of the contacting parts into clusters by a depth-first search algorithm: whenever a cluster was found to be disconnected from other clusters in the original part, the atoms of that cluster were considered as the transferred ones. Nonetheless, the transferred atoms issue during sliding is not the goal of the current chapter; however, the early results of the further investigations on this issue can be found in Appendix A.

3.3 Simulation methodology

In order to compare the three described methods (Table 3.1), one nanocontact should be studied separately via each method. Also, since the elements in the contact could affect the results of each method, several nanocontacts were simulated to study, both, the effect of materials in the system, as well as the differences between methods. The simulations were performed by placing different spherical particles on a substrate under zero external force. An atomically flat substrate comprising a single fcc crystal was generated from silver atoms, with dimensions of $40a_0 \times 40a_0 \times 10a_0$, where $a_0 \cong 4.09$ Å is the lattice constant of the simulated silver [45]. At the bottom, atomic layers were fixed to resemble a rigid substrate. The next four atomic layers were assigned to be the thermostatic layer, and the remaining atoms (14 atomic layers) were not constrained. The contacting spherical particles were generated from silver, lead, and platinum. Each particle had a spherical shape with a radius of 30 Å and a stepped geometry [65], and was placed~3 Å above the substrate. Periodic boundary conditions (PBCs) were applied in the lateral directions. The simulations were run for 1 ns.

The large-scale atomic/molecular massively parallel simulator (LAMMPS) [37] was used to perform the simulations. The velocity-Verlet algorithm [38] was used to solve the equations of motion with a step size of 10 fs [65]. The Berendsen's thermostat [39] was applied to the thermostatic layers to keep their temperature at 300 K. The crystalline directions of $[\bar{1}10]$, $[\bar{1}\bar{1}2]$, and $[111]$ were defined as the *x*, *y*, and *z* coordinate directions, respectively. The post processing analyses were done using OVITO [40] and ImageJ [68].

The simulations were categorized into two sets based on the governing potential energies: one was performed by applying the Lennard-Jones (LJ) potential [35], and the other was governed via the embedded atom method (EAM) potential [69]; this was done so as to make a comparison between the effects of using LJ or EAM potentials in the definition of contact. Although it is common to use EAM for simulations of metallic systems, the LJ potential still plays an important role in atomistic simulations of contacts, mostly in order to control the adhesion, or to define the interactions between metallic and non-metallic substances in the system, e.g. in [8, 70]. Therefore, both of these potentials were examined in this study. The potential energy value between two atoms i and j via the LJ formulation can be estimated by

$$E_{ij} = 4\varepsilon\left(\left(\sigma/r_{ij}\right)^{12} - \left(\sigma/r_{ij}\right)^{6}\right), \tag{3.1}$$

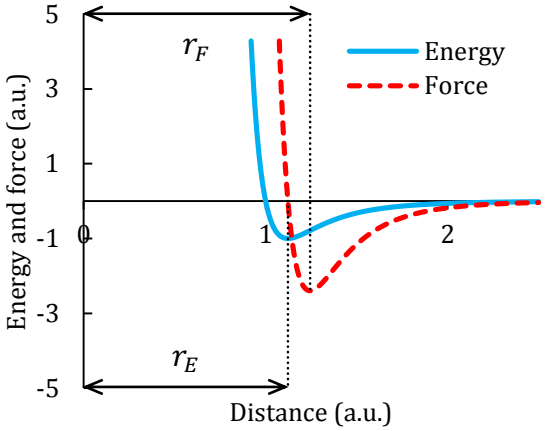

Figure 3.2 Schematic plot of the Lennard-Jones potential and force, with $\varepsilon = 1$, and $\sigma = 1$.

where ε is the depth of the potential well, and σ is the distance where the potential energy is zero. The schematic plot of (3.1) is depicted in Figure 3.2.

The LJ parameters reported by Shu and Davies [71] (see Table 3.2) were used for pure elements, while the LJ parameters between different elements were estimated using the mixing rules proposed by Waldman and Hagler [72], which are described as follows:

$$\sigma_{ij} = \left(\left(\sigma_i^6 + \sigma_j^6\right)/2\right)^{1/6}, \tag{3.2}$$

and

$$\varepsilon_{ij} = 2\sqrt{\varepsilon_i \varepsilon_j}\left(\sigma_i \sigma_j\right)^3 / \left(\sigma_i^6 + \sigma_j^6\right), \tag{3.3}$$

where i and j represent two dissimilar non-bonded atoms. These mixing rules have been shown to yield accurate results compared to experiments (e.g. see [73, 74]).

In the EAM potential, the total energy E of the system can be expressed as [69]

$$E = \frac{1}{2}\sum_{i,j,i\neq j} \varphi_{ij}(r_{ij}) + \sum_i F_i(\rho_i), \tag{3.4}$$

where φ_{ij} is the pair potential energy between atoms i and j separated by a distance r_{ij}, and F_i is the embedding energy associated with embedding an atom i into a local site with an electron density of ρ_i. The value of ρ_i can be

calculated from $\rho_i = \sum_{j,i\neq j} f_i(r_{ij})$, with $f_i(r_{ij})$ being the electron density at the site of atoms i arising from atom j at a distance r_{ij}.In this chapter, the EAM potential database developed by Zhou et al. [45] was used; the database includes the needed parameters and formulae to define the EAM model. Furthermore, the pair potential between dissimilar species A and B, $\varphi^{AB}(r)$, was constructed by the mixing formula developed by Johnson [75] in the form of

$$\varphi^{AB}(r) = \frac{1}{2}\Big(\big(f^{B}(r)/f^{A}(r)\big)\varphi^{AA}(r) + \big(f^{A}(r)/f^{B}(r)\big)\varphi^{BB}(r)\Big). \qquad (3.5)$$

Moreover, a few additional calibration simulations were performed as necessary. Those simulations and their results are described in detail in the following sections, with emphasis on the parts of their procedures that are different from the abovementioned method.

Table 3.2 The Lennard-Jones parameters for silver, lead, and platinum used in this chapter.

	Ag	Pb	Pt
ε (eV)	0.3453	0.2363	0.6815
σ (Å)	2.6376	3.1888	2.5394

3.4 The contact distance

As was mentioned previously, the interatomic distance where the potential energy is minimum, r_E, is a commonly used value for the contact distance; however, this definition suffers from two problems: there is not a specific r_E value for non-pairwise potential energies, and also, the system state, i.e. temperature and pressure, is not reflected in this value. Therefore, this definition is limited to systems with pairwise potential energies, at a state where the atoms are not vibrating, i.e. at 0 K. A more general definition is based on the first atomic neighbor distance (d_{fn}). This value can be calculated for perfect crystal structures via well-established formulae based on the constant parameters which can be calculated for a specific state; however, if the system is not perfectly crystalline, this methodology does not hold

anymore. The most generally applicable method, then, is to consult the corresponding $g(r)$ plots. These plots can be calculated numerically, regardless of the potential energy type and the crystal structure.

In the current study, the surfaces were under no externally applied pressure; therefore, $g(r)$ plots resulting from the isothermal-isobaric (NPT) ensemble at an external pressure of 0 GPa and a corresponding temperature of 300 K were generated to quantify the similarities between the different simulations. Along these lines, a series of simulations were performed for cubic systems of crystalline silver, lead, and platinum. The temperature and pressure were controlled via the algorithm developed by Shinoda et al. [76]. The $g(r)$ curves were obtained by using the positions of all atoms across systems. The $g(r)$ curves are shown in Figure 3.3 and reveal that EAM potentials suggest a larger value for d_{fn} compared to LJ potentials; the values of d_{fn} can be found in Table 3.3. As mentioned in the simulation methodology section, the Waldman and Hagler [72] mixing rules were applied between different elements. Applying the same formulation, the values of d_{fn} between elements i and j can be estimated via $d_{\mathrm{fn,ij}} = \left(\left(d_{\mathrm{fn,i}}^6 + d_{\mathrm{fn,j}}^6\right)/2\right)^{1/6}$. The provided values of contact distances in Table 3.3 were used in the analyses in the current study.

Table 3.3 The values of d_{fn} in Å for silver, lead, and platinum.

	Ag	Pb	Pt	Ag/Pb	Ag/Pt
EAM	3.248	4.148	3.053	3.825	3.158
LJ	3.068	3.773	2.903	3.507	2.991

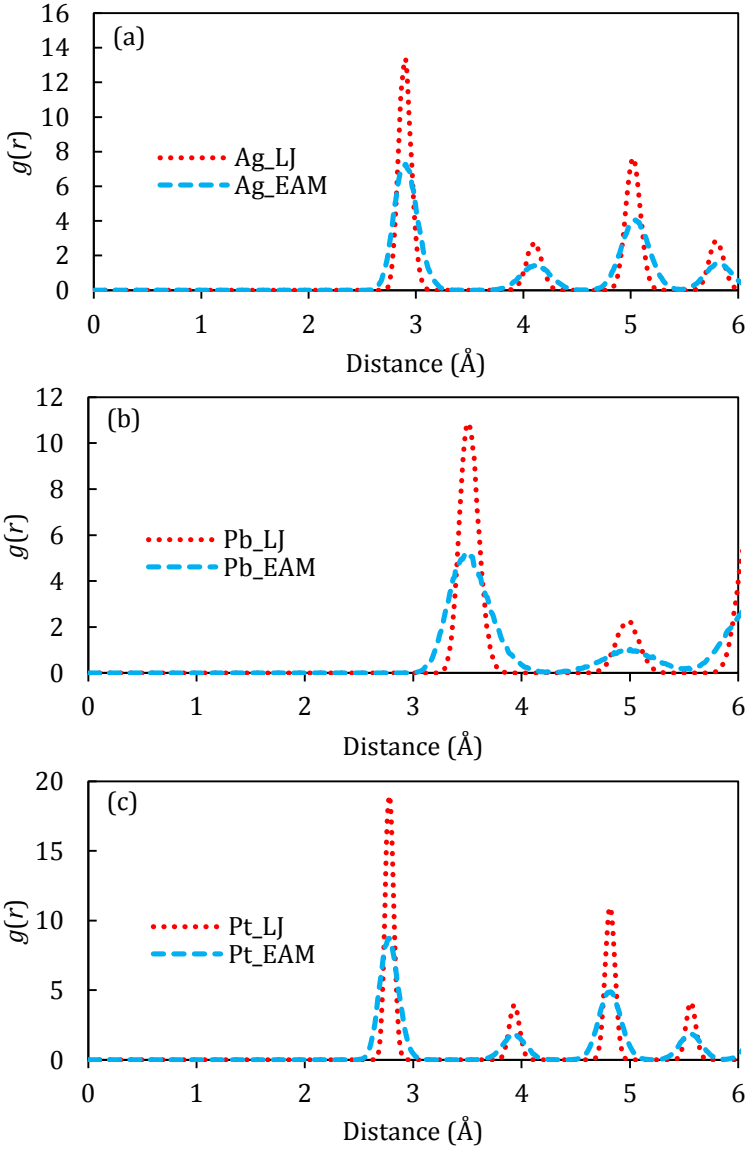

Figure 3.3 The $g(r)$ plots of systems composed of silver, lead, and platinum, at 300 K, and under an external pressure of 0 GPa; both the LJ and EAM potentials were used for the simulations.

3.4.1 Estimation of the contact distance based on the Lennard-Jones potential

In order to estimate the contact distance from the LJ potential, one may argue that the distance of an atomic pair should not exceed the distance at the LJ maximum force, in order for it to be considered as being an atomic pair. The LJ force can be calculated as follows:

$$F = -dE/dr = -24\,\varepsilon/\sigma\,(2(\sigma/r)^{13} - (\sigma/r)^{7}). \tag{3.6}$$

Figure 3.2 illustrates a schematic plot of an LJ-type potential and force. The distances at the minimum of the potential (r_{E}) and of the force (r_{F}) are functions of σ, i.e. $r_{\mathrm{E}} = 2^{1/6}\sigma$ and $r_{\mathrm{F}} = (26/7)^{1/6}\sigma$. The reason for the difference between r_{E} and r_{F} is that the LJ potential is anharmonic. As the temperature increases, the atomic thermal vibration would be higher, indicating that the temperature should play a role in the calculation of d_{fn}.

Although the LJ parameters can be adjusted for a certain range of temperature and pressure conditions, let us assume a set of LJ parameters, i.e. values of ε and σ, that can work without any limitation. In such a case, the maximum atomic distance between an atomic pair would change from r_{E} at 0 K where there is no atomic thermal vibration, to r_{F} at a temperature where the thermal vibration results in the bond breaking. Therefore, at temperatures higher than absolute zero, d_{fn} should tend towards r_{F}. If the potential energy value between two atoms is known, then the following formulae can be used to calculate the distances between the two:

$$r_{-} = \left(-2\sigma^{6}/\left(\sqrt{(E+\varepsilon)/\varepsilon} - 1\right)\right)^{1/6}, \tag{3.7}$$

and

$$r_{+} = \left(2\sigma^{6}/\left(\sqrt{(E+\varepsilon)/\varepsilon} + 1\right)\right)^{1/6}, \tag{3.8}$$

where r_{-} and r_{+} represent the distances lower and higher than r_{E}, respectively.

Figure 3.4 demonstrates (3.7) and (3.8), and their average. As can be seen, the average tends to higher values than r_{E}; whether this average can be used as the contact distance or not, this behavior indicates that, at energy states higher than ε, a value larger than r_{E} should be defined as the contact distance. Considering the melting point (T_{m}), the following weighted mean of r_{E} and r_{F} showed a good fit with the measured d_{fn} from $g(r)$ plots:

$$\overline{r} = (r_{\mathrm{E}} + \theta r_{\mathrm{F}})/(1+\theta), \tag{3.9}$$

with $\theta = T/T_{\mathrm{m}}$, where T is the current temperature in Kelvin. The values of the melting point, r_{E}, r_{F}, and $\overline{r}$ for the simulated materials can be found in Table 3.4.

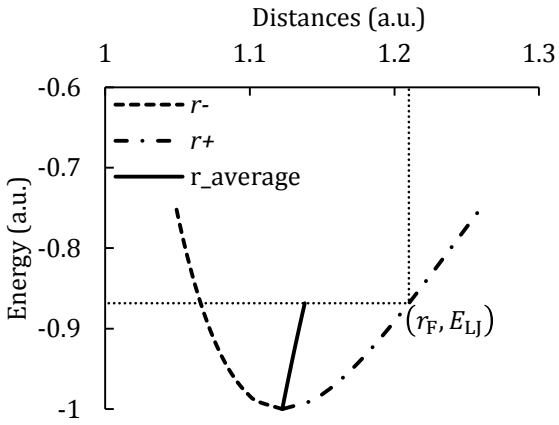

Figure 3.4 The Lennard-Jones potential around its minimum. The r_{-} and r_{+} the curves are determined from (3.7) and (3.8), respectively, for $\varepsilon = 1$ and $\sigma = 1$. Because the Lennard-Jones potential is anharmonic, the average distance between two vibrating particles is larger than r_{E}. Moreover, because the bond between two atoms at distances farther than r_{F} could be considered as broken, the average distance between r_{-} and r_{+} is shown up to the energy where the distance between the two atoms reaches r_{F}.

Table 3.4 The values of T_{m}, r_{E}, r_{F}, $\overline{r}$, and d_{fn}(copied from Table 3.3) for silver, lead, and platinum. Distances are reported in Å, and temperature is in Kelvin.

	T_{m}	r_{E}	r_{F}	$\overline{r}$	d_{fn}
Ag	1234.95	2.961	3.282	3.066	3.068
Pb	600.65	3.579	3.968	3.774	3.773
Pt	2041.15	2.850	3.160	2.921	2.903

3.5 The area of an individual atom

In order to convert the MD contact data to the real contact area, it is important to define a conversion factor. Mo et al. [5] estimated A_a by dividing the total nominal surface area by the total number of surface atoms. Therefore, the method defines a crystallographic-directional shape for atoms. In principle, this definition is not compatible with the MD simulation technique which treats atoms equally regardless of the crystallographic directions. Considering atoms as spheres is common in atomistic studies. This removes directionality from individual atoms, although there could be gaps or overlaps between them. It should be noted that these features, i.e. the gaps (due to the crystallographic directions) and overlaps (mainly due to the simulation conditions, i.e. temperature and pressure), could cause a discrepancy between the nominal and actual area of an atomic plane. A spherical representation of atoms with a radius of r_a results in an area of $\pi {r_a}^2$ for A_a. But, what is an acceptable definition for A_a or r_a?

One way to solve the problem is to define A_a based on the most packed atomic plane for crystalline materials. For instance, from {111} in the face-centered cubic (fcc) crystal structure it can be found that $A_a = \mathrm{a}_0^2\sqrt{3}/4$. Using this method, the value of A_a can be estimated with the assumption that there are no atomic gaps in the most packed atomic plane. Also, it ensures that there is no atomic overlap along any crystallographic direction. It should be noted that a_0 is a function of simulation conditions. In order to perform this calculation, a set of NPT ensembles were simulated with EAM and LJ potentials for a cubic system of silver. The simulation parameters were the same as those for the calculation of $g(r)$. By measuring the length of the simulation boxes' edges and dividing it by the number of the unit cells along each edge, an average value was calculated for a_0, which was found to be 4.1192 Å, and 4.1008 Å for the systems with EAM and LJ potentials, respectively. These values result in 7.3473 Å^2, and 7.2818 Å^2 for A_a in the systems governed by EAM and LJ potentials, respectively.

Although the method seems to work correctly, it cannot be used in all situations. For instance, when a system is partly or entirely in amorphous structure, the definitions of crystallographic parameters such as a_0 are not valid anymore. Furthermore, the visualization of the atoms might also be important in the process of detection of contacts, like in the projection of the non-contacting atoms method. In such cases, an atom can be represented by a sphere; therefore, a definition for its radius would be inevitable. Following the previous discussion, $g(r)$ would be the best reference to consult for this

definition; the distances on $g(r)$ plots can be considered as the atomic diameters (d_a). Defining d_a as the distance where the first peak of a $g(r)$ plot begins (d_s) ensures that there will not be any overlaps between the atoms, but this will result in large gaps. Also, considering d_{fn} and d_a as being equal reduces the number of gaps, but increases the number of overlaps at the same time. As one may argue, the first peak of a $g(r)$ plot (d_{fp}) refers to the distance where two atoms have the highest probability of being in contact. Therefore, considering $d_{fp} = d_a$ results in a balance between the gaps and overlaps for a spherical representation of the atoms. The values of d_{fp} can be found in Table 3.5.

In this chapter, the atoms were represented as spheres with radii calculated from the data provided in Table 3.5, and πr^2 was used to calculate the corresponding A_a values.

Table 3.5 The values of d_{fp} in Å for silver, lead, and platinum.

	Ag	Pb	Pt
EAM	2.903	3.503	2.768
LJ	2.903	3.503	2.783

3.6 Results and discussion

3.6.1 Method A: projection of the non-contacting atoms

No definition is necessary for d_c to detect contacting atoms via their potential energies; only the value of PE_c is necessary, which can be measured from a calibration test. This was done through a simulation of a spherical silver particles with a radius of 50 Å and a stepped geometry (see Figure 3.5), equilibrated at 300 K. The first step of the analysis of the crystalline spherical particles was done by applying the adaptive common neighbor analysis (a-CNA) [43]; all of the fcc crystalline atoms were removed, and an atomic shell remained. Figure 3.6 (a) shows the potential distribution of the remaining atoms. The potential energy distributions were divided into different regions with respect to the atomic positions, such as corners, edges, surfaces, and

partial contacts. The partially contacting atoms are recognized by their white color in Figure 3.6 (b), which illustrates two adjacent (111) planes of the shell. The atoms in the corners and edges of the higher plane are in contact with some of the atoms of the lower plane, which are labeled according to Figure 3.6 (a); these atoms should not be considered as surface atoms. Therefore, consulting the potential energy distribution, i.e. Figure 3.6 (a), the PE_c should be defined in a way so as to differentiate the atoms with partial contacts, labeled as (ι, I) and (κ, K), from the rest. This value was found to be -2.505 eV, and -2.080 eV for EAM and LJ potentials, respectively.

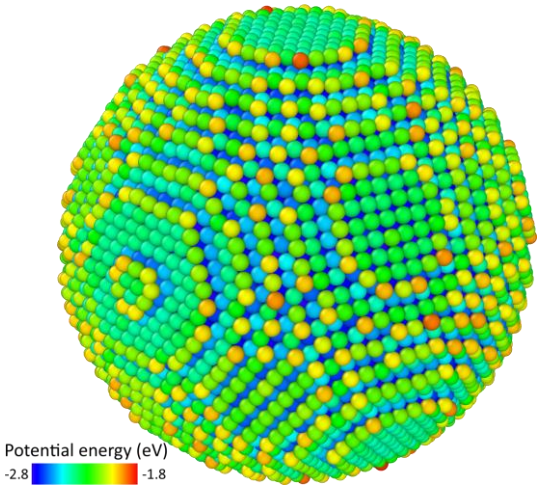

Figure 3.5 The silver spherical particle with a stepped geometry, equilibrated at 300 K, and governed by the EAM potential. The atoms are colored using their potential energy values.

In order to project the non-contacting atoms of the substrate, the spherical particles' atoms were removed in the first step of visualization; otherwise, they would cover the contact area of the substrate, and make it invisible. Then, the atoms with potential energy lower than the PE_c, i.e. the contacting atoms and the atoms in the bulk, were removed, and a top-view snapshot normal to the z axis was taken. Figure 3.7 depicts the substrate in contact with the different spherical particles. As the figure shows, it seems that there are some contacts at the edges of the substrate; however, those are generated because of some perturbations on the surface. Those perturbations were the results of the atomic reconfigurations in the substrate allowing for atoms to change their positions during relaxation. Therefore, these perturbations having a thickness

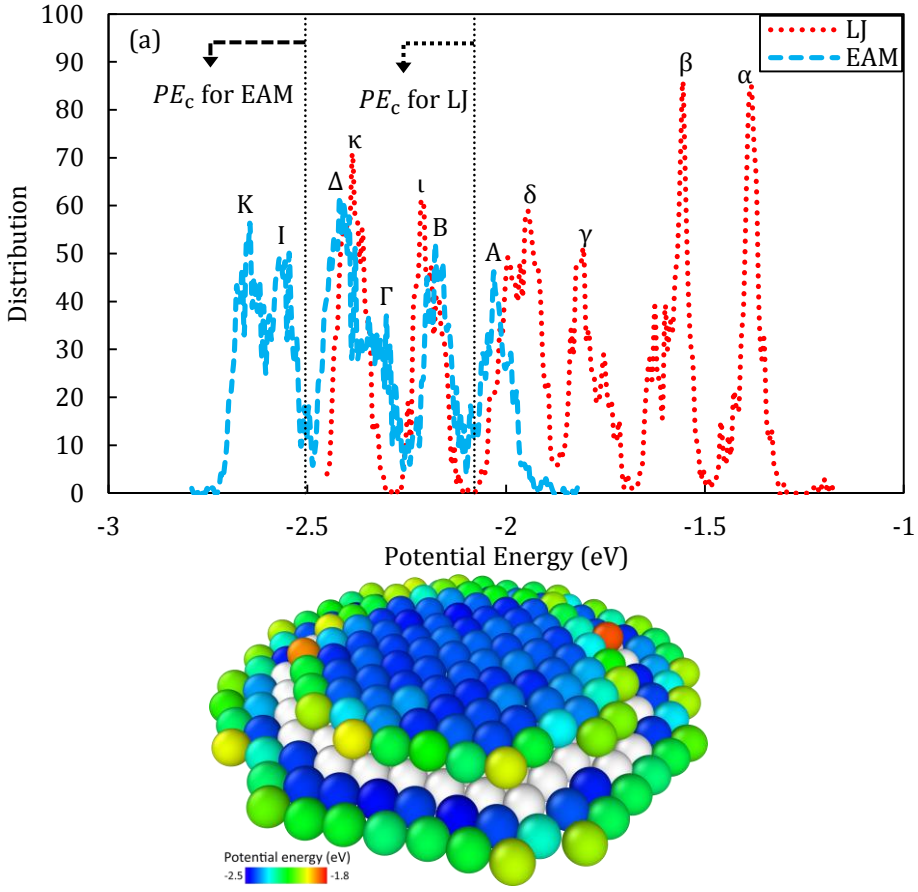

Figure 3.6 (a) The potential energy distribution of the shell atoms of the crystalline silver spherical particles. The vertical lines indicate the values that divide the partially contacting atoms from the rest, i.e. PE_c. The atomic potential energy values depend on the governing potential energy model. Moreover, these values are dependent on the atoms' positions. In this figure, the distribution of atoms at the corners, edges, (100) planes, and (111) planes are labeled as (α, A), (β, *B*), (γ, Γ), and (δ, Δ), respectively. The two peaks with the lower energies correspond to the atoms in partial contact with corners and edges and are labeled as (ι, I) and (κ, K), repectively. (b) Close-up of the top two atomic (111) planes of the shell atoms depicted in Figure 3.5. The atoms are colored using their potential energy values, except for the white colored ones; as can be noticed, these are in contact either with the atoms at the corners (peak I) or the edges (peak K) of the upper layer.

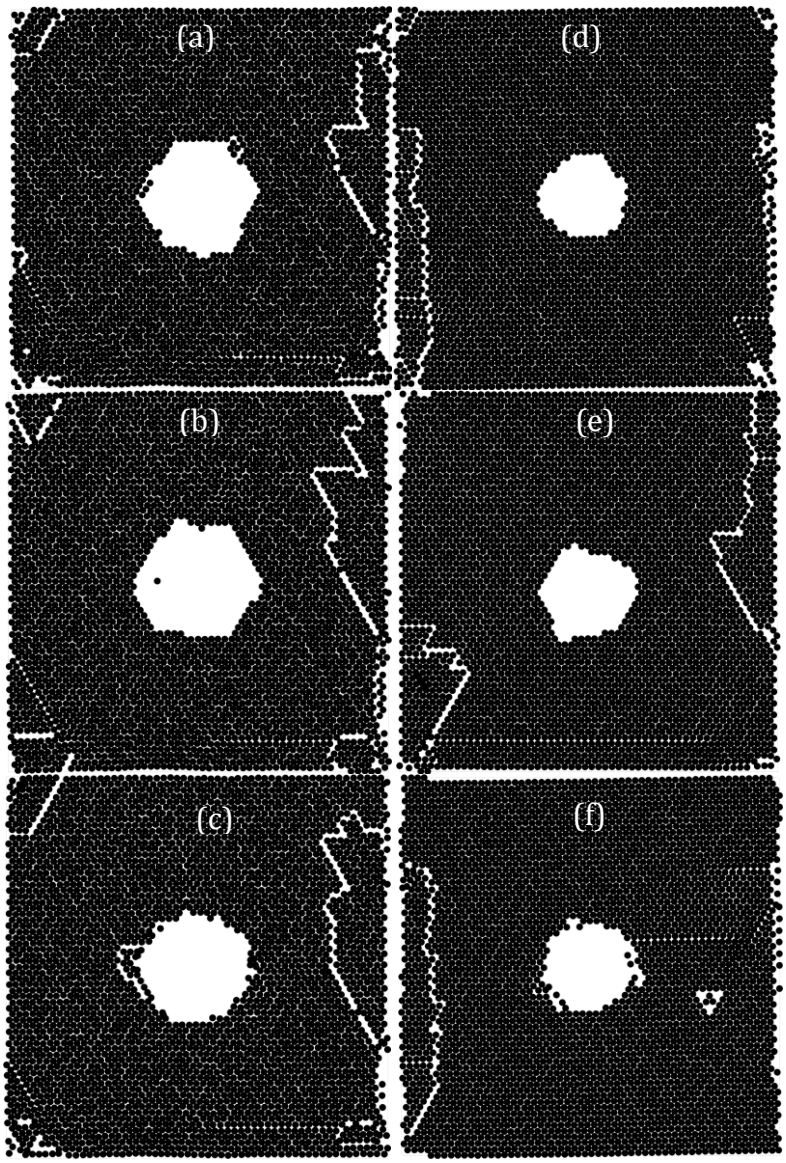

Figure 3.7 The black dots represent the non-contacting silver atoms of the substrate in contact with the different spherical particles: silver (a, d), lead (b, e), and platinum (c, f), governed by EAM (a-c) and LJ (d-f) potentials.

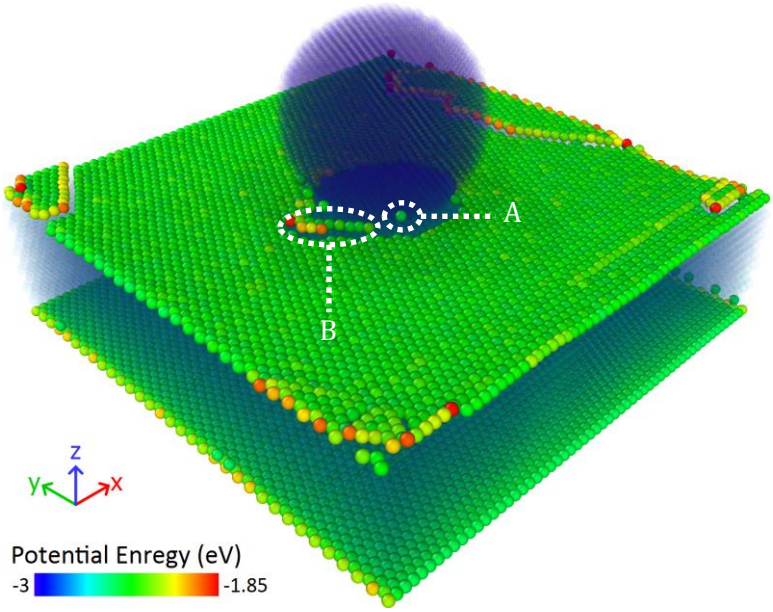

Figure 3.8 The atomistic system of the platinum spherical particle in contact with a silver substrate. The atoms are colored based on their potential energy values. The solid atoms indicate those atoms of the surface which have a potential energy higher than PE_c, and the rest are made transparent. Atom A is an example of a contacting atom, even though it is not detected as being one. Section B shows the atoms which are considered as being in contact; however, these are partially in contact with the atoms of the substrate itself due to an atomic step generated adjacent to the actual contact with the spherical particle.

of one atomic layer are related to 'contacts' within the substrate itself and not with the spherical particles. This means that, with this method, the contact region should be known beforehand, in order to remove the unwanted sections from the analyses; however, this is not always an easy task to do. For instance, in the systems with platinum spherical particles, some irregularity around the contacts can be noticed which is related to the atomic steps generated on the substrate around the spherical particle because of some vertical movements of silver atoms. This can be seen in Figure 3.8. In such a case, it is not easy to distinguish between these two different kinds of contacting atoms.

Moreover, Figure 3.8 shows that some of the silver atoms that were in contact with the spherical particle were not detected as being in contact based on their potential energy. This behavior is related to the potential energies

between atoms of different materials: the interatomic potential energy between two atoms should be low enough to decrease the potential energy of the targeted atoms to a value lower than the PE_c; otherwise, the atoms cannot be detected as contacting ones. This shortcoming is not limited to the systems with different types of atoms, but can also be seen when the contacting atoms are very few in number; the most extreme case would be when a corner atom (see Figure 3.6) is in contact with one atom of the substrate. In such a case, the potential energies of the contacting atoms would not become lower than PE_c. Therefore, the contact would not be detected.

Figure 3.7 was analyzed, and the values of A_{real} were estimated with the results summarized in Table 3.6. One of the difficulties in the analyses of these figures is the occurrence of gaps between the atoms. Focusing on the contact area reduces potential errors from the presence of the gaps. It should be noted that, in the contact area where the atoms are removed, i.e. the white sections in the middle part of the projected atoms in Figure 3.7, there were gaps between the contacting atoms that are not distinguishable, even though the contacting atoms are not shown. In other words, the overestimation of the contact area is an intrinsic feature of this method. It might be possible to introduce some mathematical steps which could be taken to modify the results, but this is not the purpose of the present study.

Table 3.6 The measured values of A_{real} from the projection of the non-contacting atoms onto a xy plane.

Particle	A_{real} (Å^2)	
	EAM	LJ
Ag	1868.3	1056.9
Pb	2055.3	1256.2
Pt	1796.8	1217.9

3.6.2 Method B: counting the contacting atoms

The real contact area can be estimated via $N_{ca}A_a$ by detecting and counting the contacting atoms of the sample. Using the d_{fn} values reported in Table 3.3, the contacting atoms in each system were detected. Then, they were counted, and the corresponding contact areas were calculated. The top views of the contacting atoms are depicted in Figure 3.9, and the calculated contact area values are reported in Table 3.7. The results indicate that applying the LJ potentials results in a smaller number of detected contacting atoms in comparison with the systems where the EAM potentials were applied. This is a consequence of the essential differences between the LJ and EAM potentials, which directly affect the inherent interactions between atoms as captured in their contact distances and potential energy cutoffs. For example, using a common contact distance d_{fn} for both EAM and LJ systems would still result in a larger contact area for EAM systems due to the different interatomic interactions captured by the EAM potential. Therefore, the prediction of a larger contact area, manifested via the detection of higher numbers of contacting atoms, is due to the definition of the EAM potential.

Table 3.7 The number of contacting atoms (N_{ca}) in contact with the spherical particles. The values of A_{real} are calculated based on N_{ca} of the substrate

Particle	N_{ca} of particle		N_{ca} of substrate		$A_{\mathrm{real}}(\text{Å}^2)$	
	EAM	LJ	EAM	LJ	EAM	LJ
Ag	237	119	272	141	1799.7	932.9
Pb	173	104	280	168	1852.6	1111.6
Pt	360	180	320	165	2117.3	1091.7

3.6.3 Method C: measuring the contact energy

In this method, the estimation of the real contact area can be performed by dividing the interaction energy between the two counterparts, U, by the interaction energy per area between them, Δ. In other words, Δ represents the

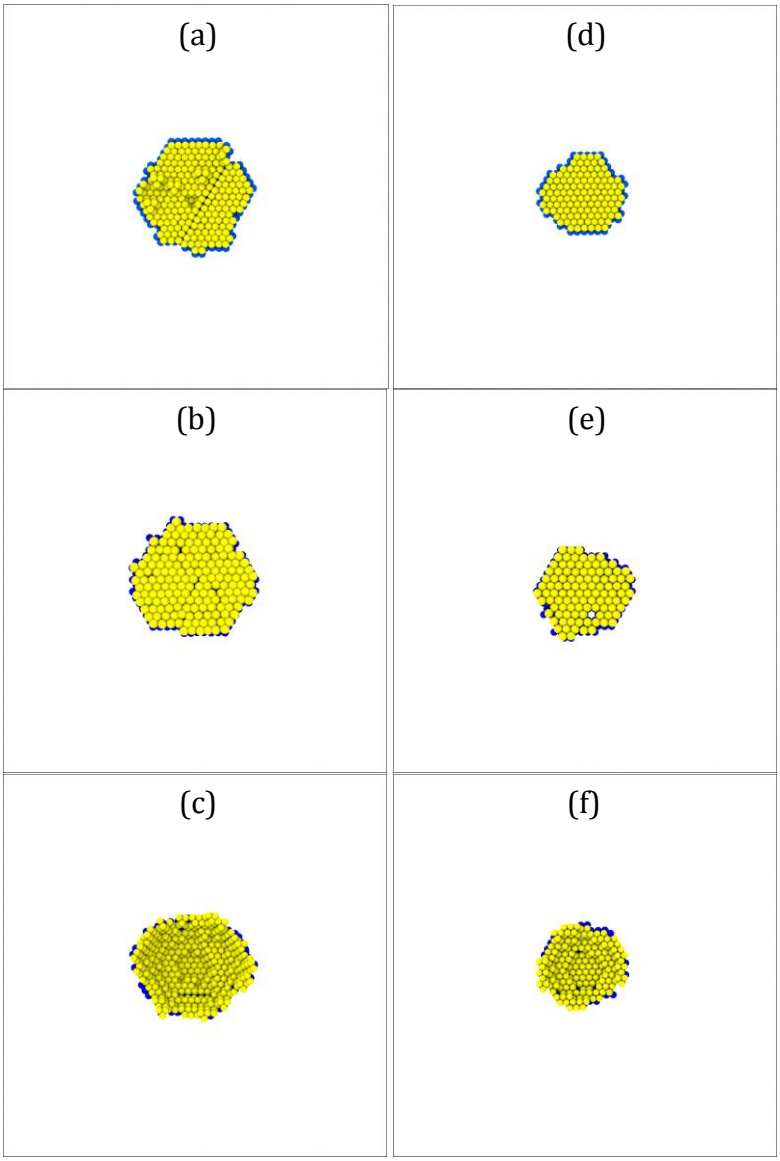

Figure 3.9 The contacting atoms of the substrate and the spherical particles: silver (a, d), lead (b, e), and platinum (c, f), governed by the EAM (a-c) and LJ (d-f) potentials. The non-contacting atoms are not depicted. The atoms of the substrate and spherical particles are colored as blue (darker) and yellow (lighter), respectively.

interaction energy between the counterparts for a unit area, and by measuring the interaction energy in the simulation, U, the real contact area can be estimated via $A_{\text{real}} = U/\Delta$. The value of Δ can be estimated by equilibrating a system consisting of two contacting bodies with a known contact area. But, how can the real contact area be known from the beginning? This shortcoming suggests that this method cannot be applied independently. Wenner [67] defined this value as the nominal contact area; however, from the previous discussion, it is known that the nominal contact area is not an acceptable value for calculations in the atomic scale. For the estimation of Δ, the interaction energy between the two blocks should be divided by the real contact area. In this study, method **B** was utilized to do this, as follows: the contacting atoms between the blocks were detected and counted based on their distances (yielding N_{ca}), and the corresponding contact areas were calculated as $A_{\text{real}} = N_{ca}A_a$. Then, Δ was calculated as the ratio of the potential energy U to A_{real}. A summary of the results of these simulations can be found in Table 3.8.

Table 3.8 The interaction energies between the contacting atomic blocks (eV), the equilibrated nominal contact area (Å^2), and the corresponding value of the interfacial energy per area between the counterparts.

Upper block	U		A_{real}	$\Delta = U/A_{\text{real}}$	
	EAM	LJ		EAM	LJ
Ag	−539.38	−1477.89	5293.3	−0.102	−0.279
Pb	−390.41	−930.72	6351.9	−0.061	−0.147
Pt	−1659.15	−4418.65	11115.9	−0.149	−0.398

The calculation of Δ was done by performing a number of NPT ensemble simulations, in order to keep the temperature and pressure at certain values. The simulation settings were the same as the ones described in the simulation methodology section, with some modifications. The simulation box was divided into two blocks: the bottom one was filled with silver atoms, and the top one with either silver, lead, or platinum, in each simulation. The temperature and pressure were controlled via the algorithm developed by Shinoda et al. [76] to keep the system at 300 K under an external pressure of 0 GPa. Moreover, different lateral sizes were used for simulation boxes of

different pairs of blocks, i.e. 57.84 Å × 50.09 Å, 57.84 Å × 60.11 Å, and 60.73 Å × 100.18 Å for silver/silver, silver/lead, and silver/platinum systems, respectively. This was done to lower the crystallographic defects in the lateral directions [65]. The initial lateral sizes of simulation boxes can be found in Table 3.9. For the estimation of Δ, the interaction energy between the two blocks should be divided by the real contact area, while the mean value of the interaction energy was calculated as U. The results can be found in Table 3.8.

The negative values of U indicate the attractive energy between the blocks. It should be noted that, for the systems simulated with EAM potentials, the interaction energy values were lower than for the ones with LJ potentials. The reason for this is the intrinsic shortcoming of the method, due to its definition which is based on pair-wise interactions. In other words, in a system where the potential formulation between the two atomic blocks is not in the form of a pair-wise potential, this method is not applicable, unless the potential consists of such a portion, as in the case of EAM potentials. In such cases, only the pair potential portion, i.e. $\varphi_{ij}(r_{ij})$, will be taken into account.

In order to apply this method, the interaction energy between the spherical particle and the substrate was measured for each system, and its mean value was divided by the corresponding Δ. The values of the measured U and estimated A_{real} are reported in Table 3.10.

Table 3.9 The initial lateral simulation box sizes in Å

Upper block	x	y
Ag	57.84	50.09
Pb	57.84	60.11
Pt	60.73	100.18

3.6.4 Discussion on the methods and their results

The estimated values of A_{real} using different methods are summarized in Figure 3.10. As can be seen, all of the tested contact detection methods have estimated a lower value of A_{real} for the systems governed by LJ potentials. In an MD simulation, it is crucial to select appropriate potential energies that can

correctly describe the system's behavior. The embedded atom method potential [69] is widely considered to be accurate for metallic systems since it is not a pure pairwise potential, but also takes the electron density around each atom into account. Therefore, the potentials used in this chapter are fundamentally different, which resulted in large differences between the contact areas for each.

Table 3.10 The interaction energies between the spherical particles and the substrate, and the real contact area.

Particle	U (eV)		A_{real} (Å^2)	
	EAM	LJ	EAM	LJ
Ag	−153.02	−223.32	1501.7	799.9
Pb	−101.83	−145.92	1656.8	995.9
Pt	−296.96	−415.61	1989.6	1045.5

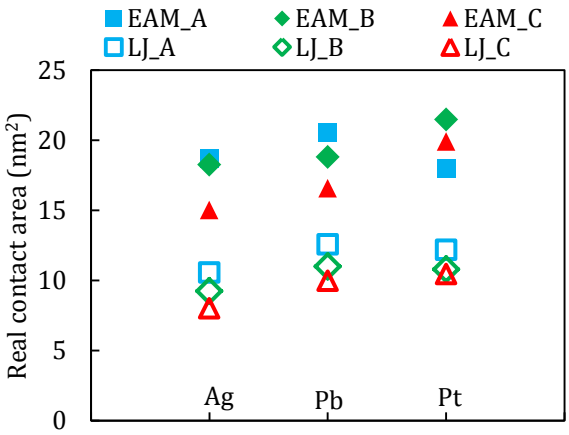

Figure 3.10 A comparison between the estimated real contact area via different methodologies, i.e. (**A**) projection of the non-contacting atoms, (**B**) counting the contacting atoms, and (**C**) measuring the contact energy.

As can be expected, method **A**, i.e. the projection of the non-contacting atoms, showed the highest estimated values of A_{real}, due to its intrinsic overestimation, except for the platinum spherical particle with the EAM potential. The reason for that is the shape of the contact zone. As illustrated in Table 3.11, the contact area is almost flat for all cases, except for the Pt/Ag contacts; as a result of the adhesion forces between the platinum spherical particle and the silver substrate, the substrate experienced deformations around the contacting spherical particle, as illustrated in Table 3.11. Because of the curved shape of the contacting atoms, their projection results in a smaller estimation of the contact area than the other two methods which are not related to the projection of atoms.

The resulting areas from method **C** were smaller than those from method **B** in all cases; they were almost the same for the systems with LJ potentials, but the differences were noticeable for the systems with EAM potentials. This behavior was to be expected, as the measured value of the contact energy contained only the pair potential part of the EAM formulation; therefore, some part of the energy, which had its own effects on the behavior of the system, was always missing from the calculations.

The estimated values of A_{real} via method **B** were between the results from the other two methods, except for the platinum spherical particle with EAM potentials. Unlike method **A**, this method is not related to the projection of the contacting atoms; therefore, the resulting areas were lower than method **A**. Moreover, because of atomic vibrations, the interaction energy between the counterparts is fluctuating, which is why its mean value was used in method **C**. On the other hand, the contact distance in method **B** was selected to be large enough to overcome the influence of atomic vibrations. As a result, this method estimated higher values of A_{real} compared to method **B**.

Table 3.11 Side view of the contacting atoms detected by the contacting distances for all studied system.

Particle	EAM	LJ
Ag	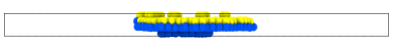	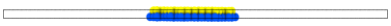
Pb		
Pt	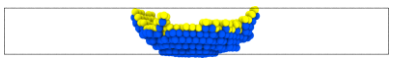	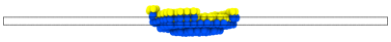

3.7 Summary and Conclusions

The results of this chapter demonstrate the complexity of measuring the contact area in atomistic simulations for a very simple geometry. In this chapter, previously published methods for the estimation of the real contact area in atomistic simulations (see Table 2.2) were reviewed and modified where necessary. Two different potential energies were used to govern the systems: LJ and EAM. The systems with LJ potentials showed lower values of the contact area than the systems with EAM potentials, regardless of the utilized method. Also, the differences between the estimated values for the systems with LJ potentials were smaller than the differences for the systems with EAM potentials. These results suggest that the governing potential energies of a system have a dominant effect on every aspect of its behavior, including the real contact area.

A few parameters should be defined before applying the methods to estimate the contact area, namely the contact distance, and the area of an atom. The results of the current study show that the statistical radial distribution description of the system, as depicted in a $g(r)$ plot, is a reliable tool for defining the contact distance between two similar atoms, with the distance where the first minimum occurs defined as the contact distance. Moreover, a mixing rule, such as the one proposed by Waldman and Hagler [72], can be used to define the contact distance between two dissimilar atoms. While it is common to use the distance at the minimum of the LJ pair potential energy as the contact distance, the current study shows that this value is not accurate, because this definition does not take the effect of atomic vibrations into account. Considering this effect, a larger value should be used for the contact distance. In order to identify the contact distance, more detailed investigations are needed; however, the following weighted average value is in good agreement with the value extracted from the $g(r)$ plots: $\overline{r} = (r_{\mathrm{E}} + \theta r_{\mathrm{F}})/(1+\theta)$, with $\theta = T/T_{\mathrm{m}}$ and temperatures in Kelvin. Regarding the area of an individual atom, it is common to represent atoms as spheres in atomistic simulations; therefore, the definition of the atom's radius crucially affects the results. Our study suggests that the $g(r)$ plots could augment this definition: the distance between the first peak of a $g(r)$ plot and the origin is defined as the atom's diameter.

The estimation of the contact area could be done via one of the three different methods, with their advantages and limitations summarized as follows:

1- Method **A**, i.e. the projection of the non-contacting atoms, can be used safely in a system where the atoms are from similar elements. In such a case, as soon as the counterparts are in contact, the potential energy of the atoms in contact drop to the bulk potential energy value; then, the contacting atoms can be differentiated from the surface atoms with ease (see Appendix A). On the other hand, the contact between different elements can make the contacting atoms unidentifiable. Afterwards, the contacting atoms would be removed from the visualization, and the non-contacting atoms would be projected in a desired plane, e.g. normal to the applied force. A disadvantage of the method is that the contact region should be known beforehand; otherwise, it is probable that surface perturbations, which are not related to the contacts between the counterparts, will be erroneously included in the results. Moreover, this method suffers from an intrinsic overestimation of the contact area, which is related to the gaps between the visualized atoms in their projection. Based on the features of the method, it would work best when the elements of the counterparts are the same, and when the projection of the contact area is needed, e.g. for calculation of the normal force [66].

2- Method **B**, i.e. counting the contacting atoms, applies to the real contact area and not the projected one. In other words, if the contact area contains some curvature(s) (e.g. see Table 3.11), the curved area would be larger than its projection. In this method, the contacting atoms should be detected based on the distances between the atoms of the counterparts. Subsequently, the contacting atoms would be counted, and the real contact area estimated via $N_{ca}A_a$. This method is reasonable for the calculation of A_{real}; however, possible atom transfer between the counterparts limits the usability of the method for studying sliding systems. In addition, if the projected area is needed, the projection of the detected contacting atoms on a desired plane could be used.

3- Method **C**, i.e. measuring the contact energy, estimates the real contacting area based on the pair potential energies that the counterparts exert on each other. Therefore, detection of the contacting or non-contacting atoms does not play a role in this method. It should be noted that the calculation of Δ is an intrinsic weakness of the method; in order to calculate this value, the area of the contact in the calibration test should be known. In this study,

method **B** was used to solve this problem, which means that this method is dependent on, and suffers from the errors of the other methods. Also, the estimation of the real contact area depends on the potential energy formulation used in the system. If the governing potential is a pair-wise one, the method works well; however, if this is not the case, this method uses only the pair potential portion: if the potential formulation does not have a pair-wise portion, this method cannot be used. Moreover, if the projected area is needed, this method cannot be of help, because it does not yield any information about the contacting atoms. See Appendix B for the applicability of this method.

The results and discussions of the present study suggest that method **B**, i.e. $A_{\text{real}} = N_{ca}A_a$, is most suitable to estimating the real contact area (and not its projection), as long as the contact distance is constant. Moreover, this method captures all necessary components of the potential energy formulation, and not simply its pair potential.

This page is intentionally left blank.

Chapter 4 *

Continuum mechanics at the atomic scale: insights into non-adhesive contacts using molecular dynamics simulations

Classical molecular dynamics (MD) simulations were performed to study non–adhesive contact at the atomic scale. Starting from the case of Hertzian contact, it was found that the reduced Young's modulus E^* for shallow indentations scales as a function of, both, the indentation depth and the contact radius. Furthermore, the contact of two representative rough surfaces was investigated: one multi-asperity, Greenwood-Williamson-type (GW-type) rough surface –where asperities were approximated as spherical caps–, and a comparable randomly rough one. The results of the MD simulations were in agreement for both representations and showed that the relative projected contact areas A_{rpc} were linear functions of nominal applied pressures, even after the initiation of plastic deformation. When comparing the MD simulation results with the corresponding continuum GW and Persson models, both continuum models were found to estimate the values of A_{rpc} relatively close to the MD simulation results.

4.1 Introduction

One of the most important factors investigated in tribological studies is the real contact area A_{real}, which is typically much smaller than the nominal contact area A_0, due to the roughness of the contacting surfaces. As described in the previous chapter, in macroscopic experiments, the real contact area of the contacting asperities can be usually described as $\sum A_{\mathrm{asp}} = F_{\parallel}/\bar{\tau}$, where $F_{\parallel}$ is the friction force, and $\bar{\tau}$ is the effective shear strength of the contacting bodies. On the other hand, in continuum contact mechanics models, the contact area is typically defined as a function of separation, normal force, or nominal

* This chapter has been originally published in Journal of Applied Physics **120** (2016) 215102.

pressure. While such continuum models were developed for macroscopic contacts, advancements in nano-sized devices required researchers to extend continuum theories to the nanoscale. Nevertheless, the atomic resolution of nano-contacts with its inherently discreet nature goes against one of the essential assumptions of continuum theories, namely that the contacting surfaces are continuous. This problem led researchers to study nano-contacts by means of atomistic computer simulation methods, such as molecular dynamics (MD).

MD simulations have been used to describe the contact behavior at different situations: normal or sliding contacts, flat or rough surfaces, with or without adhesion, with or without lubricant, and so on [66, 77-81]. Some researchers went further to compare their simulation results with relevant continuum models; however, discrepancies between the two resulted in a number of extensions to continuum models such as developing an extended version of the Johnson-Kendall-Roberts (JKR) theory [2, 14], and proposing a three-parameter friction law [9]. In a detailed investigation by Luan and Robbins, the breakdown of continuum models for mechanical contact at the atomic scale was demonstrated [3] to be due to the inherent atomic roughness at the contacts; however, Mo et al. [4] later argued that the definition of the real contact area needs to be corrected for the atomic scale, which will result in comparable results with the relevant continuum models. They defined the real contact area as $A_{\mathrm{real}} = N_{ca} A_a$, where N_{ca} is the number of contacting atoms, and A_a is the projected area of an individual atom. In chapter 3, different methods for identifying the contacting atoms were further investigated, and argued that the most suitable method for doing so is based on atomic distances, i.e. two atoms are identified as being in contact if their pair-distance is closer than a contact distance d_{c}. Moreover, it was discussed that the $g(r)$ curves, depicting the normalized radial distribution function of the system, can be used to define this contact distance as well as the diameter of an individual atom in an adhesive contact.

While the definition of the adhesive contact distance was investigated in detail previously (see chapter 3), the non-adhesive contact distance is not well defined but is very relevant in direct comparisons between atomistic simulations and non-adhesive classical continuum theories. An atom can be identified as being in contact if it is acted upon by a non-zero force from the counterpart. This force-based definition can be translated into a distance-based one in which the governing potential energy needs to be considered. While such definitions have been widely adopted, there is a lack of validating investigations, especially with regard to widely accepted continuum theories.

4.2 A short review on non-adhesive contact mechanics

Different models have been developed for analyzing non-adhesive contact mechanics, which share some common assumptions: the surfaces are continuous and smooth, each solid can be considered as an elastic half-space, and the strains are small for elasticity to be valid [25]. Moreover, most of the models assume frictionless contact.

The first successful model for analyzing non-adhesive contacts between two solids was published by Hertz [24] (see, e.g., [25] for a review). This model was later adapted and made applicable to adhesive contacts as well, e.g. in the classical JKR [14] and Derjaguin-Muller-Toporov (DMT) [15] theories. Furthermore, the Hertz theory was utilized by Greenwood and Williamson (GW) [82] in their well-known study of rough surface contact, while a 'competing' contact mechanics model of rough surfaces was introduced and further developed by Persson [83, 84]; the applicability and limitations of the GW-inspired and Persson models are still debated [85].

4.2.1 The Hertz model

Hertz analytically solved the contact mechanics problem of elliptical point contacts [24]. Assuming the same values of principle radii of curvature for each surface, the area of contact will be circular; therefore, the two contacting surfaces have two radii of curvature of R_1 and R_2, and $R = (R_1^{-1} + R_2^{-1})^{-1}$ would be the relative radius of contact. For such a contact, Hertz proposed a pressure distribution of the form $p(r) = p_0(1 - (r/r_c)^2)^{0.5}$, where r is the radial distance of the contact (with 0 at the center of the contact), p_0 is the maximum compressive pressure, and r_c is the radius of the contact area projected on a plane normal to the applied load. The proposed pressure distribution results in the following relations:

$$r_c = \left(\frac{3F_\perp R}{4E^*}\right)^{1/3}, \tag{4.1}$$

and

$$p_0 = \left(\frac{6F_\perp E^{*2}}{\pi^3 R^2}\right)^{1/3}, \tag{4.2}$$

with

$$E^* = \left(\frac{1 - \nu_1^2}{E_1} + \frac{1 - \nu_2^2}{E_2} \right)^{-1}, \tag{4.3}$$

where $F_\perp$ is the normal applied force, and E_i and ν_i are the elastic modulus and the Poisson ratio of the contacting bodies. Moreover, the normal applied force relates to the indentation depth via $F_{\mathrm{H}}(d) = 4/3\, E^* R^{0.5} d^{1.5}$.

4.2.2 The GW model

Greenwood and Williamson analyzed the non-adhesive contact between rough surfaces by applying Hertzian theory [82]. In their model, the contact of two rough surfaces was simplified as one equivalent elastic rough surface contacting a rigid flat, under the assumption that the final rough surface has an isotropic normal height distribution. Then, they modelled the rough surface as a distribution of N asperities having spherical caps with a constant radius. Their original model was developed for non-adhesive and elastic contacts, and ignored all types of interactions between the asperities. At any given separation s, defined as the distance between the rigid surface and the mean value of the asperity heights, the GW model describes the projected contact area A_{GW} and the contact normal force F_{GW} as functions of separation as follows:

$$A_{\mathrm{GW}} = N \int_s^\infty A_{\mathrm{H}}(h - s) P(h)\, \mathrm{d}h, \tag{4.4}$$

and

$$F_{\mathrm{GW}} = N \int_s^\infty F_{\mathrm{H}}(h - s) P(h)\, \mathrm{d}h, \tag{4.5}$$

where h is the asperity height, $(h - s)$ represents the indentation depth of an asperity, A_{H} and F_{H} are the projected contact area and the normal compressive force of each asperity, respectively, calculated from the Hertz model, and $P(h)$ is the height distribution.

4.2.3 The Persson model

Persson developed a multiscale contact theory by applying a diffusion-like formula to implement scale dependency to his model, which relates the projected contact area of a rigid rough surface contacting an elastic flat surface

to the applied pressure [83, 84]. The theory was originally developed for non-adhesive contacts, where the rough surface is a quasi self-affine one with an isotropic and normal height distribution. Before the description of the model, let us define the relative projected contact area ratio as $A_{\mathrm{rpc}} = A_{\mathrm{pc}}/A_0$, where A_{pc} is the projection of the real contact area on a plane normal to the applied load, and is not to be confused with the area A_{H} calculated from the Hertz model, and A_0 is the apparent contact area, i.e. $L_x \times L_y$, where L_x and L_y are the lateral lengths of the contacting system.

In this theory, the projected contact area A_{Persson} is a function of an arbitrary length scale λ, assuming that the original surface is smooth at all length scales below λ [86]. This length scale is defined as $\lambda = L/M$, where M is called the "magnification level", and $M \geq 1$. The magnification level controls the length scale λ, so that λ is the shortest wavelength of roughness that can be resolved at magnification M [12]. Although, in theory, the value of λ is bounded by the distance between two neighboring atoms, in practice its value cannot be smaller than the lateral resolution of scanning instruments.

In an elastic contact, the relative projected contact area at a given magnification is defined as $A_{\mathrm{rpc}} = \int_0^\infty P(p)\,dp$, where p is the interfacial contact pressure, and $P(p)$ is the probability distribution of p. Persson solved his model, which resulted in the normalized area of real contact

$$A_{\mathrm{rpc}} = \mathrm{erf}\left(\frac{P_0}{2\sqrt{G}}\right), \tag{4.6}$$

with $P_0 = F_\perp/A_0$. The magnification dependent "diffusion coeffiecient" G was obtained, both, analytically [83, 84] and numerically [12]. Figure 4.1 shows a typical power spectral density (PSD) of a quasi self-affine rough surface. For such surfaces, the value of G can be calculated from

$$G = \frac{\pi}{4} E^{*2} \int_{q_{\mathrm{L}}}^{M q_{\mathrm{L}}} q^3 C(q) \mathrm{d}q, \tag{4.7}$$

where $C(q)$ is the PSD of the surface, and q is the wavenumber. Note that $M q_{\mathrm{L}} \leq q_{\mathrm{S}}$, where $q_{\mathrm{L}} = 2\pi/L$ and $q_{\mathrm{S}} = 2\pi/2\delta$ are the wavenumbers corresponding to the largest and shortest wavelengths, respectively, with δ being the shortest distance between two sampled neighboring point. Comparing (4.7) with the second moment of the PSD, it can be shown that $G = 1/8\, E^{*2} \langle |\nabla h|^2 \rangle$ (e.g. see [87, 88]), where $\langle |\nabla h|^2 \rangle$ is the mean square gradient of the surface. It should be noted that the values of G and $\langle |\nabla h|^2 \rangle$ are dependent on the magnification level M.

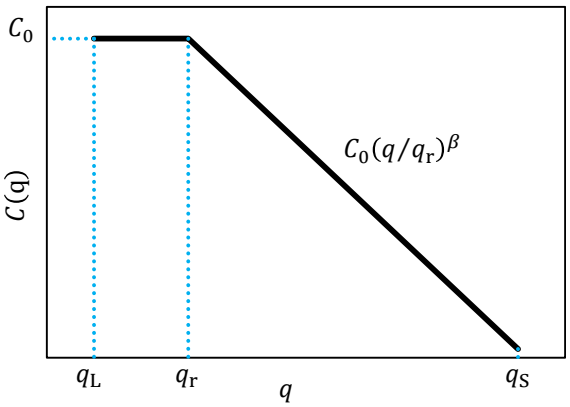

Figure 4.1 The schematic power spectral density of a quasi self-affine rough surface with an isotropic height distribution, plotted in a full logarithmic scale: C_0 is a constant, $q_L = 2\pi/L$ and $q_S = 2\pi/\delta$ are the wave numbers corresponding to the largest and shortest wavelengths, respectively, and q_r is the roll-off wavenumber.

The numerical approach was based on the fitting of a double Gaussian function of the following form to the interfacial stress distribution:

$$P(p) = \frac{1}{2\sqrt{\pi \bar{G}}}\left(\exp\left(-\frac{(p-P_0)^2}{4\bar{G}}\right) - \exp\left(-\frac{(p+P_0)^2}{4\bar{G}}\right)\right). \qquad (4.8)$$

Theoretically, $G = \bar{G}$; however, it was shown that the ratio $r = \bar{G}/G$ varies between 0.5 and 1, suggesting that the theoretical solution requires a correction factor [89].

4.3 Simulation methodology

4.3.1 Overview of numerical experiments

In order to examine the applicability of the Hertz, GW and Persson contact models at the atomic scale, three different systems had to be simulated separately: in the first one, a single asperity comes into contact with a flat substrate; in the other two, a flat substrate touches a GW-type rough surface and a randomly rough surface, respectively. Each of the systems were comprised of a rigid indenter, in the form of a single asperity or a rough

surface, and a deformable counterpart constructed from three different layers: (1) the two atomic layers farthest from the contact were fixed to resemble a rigid substrate and provide the needed support, (2) the next four atomic layers were assigned to be the thermostatic layer, and (3) the remaining atoms were Newtonian and formed the free layer. The various studied systems are summarized in Table 4.1. Although the geometrical structure of the systems was different in each case, all other parameters were the same in all simulations.

Table 4.1 A summary of the different types of the simulated systems in this chapter, and their placement in the results and discussion section.

System type	System snapshot	Placement in the text
Single asperity contact	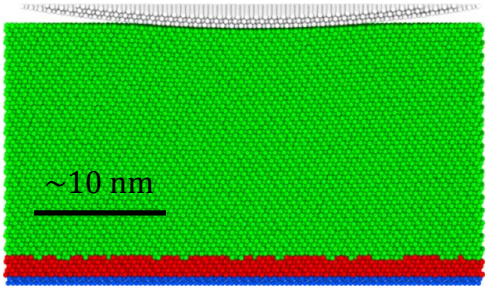	4.4.1 Single asperity contact size effects
GW-type rough contact	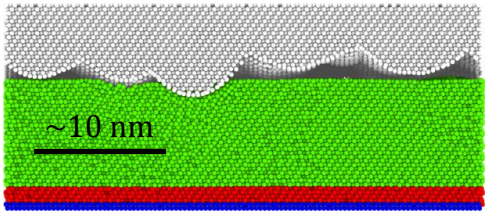	4.4.2.1 Multi-asperity rough contact: GW approximation
Randomly rough contact	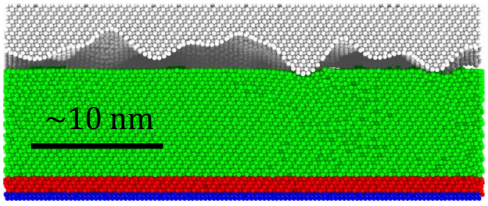	4.4.2.2 Randomly rough contact

Applying a step size of 10 fs [90], the equations of motion were solved via

the velocity-Verlet algorithm [38]. The temperature of the thermostatic layers was set to 300 K using Berendsen's thermostat [39]. The systems were equilibrated before the initiation of contact for ~0.5 ns. Moreover, in order to overcome the thermal fluctuations [6], the forces and pressure values were collected by averaging the values over 0.1 ps and 10 ps, respectively. The crystalline direction of [111] was defined as the z coordinate direction. Periodic boundary conditions were applied along the lateral directions. Aside from OVITO [40] and ImageJ [68], the post processing analyses were also done by means of a number of codes written explicitly for this purpose in MATLAB (The MathWorks, Inc., Natick, MA).

4.3.2 Potential energies

All of the systems in this investigation were generated of calcium with FCC crystal structure and a lattice parameter of $a_0 = 5.5884$ Å [91]. Two different types of potential energies were used in this study: one for the atoms of the deformable blocks, and one for the interactions between the counterparts. The atoms of each block were governed by the embedded atom method (EAM) potential [69] with the database developed by Sheng et al. for calcium [91].

In order to replicate a non-adhesive contact, only the repulsive part of the Lennard-Jones (LJ) potential [35] was used:

$$E(r) = 4\varepsilon(\sigma/r)^{12}, \tag{4.9}$$

where r is the distance between the two atoms, ε is the depth of the potential well, and σ is the distance where the potential energy is zero. The LJ parameters for calcium reported by Shu and Davies were used: $\varepsilon = 0.21445$ eV and $\sigma = 3.5927$ Å [71]. A cutoff radius of 3σ was applied to the potential. Moreover, the potential was switched off by applying the CHARMM potential switching function [92] from a starting radius of 2.5σ. The switch ensures that there is no discontinuity jump in the force field at the cutoff radius. Although a cutoff of 3σ was introduced to the potential, the potential energy would be negligibly small at distances slightly larger than the calcium lattice parameter. Considering the potential energy of the standard LJ formula at a conventional cutoff of 2.5σ, i.e. $E(2.5\sigma) \cong 1/60\ \varepsilon$, the repulsive part of the LJ potential shows almost the same value at a distance of ~5.7 Å $\cong 1.6\sigma$.

It should be noted that the indenter's response is a function of the applied interacting potential energy. See Appendix C for further investigations on this topic.

4.3.3 Single asperity contact

The Hertzian contact model was simulated by bringing a deformable substrate in contact with an atomistic rigid spherical cap. In order to investigate possible size effects, different radii, ranging between 15 Å and 1000 Å, were used for generating the spherical caps. The caps were generated by bending a crystalline slab: first a crystalline slab with a thickness of three atomic layers was generated, and then the atoms were shifted accordingly to follow the geometry of a spherical cap. In this manner, an atomically smooth surface was generated that would show the most comparable stress distribution conditions with Hertz continuum mechanics [3]. Moreover, the height of the spherical caps were equal to their radii for $R \leq 100$ Å, while it was ~110 Å and 15 Å for $R = 200$ Å and $R = 1000$ Å, respectively.

The size of the deformable substrates was different for different contact radii, in order to decrease the simulation time: each of the deformable parts contained 76700 atoms (for radii of 15 and 20 Å), 165056 atoms (for radii from 50 to 200 Å), and 570960 atoms (for the 1000 Å radius), respectively. The spherical cap was moved toward the substrate with a constant velocity of 1 m/s, with a total displacement of ~14 Å.

4.3.4 Multi-asperity contact

The GW contact model was investigated by bringing a rigid rough surface comprising multiple spherical asperity tips in contact with a deformable flat counterpart, as discussed in detail in section 4.4.2.1. It should be noted that, assuming no asperity interactions, there is practically no difference between the case where the rough surface is deformable and the flat one is rigid, as in the original GW model, and when the flat surface is deformable and the rough surface is rigid, as is implemented in this investigation.

First, a point cloud was created through generating a rough surface with an RMS roughness of 10 Å, a radius of 100 Å, and an asperity density of 0.001 $Å^{-2}$. The generated rough surface had 149 asperities. Then, the surface point cloud was used for constructing an atomic block. To do so, a crystalline cubic bulk with a lateral size of ~386.7 Å was generated, with [111] along its z direction. Then, the height of the surface point cloud was calibrated to have its minimum at a value of a_0. Finally, the positions of the atoms of the crystalline bulk were compared with the coordinates of the surface point cloud: the ones located above the surface point cloud were removed, and the remaining constituted a

crystal structure with a rough surface of minimum thickness of a_0. It should be noted that the surface point cloud itself was also added as an extra atomic layer to the top of the constructed substrate, in order to keep the substrate's surface the same as the generated one, with no stepped structure [65].

The counterpart was generated with the same lateral length, but with an atomically flat surface, and a thickness of 18.5 a_0, built from 364861 atoms. Because this flat counterpart was meant to be deformable, it was divided into three layers as described in section 4.3.1.

4.3.5 Randomly rough contact

A randomly rough contact was simulated for comparison with the multi-asperity contact and, later, with Persson's model. In order to generate a comparable randomly rough surface, first, the lateral correlation length ζ of the GW surface was calculated. Then, using the values of ζ and RMS roughness of 10 Å, a Gaussian randomly rough surface was generated following the method outlined by Bergström et al. [93]. The surface point cloud was used for building of a system with the same features as those described for the multi-asperity contact. Additional details are given in section 4.4.2.2.

4.4 Results and discussion

The results of the single asperity, multi-asperity, and randomly rough contacts are discussed in following sections.

4.4.1 Single asperity contact size effects

The force-displacement curves of a number of contacts with spherical cap indenters of various sizes are shown in Figure 4.2. The indenters were moved by controlling their displacement. The results show that larger indenters applied larger forces for the same displacement values. Moreover, a number of load drops are noticeable for all but the largest indenter. In the nanoindentation process, the first load drop indicates the onset of plastic deformation, which is a result of the nucleation of dislocations, and their movement and interactions; readers are referred to the literature [65, 94, 95] for detailed analyses on dislocations behavior during the nanoindentation process. As is shown in Figure 4.2, the plastic deformation was initiated at a larger penetration depth as a bigger indenter was used for the simulation.

When fitting the Hertz theory to the elastic part of the force-displacement curves, the reduced Young's moduli were found to be $E^*_{R=100\text{Å}} = 23.18$ GPa, and $E^*_{R=200\text{Å}} = 27.17$ GPa; however, the fitted constant values could not correctly describe the systems' mechanical behavior for the complete range of elastic deformation. The same trend of these results, i.e. the increase in E^* for larger indenters, and the inability of describing the contact behavior for the whole range of elastic deformation, can be found in the literature [95]. Therefore, instead of the conventional method of fitting the Hertz theory to the force-displacement curve, the mechanical behavior of the contacts was investigated through their pressure distributions and their comparison with the Hertzian solution (see section 4.2.1). It should be noted that the fitting process was done for the range up to and excluding the initiation of plastic deformation. Moreover, these simulations were used to define a contact distance for non-adhesive contacts.

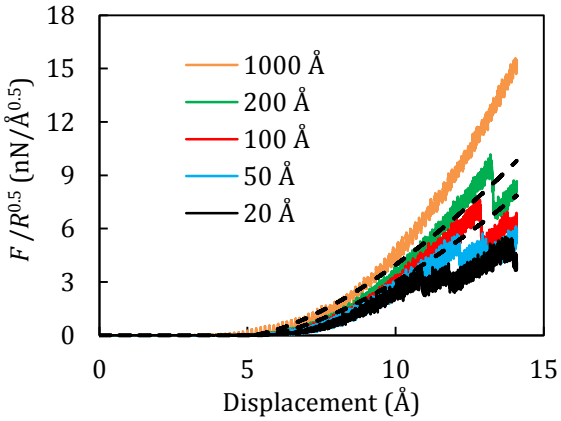

Figure 4.2 The variation on the normal forces, normalized by the indenters' radii, as a function of displacement. The reference point of the displacement axis is the initial position of the indenter. The dashed lines show the best fits to the curves of $R = 100$ Å and $R = 200$ Å, based on Hertzian theory. The sudden drops are indications of dislocation sliding in the systems, i.e. the initiation of plastic deformation [65].

4.4.1.1 The fitting procedure

In order to compare the results with Hertzian mechanics, two conditions were considered for extracting data from the simulations: first, the

deformation should be in the elastic regime, i.e. before the onset of plastic deformation, and, also, the stress field initiated at the contact should not extend beyond the substrate so that it could be fully enveloped within the simulation box (see Appendix D).

The Hertz formula for the contact pressure needed to be fitted to the values extracted from the simulations. To do so, the interfacial stress values of the indenters' atoms were calculated, and the values were saved with 2 decimal place precision. Then, all atoms that had non–zero interfacial stress were selected (see Figure 4.3 (a)). The distribution of the interfacial stresses showed two different patterns: one comparable with the Hertz theory, albeit with a "pressure tail" [12], and one with very low stresses distributed sparsely over the contact area. The pressure tail of the first pattern and the second pattern itself, both, have the same justification: the weak interfacial stress values are detectable in the atomistic model due to the applied long-range interaction between the contacting atoms, which is not considered in non-adhesive contact mechanics theories. The pressure tail results from the atoms that are radially far from the center of the contact. On the other hand, the second pattern is mostly a consequence of the weak interactions of the atoms that are radially close to, but vertically far from the center of the contact: these are the atoms of the second atomic layer of the spherical caps. In order to remove the atoms occurring with the second pattern, and which can be considered as false positives, an empirical interacting pressure threshold value of $P_{\mathrm{i}} = 0.02$ GPa was determined by examining all of the studied systems and identifying the pressure values associated with false positives. This threshold removed false positives and had negligible effect on the pressure tail (see Figure 4.3 (a)). After filtering the data using the proposed threshold, the data was smoothened using a moving average filter with a span of 1% of the data points. Finally, the fitting procedure was performed for pressures equal to or greater than the mean pressure of each system. These steps are illustrated in Figure 4.3.

4.4.1.2 The contact distance

The Hertz theory was used to define a contact distance by applying a contact pressure P_{c}: the atoms with interfacial stresses lower than P_{c} were assigned to be out of contact. This contact pressure was defined by comparing the smoothened pressure distribution of a given simulated system with its corresponding fit, prior to the onset of plastic deformation. The pressure at the fitted contact radius was selected as P_{c}, and the contacting atoms were

identified by filtering using the corresponding P_c. These atoms were used for defining the contact distance in a two-step procedure. First, the distances between the contacting atoms and the atoms of the substrate were calculated, and, for each atom, the minimum of the distances was selected as its contact distance. Then, the maximum of the contact distances was defined as the contact distance of the system, d_c.

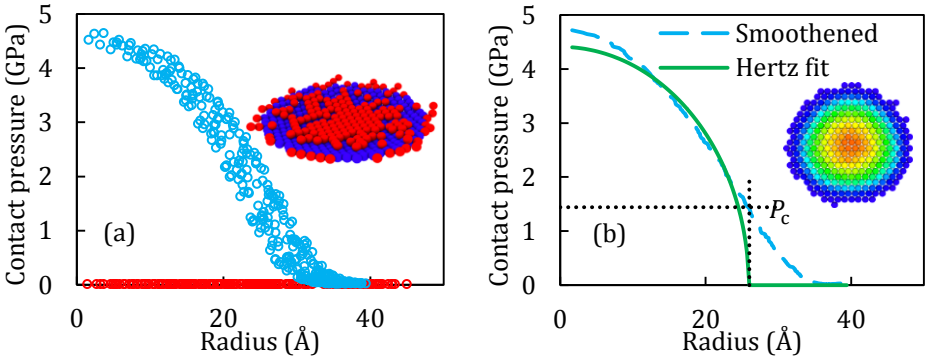

Figure 4.3 The interfacial pressure distribution at the contact as a function of radial distance from the center of the contact was obtained from the atoms of the spherical caps. This figure corresponds to $R = 100$ Å, at a strain prior to the onset of plastic deformation. (a) The atoms of the cap with a non-zero interfacial stress were selected; the red colored data points were identified as false positives, and were removed by applying an empirical interacting pressure threshold value of $P_i = 0.02$ GPa. (b) The Hertz theory was fitted to the smoothened interfacial pressure distribution. The interacting atoms are also shown, colored corresponding to their interfacial pressure values. The fitted contact radius was used to define a contact pressure, as illustrated; this P_c was later used to define the contact distance, as discussed in section 4.4.1.2.

The obtained values of P_c and d_c are summarized in Figure 4.4. As the results show, the values of these two parameters vary with the indenter size: the smaller the radius of curvature, the larger the value of P_c, while an inverse behavior can be noticed for the values of d_c. The same behavior has reported by Yang et al. [12] for a system simulated by a multiscale molecular dynamics approach.

By fitting a power law to the obtained contact distances, one can estimate the values of d_c from

$$d_c \cong 4R^{0.05}. \tag{4.10}$$

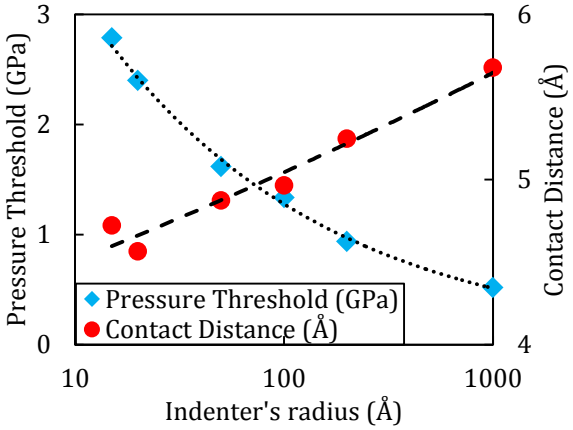

Figure 4.4 The dependence of the pressure threshold and the contact distance on the indenter's radius. The dotted curve and dashed line illustrate the trends.

4.4.1.3 The mechanical behavior

For the simulated material, the values of E and ν are reported to be 26 GPa and 0.3, respectively [91]. Therefore, the reduced Young's modulus was calculated to be $E^* = E/(1-\nu^2) = 28.57$ GPa. In order to compare the results with the Hertz theory, the value of the variable E^* was estimated based on the pressure distributions at the contacts.

Through the fitting procedure, the contact area and the maximum pressure values were estimated for the Hertz contact. Using the formulae for r_c (4.1) and p_0 (4.2), one can conclude that

$$E^* = \frac{\pi}{2} p_0 \frac{R}{r_c}. \tag{4.11}$$

The values of E^* for each system were estimated at different values of indenters' displacement. In order to convert the indenters' displacement into the indentation depth, the following procedure was followed for all systems. Each system was analyzed at various time steps t, and, using the fitted values of p_0 and r_c at each time step, the values of the reduced modulus E_t^* (using (4.11)), the force $F_t = 4/3\, E_t^* R^{-1} r_c^3$ and the interference $d_t = r_c^2/R$ were calculated, where the subscript t specifies the corresponding time step. Then, the absolute error between the fitted values of force and the simulation results were calculated via $\varepsilon = \left|1 - F_{t,\text{fit}}/F_{t,\text{simulation}}\right|$. The time step at which the

absolute error value reached its minimum was selected as the reference point for the conversion of displacement into indentation depth: it was assumed that the actual indentation depth was the value of $d_{t,\mathrm{fit}}$ at the reference point. Hence, a shift was defined as $\delta_d = d_{t,\mathrm{simulation}} - d_{t,\mathrm{fit}}$, and all displacement values were shifted using δ_d. In order to make sure that the force was zero at zero indentation depth, a force shift was similarly defined as $\delta_F = F(id = 0)$, where id is the newly estimated indentation depth. Therefore, the origins of the force-displacement curves were shifted by the corresponding values of (δ_d, δ_F) in order to estimate the force-indentation depth curves. These corrective displacement shifts are summarized in Figure 4.5.

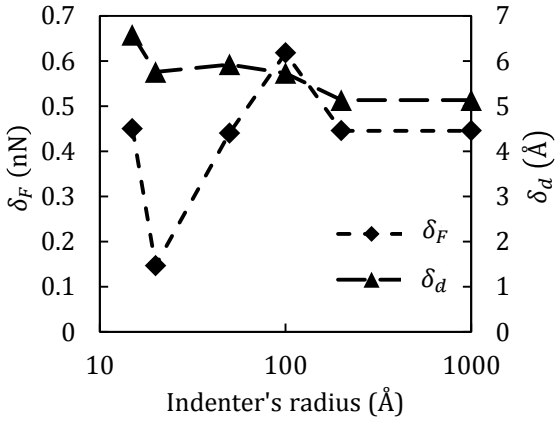

Figure 4.5 The corrective displacement shifts (δ_d, δ_F) as functions of indenter radius, which were used for the conversion of the force-displacement curves into force–indentation depth ones.

Figure 4.6 (a) shows the fitted Young's moduli: the fitted E^* values reveal that this parameter is highly strain-dependent at the very early stages of contact, in contrast to the conventional definition of E^* as a constant value. The results show that the contact behaved as "softer" at shallow indentation depths, and the contact's elastic modulus increased toward the bulk value of 28.57 GPa as the contact approached the point of initiation of plastic deformation. Moreover, it can be seen that the radii of curvature at the contact influenced the fitted E^* values; a normalized representation would give a better insight to this effect. Figure 4.6 (b) shows the fitted E^* values as functions of the normalized indentation depth (d) by the corresponding tip's radius (R), i.e. d/R. Figure 4.6 (a) reveals that the two smallest contact radii, namely 15 Å and 20 Å, behaved differently from the other systems.

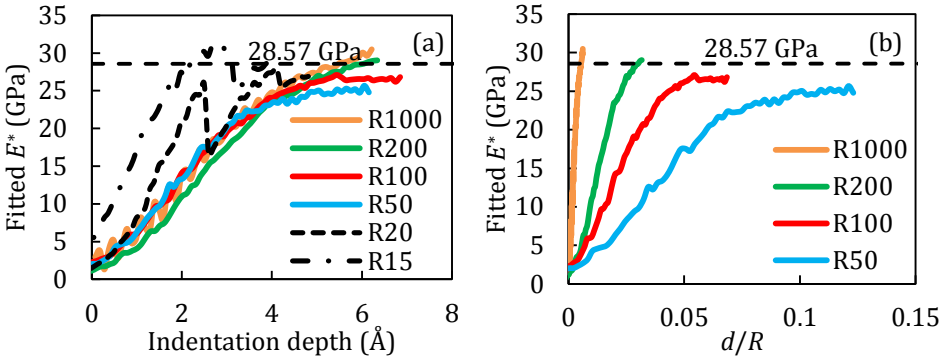

Figure 4.6 Variation of the fitted values of E^* as a function of (a) the indentation depth, and (b) the normalized indentation depth by the corresponding values of the tip's radius. Note that i in Ri indicates the size of contact radius, e.g. $\mathrm{R50} \equiv (R = 50\ \text{Å})$.

In order to explore these behavior further, the number of interacting atoms (N_i), detected based on the pressure threshold of 0.02 GPa (see Figure 4.3), were investigated. Figure 4.7 shows the values of N_i, normalized with the contacts' radii, as a function of indentation depth. This figure shows that the number of the interacting atoms was increasing as the indentation depth was increased. For the smallest contact radius, i.e. $R = 15$ Å, these increments occurred in large steps. These steps became smaller as the indenters were enlarged, resulting in a linear behavior for $R \geq 50$ Å. On the other hand, some fluctuations are visible for the largest system, i.e. $R = 1000$ Å, as is also reflected in Figure 4.6 (a). It should be noted that this behavior could also have occurred due to the system's size and the sampling time: as the systems became larger, their stability was increased, while the sampling time remained the same. Consequently, the extracted data for the smaller systems were essentially an average of all the fluctuating values, while for the largest one, the extracted data needed to be smoothened to filter out the fluctuations. At the same time, it should be noted that a smaller sampling time would potentially reveal fluctuations in the other systems as well.

Although Figure 4.6 (b) shows that the values of the fitted E^* are not exactly a linear function of d/R, assuming a linear relation for shallow indentations helps us to predict the values of E^*. The slope of the fitted E^* values versus d/R, as shown in Figure 4.6 (b), was calculated for the ranges of data with the fitted $E^* \leq 25$ GPa of each system, which corresponds to the indentation depth of ~4 Å, as shown in Figure 4.8. This behavior describes E^*

as a function of indentation depth and the indenter's radius in the form of

$$E_c^* = C + md/R, \tag{4.12}$$

where C is a constant found to be ~2.1 GPa, and m is a power law function in the form of $m = AR^B$; for the current system, it was found that $m \cong 3.7R^{1.05}$ GPa. This empirical formula describes the parameter E^* as a function of the contact geometry, i.e. the indenter's size and the indentation depth, as well as the mechanical properties of the contacting materials.

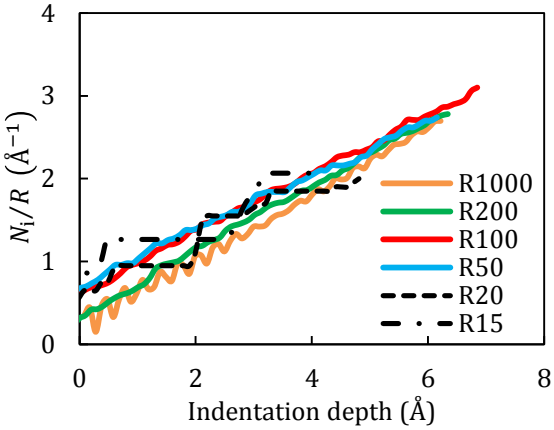

Figure 4.7 The number of interacting atoms (N_i), based on the pressure threshold of 0.02 GPa, normalized by the contact's radius, i.e. N_i/R, increases with increasing indentation depth.

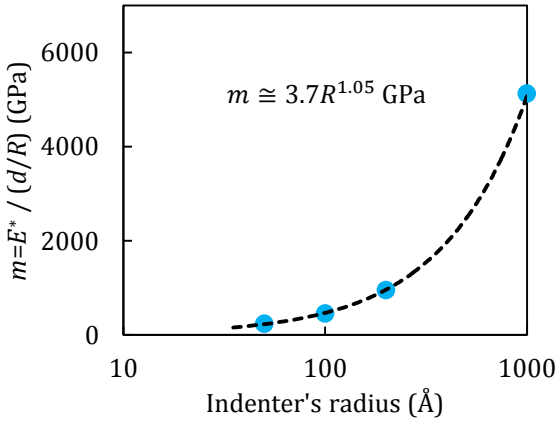

Figure 4.8 The rate of change of the fitted E^* values as a function of the tip's radius.

The value of E_c^* increases and tends to the bulk value by increasing the indentation depth up to a finite value, which is ~4 Å in the current study; however, the way E_c^* varies as a function of the indenter's size depends on the value of the exponent B. While the contact geometry appears directly in the formula for E_c^*, the mechanical properties of the contacting materials are embedded in the values of constants A, B, and C. The nonzero value of C, which suggests a finite value of E^* at the limiting case of zero indentation depth, is a consequence of defining an interacting pressure threshold $P_i = 0.02$ GPa for identifying the interacting atoms, and fitting the Hertz formula to the pressure distribution of those atoms. In order to show this effect, let us assume a limiting case of two interacting atoms: for this conceptual system, the Young's modulus can be defined as $E = \sigma_{eng}/\varepsilon_{eng}$, where σ_{eng} and ε_{eng} are the engineering stress and engineering strain, respectively, and which can be rewritten as $\sigma_{eng} = F_\perp/A_a$ and $\varepsilon_{eng} = \delta_r/r_i$, where r_i is the interacting distance between the two atoms, and δ_r is an infinitesimal change in r_i. The Young's modulus can be rewritten as $E = \frac{F_\perp/A_a}{\delta_r/r_i} \sim \frac{r_i}{A_a} \cdot \frac{dF_\perp}{dr} = 168\varepsilon\sigma^6 r_i^{-7} A_a^{-1}$; therefore, the Young's modulus would have a nonzero value at any interacting distance r_i. In the current study, the interacting distance was defined by an interacting pressure threshold, and by replacing σ_{eng} with P_i, a corresponding contact force can be estimated as $F_i = P_i A_a$. Then, the interacting force can be calculated as $F(r) = 48\varepsilon\sigma^{12}/r^{13}$, which results in $r_i = 6.417$ Å, for $F(r) = F_i$ (see section 4.4.1.4 for the calculation of A_a). Therefore, the corresponding value of the Young's modulus can be estimated to be $E \cong 2.27$ GPa. Although this crude estimation of the Young's modulus, which is close to the value of $E_c^*(d = 0) = C = 2.1$ GPa, cannot be directly translated into the contact's elastic modulus, it appears to justify the nonzero value of the constant C.

The Hertz formula was solved using the fitted values of E^*, the bulk value of $E^* = 28.57$ GPa, and the estimated values from (4.12), as shown in Figure 4.9. As the results show, the fitted values of E^* describe best the systems' behavior through the whole indentation process, as was expected, while the values estimated with (4.12) are valid only for very shallow indentation depths. On the other hand, the bulk value of $E^* = 28.57$ GPa appears to fit better to the results for indentation depths larger than ~4 Å. Therefore, as the results show, assuming the applicability of the Hertz theory at the atomic scale, a redefined value of E^* is needed to describe contacts at shallow indentation depths.

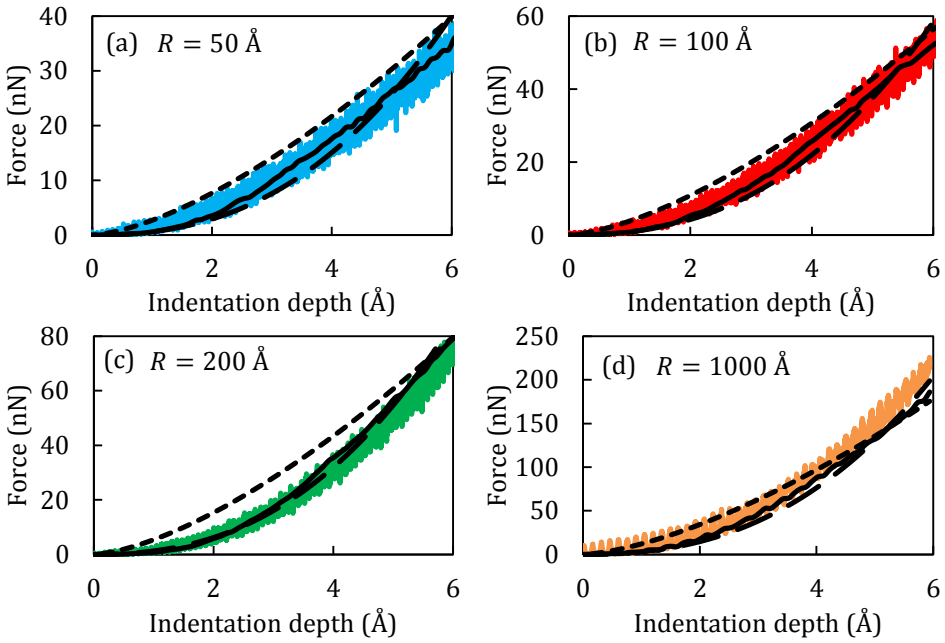

Figure 4.9 The force–indentation depth curves from simulations were compared to the Hertz theory using the fitted values of E^* based on (4.11) (continuous line), the estimated ones from (4.12) (large dashed line), and the constant bulk value of $E^* = 28.57$ GPa (small dashed line) for the spherical caps with radii of (a) 50 Å, (b) 100 Å, (c) 200 Å, and (d) 1000 Å. Note that the axes ranges are different.

4.4.1.4 The contact area

In this section, the correctness of the proposed pressure cutoffs was investigated by comparing the Hertz solution with the estimated contact areas based on the contact distances. Hertzian mechanics suggest a relation between the radius of the contact area r_c, the indenter's radius, and the indentation depth in the form of $d = r_c^2/R$. The radii of the contact areas for each of the simulated systems were estimated as follows: first, the contacting atoms were identified. Then, the real contact area was estimated via $A_{\text{real}} = N_{ca}A_a$, where N_{ca} is the number of the contacting atoms, and A_a is the projected area of an individual atom, estimated from $A_a = \pi/4\, d_a^2$, where d_a is the atomic diameter, which was found to be 3.94 Å, following the method described in Chapter 3. Finally, assuming the contact area to be a circle, the radius of the

contact was calculated. Figure 4.10 shows the radii of contact normalized by the indenters' radii versus the indentation depth.

The results show that the estimated contact areas based on the contact distances were in good agreement with the Hertz solution, which verifies the proposed contact distance definitions, as well as the method used for the conversion of the indenters' displacement into indentation depth.

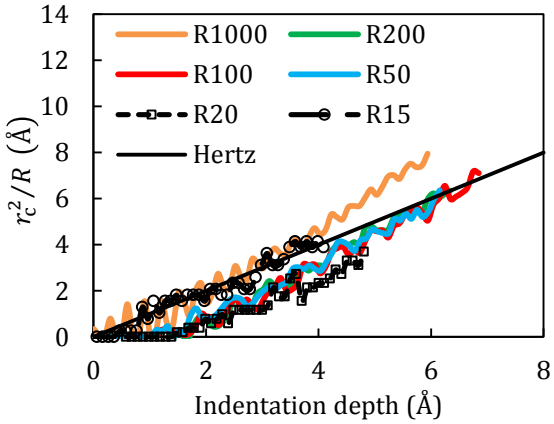

Figure 4.10 The normalized contact area as a function of indentation depth. The overestimation of R1000 at large indentation depths could be due to the comparison between A_{real} (MD simulations) and A_{pc} (Hertz solution).

4.4.1.5 Contacting atoms versus interacting atoms

The agreement between the estimated contact area and the Hertz solution implies that there is a distinction between the interacting area and the contacting area, where the former can be calculated from the interfacial pressures, and the latter can be estimated based on the defined contact distances; however, one may wonder if these two areas result in the same contact behavior. This issue can be investigated by comparing the number of interacting atoms (N_{i}) and the number of contacting atoms (N_{ca}). Figure 4.11 shows that the ratio of N_{ca}/N_{i} is very small at the beginning of the contact; however, with increasing indentation depth, N_{ca} and N_{i} changed with different rates in a way that the ratio of N_{ca}/N_{i} tended to 1.

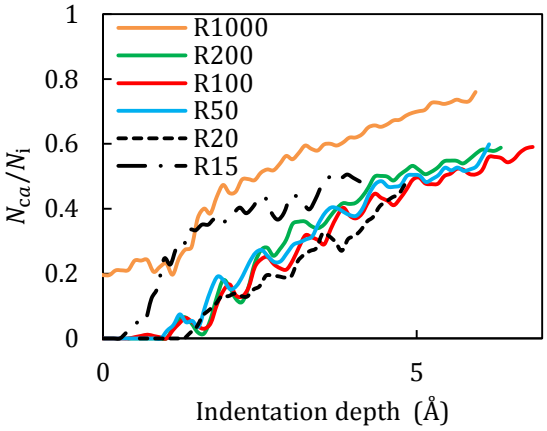

Figure 4.11 The number of interacting atoms (N_i) and the number of contacting atoms (N_{ca}) change with different rates as the indentation depth increases. It should be noted that the results were smoothened with a moving average filter with a span of 5% of the data points, in order to remove the fluctuations due to the sampling sizes, as is discussed in 4.4.1.3.

Aside from the essentially different behavior of the contact with $R = 15$ Å, the results show a clear size effect: *the contact area tends to the interacting area with increasing indenter size*. This effect can be related to the atoms responsible for the tail appearing in the pressure distribution, as described in section 4.4.1.1: practically, the contact area tends to the interacting area with increasing indenter size as the pressure tail length becomes negligibly small and the pressure distribution increasingly approximates the Hertzian one. More specifically, as the interacting area increases, the contact area increases faster than does the length of the pressure tail. In order to demonstrate this, the systems were analyzed at a displacement of ~4 Å: the lengths of the pressure tails were estimated via an empirical formula as a function of the indenter radius, as is shown in Figure 4.12 (a), which shows that the ratio ρ/r_c decreases as the indenter's size increases. Furthermore, the ratio A_c/A_i can be predicted by $(r_c/(r_c+\rho))^2$, where $r_c = \sqrt{Rd}$, with $d = 4$ Å, and $\rho = \rho_1 \ln(R) + \rho_2$ is the length of the pressure tail, and ρ_1 and ρ_2 are the fitted constants. Figure 4.12 (b) shows the comparison between the predicted ratios of A_c/A_i and the simulation results.

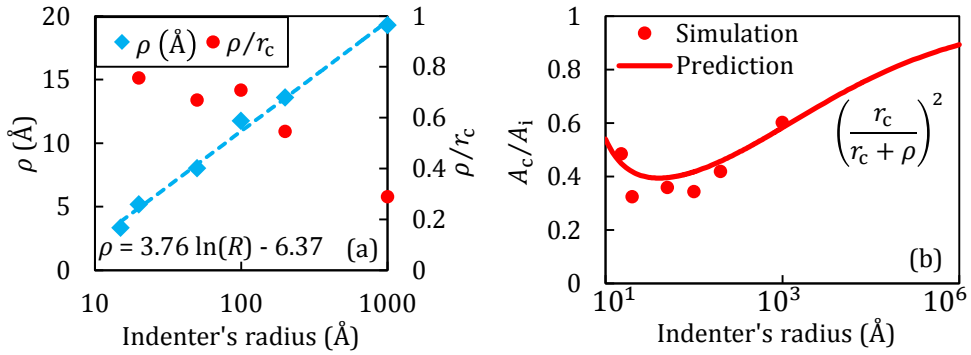

Figure 4.12 (a) The length of the pressure tail, ρ, was calculated at a displacement of ~ 4 Å, and described by a natural logarithmic function of the indenter's radius. Moreover, the figure shows the ratio ρ/r_c decreases with increasing indenter size. (b) The ratio of A_c/A_i of, both, the simulation results and the prediction method are shown. The prediction is based on the Hertz contact theory, i.e. $r_c = \sqrt{Rd}$, and the values of ρ calculated in (a).

4.4.2 Rough surface contacts

In order to estimate the projected contact area of the rough surface contacts, different approaches were applied, which are summarized in Table 4.2. In "projection method", the mean value of the radius of curvature R for the rough surface was estimated; the mean value of the radius of curvature for the constructed surface was estimated through its definition of $\boldsymbol{R} = \left|\left(1 + \boldsymbol{z}'^2\right)^{3/2}/\boldsymbol{z}''\right|$, where $\boldsymbol{z}'$ and $\boldsymbol{z}''$ are the first and second derivative of the surface heights, respectively; then, R was defined as $\sqrt{R_x \cdot R_y}$. Using the calculated R and (4.10), a contact distance was defined in order to identify the contacting atoms. Then, the projected area of the contacting atoms on a plane normal to the applied force, i.e. the xy plane in the current study, was estimated as the projected contact area A_{pc}. The relative contact area was easily calculated from the ratio $A_{rpc} = A_{pc}/A_0$. In another approach, the GW model was used for estimating the contact behavior of the rough contacts. To do so, (4.4) and (4.5) were solved, and the results were normalized with the nominal contact area A_0, in order to achieve the relative projection contact area A_{rpc} and the nominal pressure, respectively. The value of R was estimated as mentioned above. Moreover, the local maxima were detected and identified as asperities; therefore, the probability distribution function of the

asperities could be generated, which was needed for solving the GW model. Finally, for the randomly rough surface, the Persson model, i.e. (4.6), was used. The value of the parameter G was found from, both, (4.7) and (4.8). It should be noted that in order to work with (4.7), the PSD of the rough surface was needed, which was estimated via with the algorithm described by Persson et al. [96].

The contact behavior of the systems were analyzed using the methods that are summarized in Table 4.2, and the results are presented and discussed in the following sections.

Table 4.2 The steps of the methods used for estimating the values of the relative projected contact area.

Projection method	1-	Identification of the contacting atoms through the definition of contact distance
	2-	Visualization of the contacting atoms
	3-	Analysis of the projection of the contacting atoms on a lateral (xy) plane
GW	1-	Detection of the local maxima, and construction of PDF of the identified asperities
	2-	Solving (4.4) and (4.5)
Persson I	1-	Calculation of the PSD of the rough surface
	2-	Integration of PSD in the form of (4.7)
	3-	Solving (4.6)
Persson II	1-	Calculation of the probability distribution of the interfacial pressure values
	2-	Fitting of the double Gaussian function in the form of (4.8) to the interfacial pressure distribution of the system
	3-	Solving (4.6)

4.4.2.1 Multi-asperity rough contact: GW approximation

The generated multi-asperity rough surface, with the estimated probability distribution function (PDF) shown in Figure 4.13.

The mean value of the radius of curvature for the constructed surface was estimated to be ~111 Å, which is slightly larger than the assigned value of 100 Å for the generation of the surface. It should be noted that the estimated value of $R = 111$ Å was used for working with the GW model.

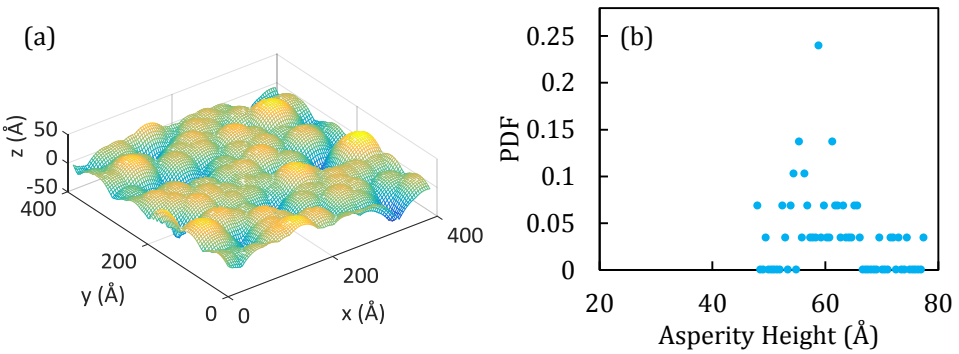

Figure 4.13 (a) The generated GW surface with $\sigma = 10$ Å, $R = 100$ Å, and $\eta \cong 5 \times 10^{-4}$ Å^{-2}, and (b) its PDF of asperity heights with 61 detected asperities.

In order to analyze the results, first, the mean plane separation was estimated using the height of the simulation box, the initial thickness of the deformable body, and the asperity mean height of the rough substrate, as demonstrated in Figure 4.14. The atomistic system was analyzed by identifying the contacting atoms by applying a contact distance of $d_c = 5.062$ Å. Using the projection method (see Table 4.2) the projected area of the contacting atoms was estimated as the projected contact area A_{pc}. Table 4.3 shows the projection of the contacting atoms under increasing contact force. The relative projected contact area ratio A_{rpc}, and the mechanical response of the contact is shown in Figure 4.15.

In order to estimate the contact force using the GW model, the reduced Young's modulus of $E^* = 28.57$ GPa was used; the reason was the initiation of local plastic deformations, suggesting that the indentation depth for each individual spherical contact was large enough for the bulk value of E^* to have been reached. The results are shown in Figure 4.16.

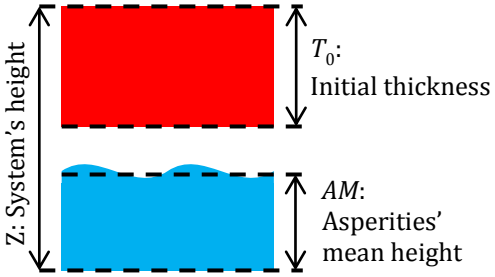

Figure 4.14 The schematic of the GW contact simulations. The separation was defined as $s = Z - (AM + T_0)$.

Table 4.3 The black dots represent the projection of the contacted atoms of the GW surface. The first row indicates the contact force in units of nN.

$1.49e-5$	18.15	91.15
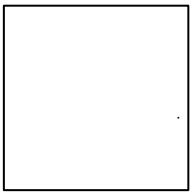	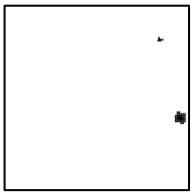	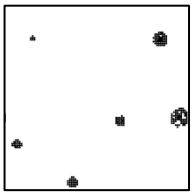
228.18	582.30	814.50
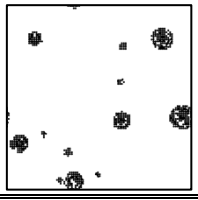	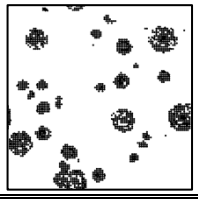	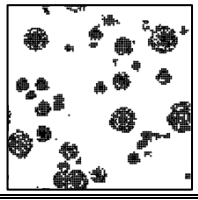

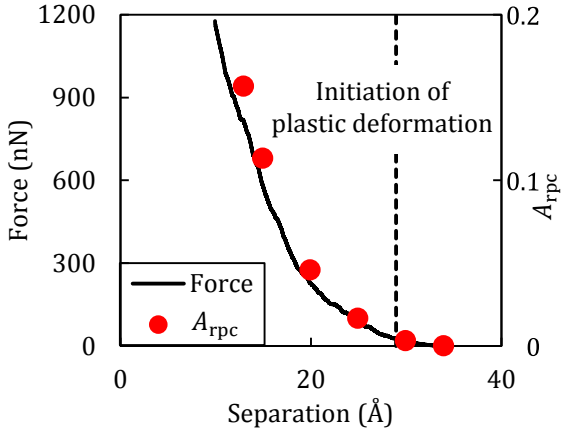

Figure 4.15 The simulation results of the GW contact. The continuous line shows the external contact force, while the dots show the value of A_{rpc} at different values of separation.

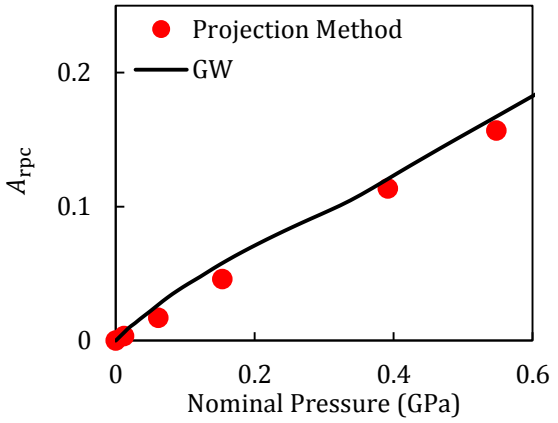

Figure 4.16 The relative projected contact area as a function of nominal pressure for the GW type multi-asperity rough surface.

4.4.2.2 Randomly rough contact

The GW-type surface was analyzed, and its lateral correlation length was found to be ~23.4 Å. Using this value and $\sigma = 10$ Å, a comparable randomly rough surface with a normal distribution of heights was generated, as shown in Figure 4.17.

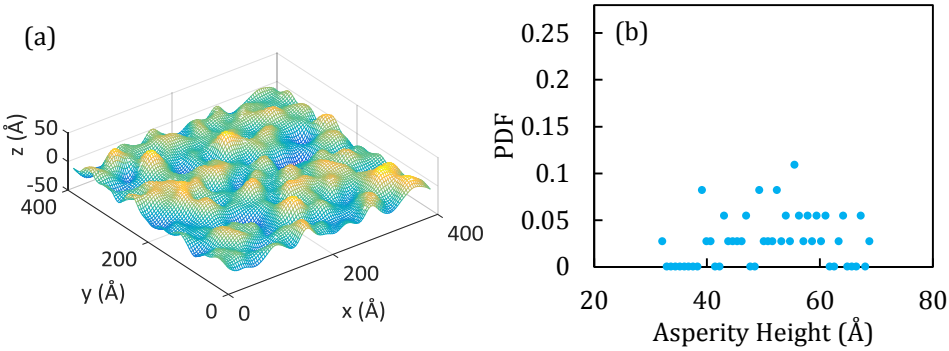

Figure 4.17 (a) The generated randomly rough surface with a correlation length of 23.4 Å, and $\sigma = 10$ Å, and (b) its PDF of asperity heights with 48 detected asperities.

The projected contact area at different pressure values was estimated via all four mentioned approaches in Table 4.2. In order to estimate the contact area via the projection method, the mean radius of curvature of the rough surface needed to be calculated. This value was found to be 112 Å, which was almost equal to $R \cong 111$ Å of the simulated multi-asperity surface. Using (4.10), a contact distance of 5.064 Å was defined for identifying the contacting atoms. Table 4.4 shows the projection of the contacted atoms at different separations.

The GW model was applied to the surface in the same way that was done for the GW-type rough surface (see section 4.4.2.1). In order to estimate the contact behavior using the Persson theory, first, the value of G was calculated based on (4.7). The needed PSD for estimating the parameter G from (4.7), was calculated following the algorithm described by Persson et al. [96] (see Figure 4.18), and the value of G was calculated to be 74.57 GPa^2, with $E^* = 28.57$ GPa, and $Mq_L = q_S$ at a length scale of $\lambda = a_0\sqrt{2} \cong 7.90$ Å.

Furthermore, the Persson model was used with the value of $\bar{G}$ as the fitting parameter of (4.8). To do so, the interfacial pressure distributions were calculated at different nominal pressure values from the simulation results. Then, the pressure distributions were smoothened using a moving average filter with a span of 1% of the data points. Finally, (4.8) was fitted to the pressure distribution, and $\bar{G}$ was found. Figure 4.19 shows the interfacial pressure distribution of the contact at a nominal pressure of $P_0 = 0.39$ GPa. It should be noted that the difference between the simulation results and (4.8) for small pressure values is due to the long-range interactions that may not be

negligible in the atomistic simulations, but are absent in non-adhesive contact theories [12].

Table 4.4 The black dots represent the projection of the contacted atoms of the randomly rough surface. The first row indicates the contact force in units of nN.

4.64e − 4	12.18	53.36
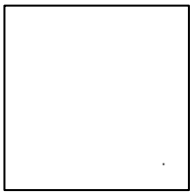	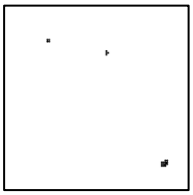	
165.33	446.96	575.32
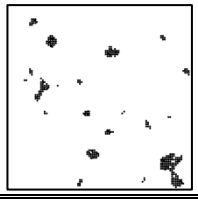	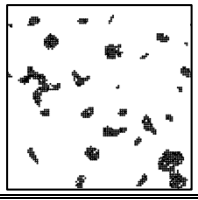	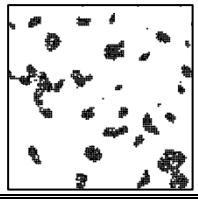

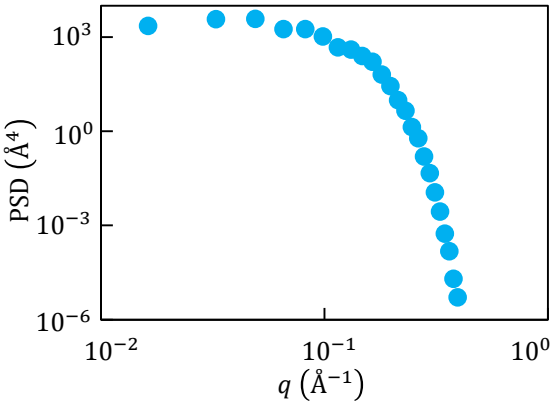

Figure 4.18 The calculated PSD of the randomly rough surface.

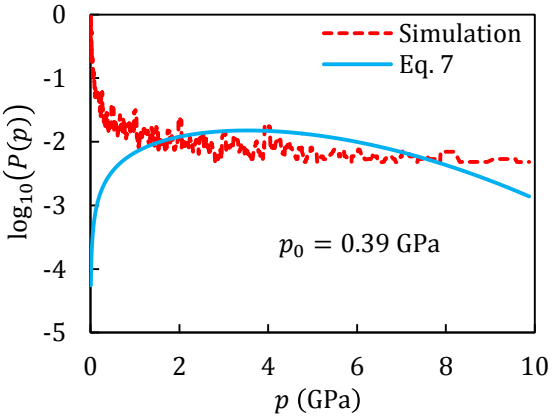

Figure 4.19 The interfacial pressure distribution $P(p)$ at the nominal pressure of $p_0 = 0.39$ GPa.

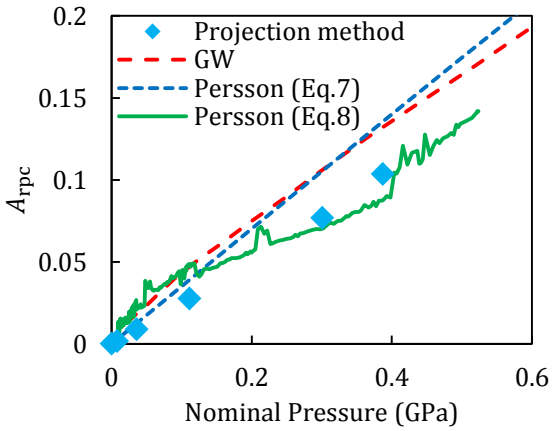

Figure 4.20 The relative projected contact area as a function of nominal pressure for the randomly rough surface.

Figure 4.20 compares the contact behavior of the randomly rough surface, estimated using all approaches of Table 4.2. As the results show, for light squeezing pressures, the estimations of, both, the Greenwood-Williamson and Persson theories are larger than the results from the projection of the contacting atoms. Moreover, it can be noticed that if the parameter G is found using (4.8), the Persson model overestimates the contact area at very small

pressures, and then tends toward the results of the projection method. The reason is that the pressure distribution contains all the interacting atoms, and not only the contacting ones, which affects the fitted values of $\bar{G}$; however, with increasing the indentation depth, the number of the contacting atoms tend toward the number of the interacting ones, as was discussed in section 4.4.1.5. Therefore, as the nominal pressure increases, the contribution of the contacting atoms will be larger in the pressure distribution, which will be directly reflected in the fitted values of $\bar{G}$, and consequently, the description of the Persson model would be closer to the results of the projection method.

4.4.2.2.1 Effects of the length scale on the estimation of the contact behavior

The value of G can be defined as $G = 1/8\, E^{*2}\langle|\nabla h|^2\rangle$ (see section 4.2.3). Assuming $G/\bar{G} = 1$, with $\bar{G}$ being the fitting parameter of (4.8), the values of the contact modulus can be estimated via $E^* = \sqrt{8\bar{G}/\langle|\nabla h|^2\rangle}$; therefore, the length scale that is used in the calculation of the mean square gradient of the rough surface can affect the estimated value of E^*. Figure 4.21 (a) shows the values of $\langle|\nabla h|^2\rangle$ calculated at different length scales, while the corresponding fitted values of E^* at two different length scales are shown in Figure 4.21 (b).

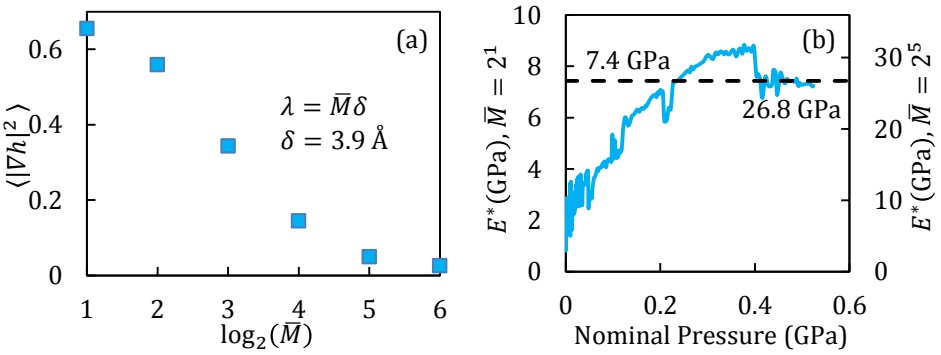

Figure 4.21 (a) The effect of the length scale on the mean square gradient of the rough surface. The length scale is defined as $\lambda = \bar{M}\delta$, where $\delta = 3.9$ Å is the lateral distance between two neighboring atoms of the rough surface. Note that $\bar{M} \neq M$. (b) The dependence of the fitted values of E^* to the nominal pressures using two different length scales (on the left and right vertical axes).

Considering the calculation method of $\bar{G}$, which is performed at the lowest length scale of the system, a reasonable length scale for the calculation of the mean square gradient would be $\lambda = 2\delta$; however, this would result in low values of E^*, as is shown in Figure 4.21 (b).

The values of G can be calculated at different length scales by assuming that the reduced modulus is $E^* = 28.57$ GPa. It was found that $G(\lambda = 2^6\delta) = 74.28$ GPa^2 had the closest correspondence to $G = 74.57$ GPa^2, which was calculated based on the PSD of the surface with $q_S = 2\pi/2\delta$. This inconsistency between the length scales could be a consequence of converting the definition of G from the original form of (4.7) into $G = 1/8\, E^{*2}\langle|\nabla h|^2\rangle$ using the second moment of the PSD, as described in section 4.2.3. Considering the results that are presented in Figure 4.20, calculating the theoretical value of G in the form of (4.7) appears to resolve this issue.

4.4.3 Comparison between studied rough surfaces and their contacts

In order to compare the surfaces, a number of statistical data was calculated for both surfaces, and the results are summarized in Table 4.5. Note that all calculations were performed at a length scale of $\lambda = 2\delta \cong 7.8$ Å.

Table 4.5 The statistical calculated values for the studied rough surfaces.

	σ (Å)	$\langle\|\nabla h\|^2\rangle$	Skewness	Kurtosis
GW type	9.82	0.58	−0.64	4.05
Randomly Rough	9.67	0.65	−0.05	3.05

For light squeezing pressures, the rough surface analytical models predict that the contact area increases linearly with the nominal pressure in the form of $A_{\mathrm{rpc}} = \kappa\left(P_0/\left(E^*\sqrt{\langle|\nabla h|^2\rangle}\right)\right)$ [97]. The simulated systems showed the same behavior as well (see Figure 4.22), resulting in a proportionality coefficient of ~6.2, which is larger than the corresponding value of, both, the multi-asperity models, i.e. $\sqrt{2\pi}$, and the Persson theory, i.e. $\sqrt{8/\pi}$ [97]. This could be a result of the lateral resolution for the calculation of the mean square gradient of the rough surfaces, as is demonstrated and discussed in section 4.4.2.2.1.

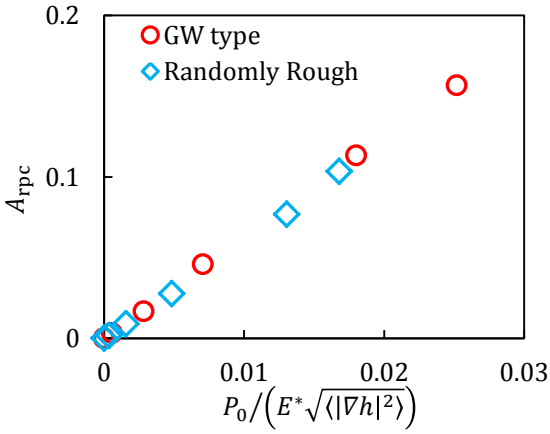

Figure 4.22 The relative projected contact area as a function of normalized pressure for both of the simulated systems with rough surface contacts.

4.5 Summary and conclusions

In this chapter, a number of continuum models for non–adhesive contacts were investigated at the atomic scale and it was revealed that the atomistic behavior is rather different from the continuum descriptions, especially at the very first stages of the contact.

First, the Hertz contact model predictions were compared to the simulated force-displacement curves; however, large discrepancies between the two were found. Therefore, the pressure distributions were analyzed instead, in order to calculate the reduced Young's moduli. It was found that the values of E^* were increasing in the form of $E_c^* = C + AR^{B-1}d$ for shallow indentation depths, of up to ~4 Å in the current study, before they reached a constant value. Contacts with various indenter sizes showed the same trend, except for the contacts with the indenter radii of 15 Å and 20 Å: these two contacts were different due to their stepped-like increment in the number of interacting atoms. Moreover, it was shown that the contact distance is a function of the indenter's radius, in the form of $d_c \cong 4R^{0.05}$. It should be noted that the results may be different for different systems: in other words, the results could be affected by changing the material, temperature, crystallographic orientation, applied potential energies, and indentation velocity.

Furthermore, the contact behavior of two different types of rough surfaces, a multi-asperity GW-type rough surface and a comparable random one, were

investigated. The contact behavior of both systems were found to be very close. Moreover, the results of the present study show that the relative projected contact area is a linear function of nominal pressure, even after plastic deformation is initiated locally.

The multi-asperity rough surface was studied by the GW theory, and it was found that using the elastic contact modulus of $E^* = 28.57$ GPa, the theory correctly estimates the contact area of the simulated system. Furthermore, both, the GW and Persson theories were used for studying the contact behavior of the randomly rough surface. The results show that the estimation of the contact area in the Persson theory is highly dependent on the method used to calculate the parameter G: the theory would correctly describe the contact behavior if G were calculated using its theoretical solution (4.7), or as the fitting parameter of (4.8); however, the relation $G = 1/8\, {E^*}^2 \langle |\nabla h|^2 \rangle$ results in some inconsistency of the length scale, which would be problematic, at least for studying atomistic systems.

This page is intentionally left blank.

Chapter 5 *

Surface roughness of gold substrates at the nanoscale: an atomistic simulation study

The statistical properties of rough surfaces at the nanoscale are studied using classical molecular dynamics. Atomistic fcc blocks of gold are generated with different crystal orientations, and with rough surfaces having the same root-mean-square roughness with variable power spectral density (PSD) exponents and roll-off wavenumbers. The process of rough surface generation may result in thermodynamically unstable sharp spatial features. In order to relax the structure, the blocks are equilibrated at 300 K. It is found that all surfaces experience changes in their roughness, regardless of their crystal orientation or temperature, although the changes are only temperature-independent when $T \leq 0.4T_{\mathrm{m}}$. Based on the analyzed PSDs of the equilibrated substrates, two methods for generating pseudo-stable rough surfaces are introduced and discussed.

5.1 Introduction

As a consequence of the miniaturization of mechanical devices, a large number of tribological research studies have been directed toward the atomic scale. Researchers routinely utilize atomistic computer simulation methods, e.g. classical molecular dynamics (MD), in order to investigate different tribological processes, such as normal or frictional contacts. In these works, the substrate is usually represented, either, as a flat or a simple patterned surface. One can also find a limited number of tribological MD studies which employed randomly rough substrates [8, 66, 70, 78-81, 98-102]; however, due to limitations in the lateral resolution of measuring devices, the nature of the atomic-scale roughness present on real surfaces is still under question. An

* This chapter has been originally published in Tribology International **115** (2017) 165-178.

important result stems from the work of Oliver et al. [47] who studied the morphology of tungsten nanoparticles using field-ion microscopy, and showed they have a stepped geometry; this was later used for studying atomistic contacts [65], and also, for identifying the surface atoms via their potential energies [103]. On the other hand, the properties required to accurately generate a realistic rough surface at the atomic scale have yet to be investigated thoroughly.

In this chapter, various randomly rough surfaces were generated and used for building atomic blocks of pure gold. Then, the blocks were equilibrated via classical MD simulations, and the effects of different parameters, such as temperature and crystal orientation, on the equilibrated blocks were studied. The results show that the atomistic substrates cannot retain their sharp steps and edges, and the surfaces are smoothened due to thermodynamics. This has important consequences in the performance of atomistic simulations, where emphasis should be placed on using physically meaningful surface topographies.

5.2 Quasi self-affine rough surfaces

The random nature of surface roughness, which is always present at some length scale, can be described statistically. One of the most widely used descriptions of random surfaces was introduced by Nayak [104]; through the transformation of rough surfaces from the Cartesian space into the Fourier one, Nayak represented the height function $h(\mathbf{p})$ (where $\mathbf{p} = (x, y)$ is a 2D vector in the plane $z = 0$) of homogeneous-isotropic-Gaussian surfaces as

$$h(\mathbf{p}) = \sum_{\mathbf{q}} h(\mathbf{q}) \cos\big(\mathbf{q} \cdot \mathbf{p} + \varphi(\mathbf{q})\big), \tag{5.1}$$

where $\mathbf{q}$ is the wavevector with q_x and q_y as its components, $h(\mathbf{q})$ is the height roughness spectrum and contains the coefficients of the discrete Fourier transform of the rough surface, and $\varphi(\mathbf{q})$ is a phase shift, randomly and uniformly distributed over $[0,2\pi)$. In order to generate real numbers for $h(\mathbf{p})$ using (5.1), the values of $h(\mathbf{q})$ and $\varphi(\mathbf{q})$ should be defined in a way that $h(-\mathbf{q}) = h(\mathbf{q})$ and $\varphi(-\mathbf{q}) = -\varphi(\mathbf{q})$. The coefficients $h(\mathbf{q})$ are related to the power spectral density (PSD) of the surface, $C(\mathbf{q})$, which is the Fourier transform of its autocorrelation function, via $h(\mathbf{q}) = (2\pi/L)|C(\mathbf{q})|^{1/2}$ [96], where L is the length of the system.

5.2.1 The PSD of self-affine surfaces

For the case of isotropy of the surface, $C(\mathbf{q})$ can be averaged to construct $C(q)$, where q is the wavenumber that corresponds to the magnitude of the wavevector $\mathbf{q}$, i.e. $q = \|\mathbf{q}\|$. One of the models for describing the PSD of a self-affine surface, which has been widely used in the field of contact mechanics, has a simple formulation in the form of:

$$C(\mathbf{q}) = \begin{cases} C_0 & q_\mathrm{L} \le \|\mathbf{q}\| < q_\mathrm{r} \\ C_0(\|\mathbf{q}\|/q_\mathrm{r})^{\beta} & q_\mathrm{r} \le \|\mathbf{q}\| \le q_\mathrm{S} \\ 0 & \text{elsewhere} \end{cases} \tag{5.2}$$

where β is referred to as "the PSD exponent" in this text and has a negative value, and C_0 is a constant. Appendices E and F provide detailed discussions on the values of β and C_0. The range of wavenumbers is bounded by the long and short wavelength cutoffs denoted by q_L and q_S, respectively. The lowest possible wavenumber is connected to the length of the system, L, and its value is $q_\mathrm{L} = 2\pi/L$, while the highest possible wavenumber is related to the shortest wavelength, i.e. the shortest distance between two sampled neighboring points, δ, and its value is $q_\mathrm{S} = 2\pi/\delta$. From this definition, it follows that q_S depends on the lateral resolution of measuring instruments. Moreover, q_r is the roll-off wave number, with $q_\mathrm{L} < q_\mathrm{r} < q_\mathrm{S}$. The schematic PSD corresponding to the definition of Eq. 2 is shown in Figure 4.1.

The definition of the PSD in the form of (5.2) is based on the Bhushan and Majumdar discovery of bifractal surfaces through analyzing magnetic tapes using atomic force microscopy [105]. The characterization of bifractal surfaces was discussed by Wu [106]: a bifractal surface has a critical wavenumber q_c in its PSD such that the PSD exponent is different for wavenumbers larger and smaller than q_c. If $q_\mathrm{r} \neq q_\mathrm{L}$, (5.2) results in a bifractal surface with $q_\mathrm{c} = q_\mathrm{r}$. The definition of bifractal surfaces can be more complicated, e.g. see [107, 108]. While most models have different formulae for wavenumbers larger or smaller than q_c, the PSD of isotropic self-affine surfaces can be defined based on the K-correlation function, developed by Palasantzas [109], in the following form [110]:

$$C(q) = \frac{(\zeta\sigma_\mathrm{rms})^2}{2\pi}\left(1 - \frac{\zeta^2}{\beta+2}q^2\right)^{\beta/2}, \tag{5.3}$$

where ζ is the lateral correlation length, which is defined using the autocorrelation function $R(r)$ of the surface: more specifically, ζ is the value of r at which $R(r=\zeta) = \exp(-1)$ [110]. It should be noted that $\beta < -2$ in this

model. Although this model can describe the behavior of bifractal surfaces, it does not require any critical wavenumber.

5.3 Atomic blocks with rough surfaces and the necessity of equilibration

In order to generate an atomic block with a rough surface, the first step is to generate the rough surface as a point cloud of spatial coordinates, which will then be used for cutting an atomic block [99]. In the process of cutting, one may include the data points of the rough surface to preserve its spatial features [99] (see Figure 5.1); however, this would result in an unrealistic structure, with atoms being stacked closer together than possible in a real system. Depending on the resolution of the generated surface, this method can remove sharp atomic steps and provide a smoother surface. In contact mechanics studies, this feature yields results closer to those of continuum mechanics theories, e.g. see [23]; however, because of the artificially high atomic density at the surface, the applicability of this method is limited to non-adhesive contacts, where only repulsion is accounted for. It should be mentioned that, if an atomic block is generated by this method, the block should be treated as completely rigid, otherwise the high surface density will result in instability for the system. Moreover, the lack of knowledge on the nature of roughness at the atomic scale limits researchers to data measured at larger scales: the vertical resolution along the height dimension can be down to the atomic level, but the lateral resolution of most instruments is still of the order of tens of nanometers. On the other hand, it is possible to cut the atomic block without imposing the rough surface data points to the system, resulting in an atomic block that would not have an artificially high atomic density; however, in this latter case, which is the focus of the present work, atomic steps and edges are unavoidable.

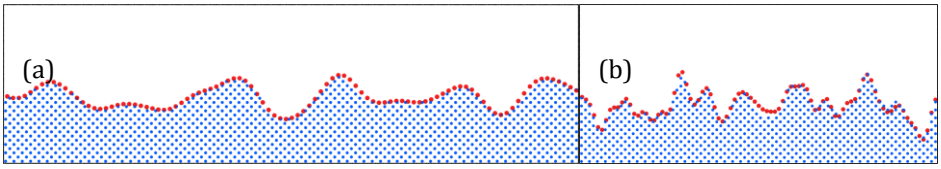

Figure 5.1 Slices of two atomistic blocks generated by different arbitrary rough surfaces with lateral correlation lengths of (a) ~21 Å and (b) ~7 Å. The smaller/blue dots indicate the atoms positioned based on their crystal structure descriptions, and the larger/red dots indicate the data points of the surface.

The sections of two representative atomic blocks with rough surfaces are depicted in Figure 5.1: the prevalence of atomic steps is clearly shown. In the figure, the two rough surfaces were compared through their lateral correlation length, ζ: a larger value of ζ corresponds to smoother features.

When investigating rough surface contact with classical molecular dynamics, the atomic block needs to be relaxed from all arbitrarily assigned initial conditions so that the system can approach an equilibrated new state point [111, 112]. In this study, atomic blocks were sliced with different numerical rough surfaces (without imposing the numerical rough surface as additional atoms; see discussion in earlier paragraph) and the resulting rough atomic blocks were analyzed by examining their statistical properties.

5.4 Simulation procedure

5.4.1 Generating the rough substrates based on the simplified PSD

The randomly rough surface generation was performed with the algorithm described by Persson et al. [96] and Rigazzi [88], by specifying the lattice constant $\delta = \mathrm{a}_0$, where a_0 is the lattice parameter of the simulated material. The surfaces were generated with a lateral length L of $60\mathrm{a}_0$. The highest wavenumber was set to $q_\mathrm{S} = \pi/\mathrm{a}_0$. The roughness of the generated surfaces was varied by changing the values of the roll-off wavenumber and the PSD exponent: the roll-off wavenumber was defined as $q_\mathrm{r}(i) = q_\mathrm{L}^{1-i/4} q_\mathrm{S}^{i/4} = q_\mathrm{L}(L/\delta)^{i/4}$ with $i \in \{1, 2, 3\}$, and different values for the PSD exponent were selected with $\beta \in [-1, -5]$. The corresponding values of C_0 were defined based on (F.3), in order to set the RMS roughness at $2\mathrm{a}_0$ (see Appendix F). It should be noted that $\beta = -2$ resulted in an undefined value of I_0 (see (F.4)) for which the surfaces cannot be generated; therefore, β was approximated by setting its value to -2.001.

Table 5.1 summarizes all the simulated rough surfaces: the surfaces are designated via their roll-off wavenumber and PSD exponent values, e.g. $q1$ denotes surfaces with $q_\mathrm{r}(i = 1)$, and $\beta 3$ refers to surfaces whose initial PSD exponent was -3; along these lines, $q1\_\beta 3$ points to the surface with$q_\mathrm{r}(i = 1)$ and $\beta = -3$.

Each of the generated rough surfaces was used for constructing a rough atomic block. To do so, a thick block of gold with a lattice parameter of $\mathrm{a}_0 = 4.078$ Å [91] was constructed. Then, the cutting procedure was applied

by placing the rough surface at a position where the distance from the bottom of the block and the minimum height of the surface was $10a_0$; in other words, each block had a minimum thickness of $10a_0$, which was selected based on the normalized radial distribution function, $g(r)$, of an extra NPT simulation. The details can be found in section S1.

Table 5.1 All the surfaces generated based on the PSD of (5.2). The q_r values, normalized by q_L, for $i = 1$, 2, and 3 would be 2.78, 7.75, and 21.56, respectively.

	$m = -1$	$m \cong -2$	$m = -3$	$m = -4$	$m = -5$
$q_r(i = 1)$	$q1\_m1$	$q1\_m2$	$q1\_m3$	$q1\_m4$	$q1\_m5$
$q_r(i = 2)$	$q2\_m1$	$q2\_m2$	$q2\_m3$	$q2\_m4$	$q2\_m5$
$q_r(i = 3)$	$q3\_m1$	$q3\_m2$	$q3\_m3$	$q3\_m4$	$q3\_m5$

5.4.2 The equilibration procedure

A number of substrates with specific rough surfaces were generated by means of the PSD in the form of (5.2), as described in section 5.4.1. In order to resolve the unstable atomic steps of the generated rough substrates, these needed to be equilibrated. This procedure was performed with classical molecular dynamics via the large-scale atomic/molecular massively parallel simulator (LAMMPS) [37]. The equations of motion were solved using the velocity-Verlet algorithm [38] with a step size of 10 fs [90]. This time step was tested by a pre-test simulation of an NVE-ensemble to make sure that the system does not exhibit any energy drift. Periodic boundary conditions (PBCs) were applied along the lateral directions. Also, the atoms of the lowest layer were not allowed to move in the z direction. The embedded atom method (EAM) potential [69], with the database developed by Sheng et al. [91], was used for governing the atoms. The temperature was set to 300 K by applying Nosé-Hoover thermostat [113] to all atoms, and the damping constant was set to 0.1 ps. The equilibration procedure was performed for 1.5 ns.

The effects of roughness, crystal orientation, and temperature were investigated in this work. In order to study the effects of the crystal

orientation, different atomic blocks were used in the cutting process; the blocks were dissimilar regarding their crystalline directions along the z coordinate direction. Three dissimilar blocks with crystalline directions of [100], [110], and [111] along the z axis were used in this study. It should be noted that the effects of crystal orientation were studied only on a number of selected systems (see section 5.5.3 for details), and, for the other systems, the [100] direction was set along the z axis. Moreover, the effects of temperature were studied for one selected system (see section 5.5.3 for the details). The temperature was set at different values between zero Kelvin and the melting point of $T_{\mathrm{m}} = 1281$ K [91]. It should be noted that the relaxation at zero Kelvin was done by the molecular statics method, using the Polak-Ribiere version of the conjugate gradient algorithm [114]. This minimization technique iteratively adjusts atoms coordinates in a direction with the steepest potential energy gradient. The procedure continues until the system reaches its local potential energy minimum.

5.4.3 Roughness analyses of the equilibrated substrates

In order to analyze the roughness of the equilibrated substrates, it was first necessary to identify surface atoms. To do so, the method described in Ref. [103] was utilized: a spherical gold particle with a radius of 50 Å and a stepped geometry was equilibrated at 300 K, and the values of the potential energy were used as a criterion for identifying surface atoms, as shown in section 5.5.1. The visualization and structural analyses of the systems were performed using OVITO [40].

Once the surface atoms were identified, their spatial coordinates were used for fitting a surface of the form $h(\mathbf{p})$ to them, using a triangulation-based linear interpolation function, e.g. see [115]. For the fitting process, the $\mathbf{p}$-space extended over [0,0] and $[L, L]$ with a grid spacing of $\delta = \mathrm{a}_0$. Considering $L = 60\mathrm{a}_0$, a 60×60 grid was used for a $\mathbf{p}$-space of size $L \times L$. Then, the fitted surfaces were analyzed for their relevant roughness parameters.

It should be noted that the atoms' positions were not saved as an averaged value over a period of time; the surface analysis was done for each system over the equilibration times between 1.1 ns and 1.5 ns (see Figure 5.3), i.e. each system was analyzed at the different time steps in which the equilibration was achieved, and the average values were reported.

5.5 Results and discussion

Table 5.2 illustrates the rough surfaces of the $\beta 3$ systems, equilibrated at 300 K. The $q3\_\beta 3$ system changed in a way that removed a number of sharp atomistic edges, as can be seen by the significant reduction of sharp peaks and their coalescence into smoother ones in the equilibrated surface. The changes in $q2\_\beta 3$ are smaller, and the changes in $q1\_\beta 3$ can barely be noticed. It should be noted that, although the global minimum potential of the systems would be reached when the substrates are flat, the equilibration process led the systems to their local potential minimum. In other words, the roughness would not disappear unless an activation energy, for example, in the form of heat, is applied to the system to surpass the energy barrier between the local and global potential minima. The effect of temperature was investigated, and the results are discussed in section 5.5.5.

Table 5.2 The atomistic $m3$ rough substrates before and after the equilibration process. The atoms are colored based on their height values, ranging between $\sim 10a_0$ (blue) and $\sim 22a_0$ (red).

	$q1\_\beta 3$	$q2\_\beta 3$	$q3\_\beta 3$
Before Equilibration	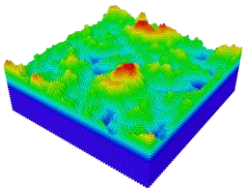	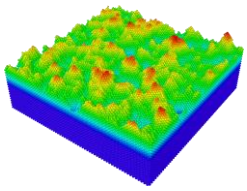	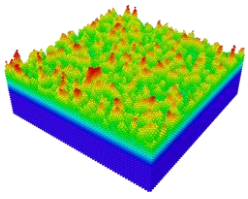
After Equilibration	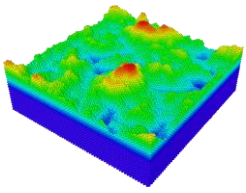	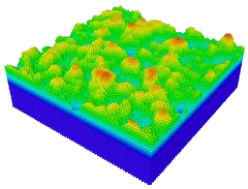	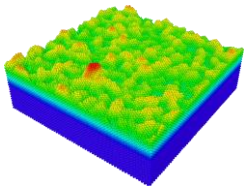

5.5.1 Identifying the surface atoms at 300 K

In order to compare the rough surfaces in a quantitative way, first, the surface atoms were identified. This was done by defining a potential cutoff using a calibration test ([103], see chapter 3), which is based on analyzing the energy distribution of the surface atoms of a spherical nanoparticle. It should be noted that, although the total potential energy of the nanoparticle is not directly comparable with the potential energy of the bulk, due to its large surface area, the potential energy values of the nanoparticle's surface atoms are comparable with those of the surface atoms of the same material, regardless of its shape [103]. Figure 5.2 shows the outer shell of the equilibrated particle, and the potential energy distribution of its atoms. The minimum energy between the δ and ι peaks was selected as the potential cutoff, and its value was found to be $PE_c = -3.5380 \pm 0.0004$ eV. It should be noted that this characteristic potential energy was found to be independent from the applied temperature. Identifying the surface atoms using their potential energy values is very fast, because a simple comparison between the saved potential energies and the cutoff can be used for this identification, and no extra computation is required. Its applicability, however, is limited to perfect crystals, and, if the system has some defects or is not crystalline, other post-processing methods should be applied. For example, the system can be analyzed via a gridding algorithm; see section 5.5.5 for a discussion on this method.

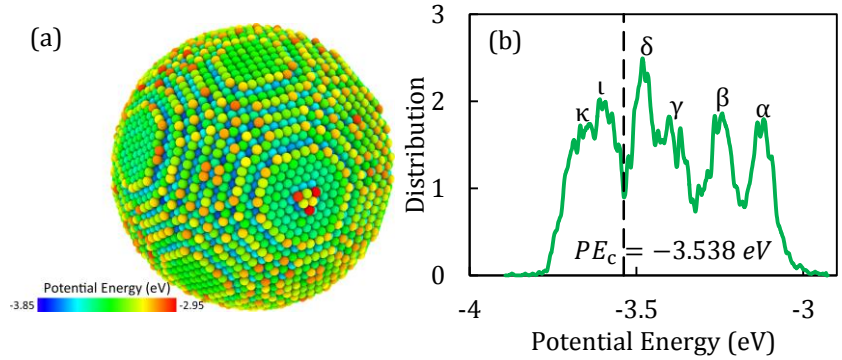

Figure 5.2 (a) A gold spherical particle with a stepped geometry, equilibrated at 300 K. The atoms are colored using their potential energy values. (b) The potential energy distribution of the shell atoms of the equilibrated gold particle. The vertical line indicates the value PE_c that divides the partially contacting atoms from the rest.

The main reason for the configuration changes was the reduction in the potential energy of the surface atoms. Sharp atomic steps and edges impose a high energy value; hence, thermodynamically, the potential energy is reduced until a more stable level is achieved with the removal of high frequency spatial features. The changes in the potential energy were studied by extracting the potential energies of the surface atoms, i.e. atoms with a potential energy higher than the cutoff $PE_c = -3.538$ eV. Then, the average values per atom were calculated, as is shown in Figure 5.3: the potential energy of the surface atoms dropped rapidly during the equilibration; however, after the first drop, the changes became smaller in magnitude. Moreover, the results show that the selected relaxation time of 1.5 ns was long enough for the potential energies of all systems to reach a steady state.

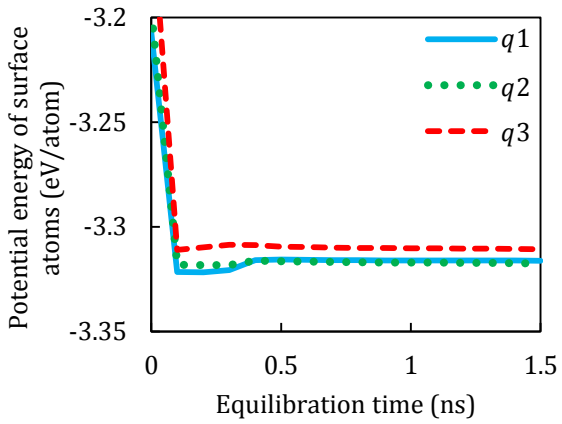

Figure 5.3 The average potential energy per atom (eV/atom) of the surface atoms of $q1$ systems during the equilibration process, at 300 K.

By applying the potential cutoff $PE_c = -3.538$ eV, the surface atoms were identified. After their identification, these were fitted by a surface. Figure 5.4 illustrates the identified surface atoms and the fitted surface of the equilibrated $q1\_\beta3$ system. The fitted surfaces were used for surface analysis; the results are presented and discussed in the following sections.

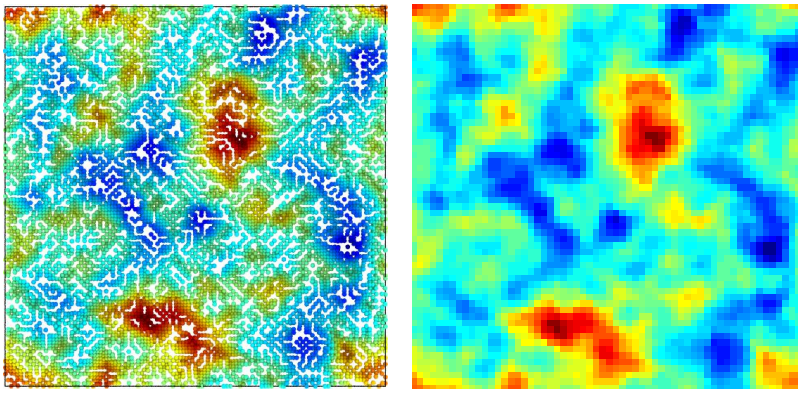

Figure 5.4 This figure illustrates (left) the identified surface atoms, and (right) the fitted surface of the $q1\_\beta3$ system. The white color sections in the left subfigure indicate the gaps between the identified surface atoms along the projected direction. The identified surface atoms were used for fitting a rough surface using a 60×60 uniform grid. This procedure was followed for all systems, and the surface analyses were done on the fitted surfaces. In this figure, the atoms and grids are colored based on their height values: valleys and peaks are colored as blue and red, respectively.

5.5.2 Roughness for $z = [100]$ at 300 K

Three sets of substrates, $q1$, $q2$, and $q3$, with crystal direction [100] along their z axis were equilibrated at 300 K. The roughness of the substrates was characterized via three statistical parameters: lateral correlation length ζ (see section 5.3), RMS gradient $\overline{g} = \sqrt{\langle |\nabla h(\mathbf{p})|^2 \rangle}$, and RMS roughness $\sigma_{\text{rms}} = \sqrt{\langle |h(\mathbf{p})|^2 \rangle}$. Figure 5.5 shows the lateral correlation length and RMS gradient for the rough surfaces, both, before and after equilibration. For the generated surfaces, the lowest lateral correlation length and the highest RMS gradients were calculated to be $\zeta_{\text{min}} \cong 0.5\text{a}_0$ and $\overline{g}_{\text{max}} = 2.08$, respectively. While these two values were not controlled in the surface generating process, some limiting values were found for these two parameters in the equilibrated state: $\zeta_{\text{min}} \cong \sqrt{2}\text{a}_0$ and $\overline{g}_{\text{max}} \cong 1$. While the maximum value of $\overline{g}_{\text{max}} \cong 1$ was smaller than the maximum limiting value of $\sqrt{2}$ for nominally flat rough atomistic surfaces (see Appendix G), $\zeta_{\text{min}} \cong \sqrt{2}\text{a}_0$ can be related to the shortest possible wavelength $\lambda_{\text{min}} = 2\sqrt{2}\text{a}_0$ in an fcc structure, which is four times the shortest interatomic distance in that crystalline structure. Moreover, Figure 5.5 shows

that σ_{rms} for all generated surfaces was originally close to the assigned value of $\sigma_{rms} = 2a_0$. The values of σ_{rms} of the equilibrated systems, however, changed to lower values with different magnitudes.

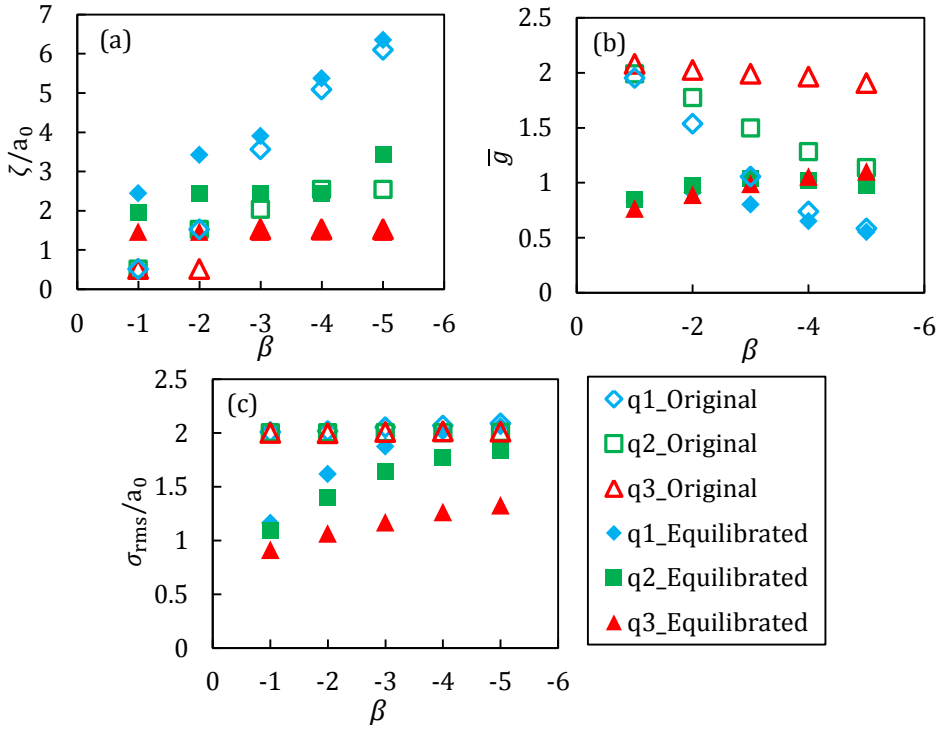

Figure 5.5 The statistical parameters of the rough surfaces: (a) the lateral correlation length normalized by the lattice constant, (b) the RMS gradient, and (c) the RMS roughness normalized by the lattice constant. Note that the systems are differentiated using their q_r values, as described in section 5.4.1.

Before further investigation, let us define a hybrid roughness parameter $\rho = \sigma_{rms}\overline{g}/\zeta$: for a flat surface ($\sigma_{rms} = 0$, $\overline{g} = 0$ and $\zeta = \infty$) $\rho = 0$, and ρ increases as the surface becomes rough with random roughness features, which results in higher values of σ_{rms} and $\overline{g}$ and lower values of ζ. Figure 5.6 (a) shows how the roll-off wavenumber and PSD exponent affect the roughness of the original substrates: higher assigned values of q_r and β resulted in rougher surfaces. In order to compare the roughness parameters before and after the equilibration, their relative change was calculated via

$|\Delta\rho|/\rho_0$, with $\Delta\rho = \rho_{EQ} - \rho_0$, where ρ_{EQ} and ρ_0 are the roughness of the equilibrated and original surfaces, respectively. The results are shown in Figure 5.7. This comparison shows that rougher surfaces experienced larger relative changes in their roughness.

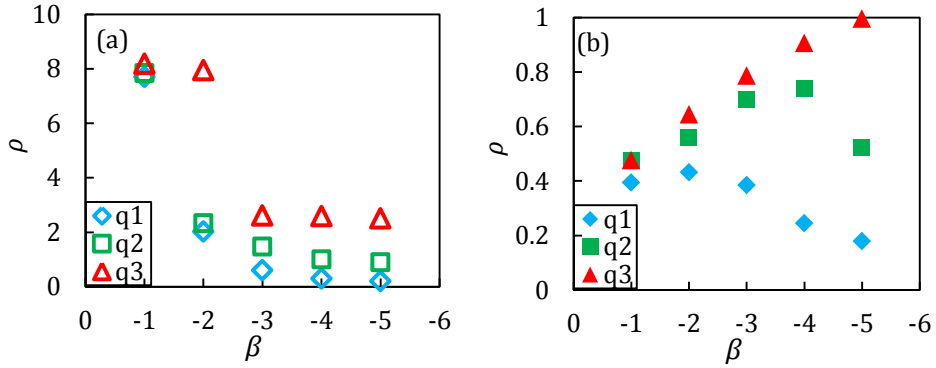

Figure 5.6 The roughness parameter ρ of the substrates (a) before, and (b) after equilibration. Note that the ranges of ρ differ by one order of magnitude between (a) and (b).

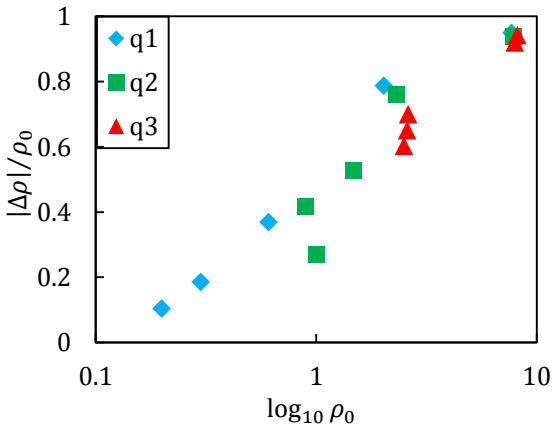

Figure 5.7 The changes of ρ as a function of the roughness of the original surfaces ρ_0.

Comparing the values of ζ and $\overline{g}$ with the corresponding values of ρ (see Figure S3), it was found that $\zeta_{min} \cong \sqrt{2}a_0$ and $\overline{g}_{max} \cong 1$ correspond to the

roughest substrates, and as the substrates become smoother, i.e. $\rho \to 0$, the values of ζ and $\overline{g}$ increase and decrease, respectively. Moreover, the results show that the changes on the RMS roughness were more pronounced on rougher surfaces (see Figure S4). This is due to the fact that the "priority" for a rough surface during equilibration is to lower its energy by becoming smoother, and not to preserve any of its original statistical roughness parameters.

Furthermore, the values of skewness $S_{\mathrm{sk}} = \langle \hat{\mathrm{h}}^3 \rangle / \langle \hat{\mathrm{h}}^2 \rangle^{3/2}$ and kurtosis $S_{\mathrm{ku}} = \langle \hat{\mathrm{h}}^4 \rangle / \langle \hat{\mathrm{h}}^2 \rangle^2$, with $\hat{\mathrm{h}} = \mathrm{h}(\mathbf{p}) - \langle \mathrm{h}(\mathbf{p}) \rangle$, and their changes due to the equilibration process were calculated. Figure 5.8 shows that the skewness values of the height distribution for the original surfaces were close to zero for most systems. For almost all substrates, the equilibration process results in negative values of skewness, which indicates that the effect of the removal of sharp peaks was more dominant than that of the removal of deep valleys [116]. The kurtosis of most of the original rough surfaces was close to, or lower than 3, and the equilibration process lowered the value of this parameter, indicating that the surfaces had relatively few high peaks and low valleys [116]; however, the changes of kurtosis showed no discernible correlation (see Figure S5).

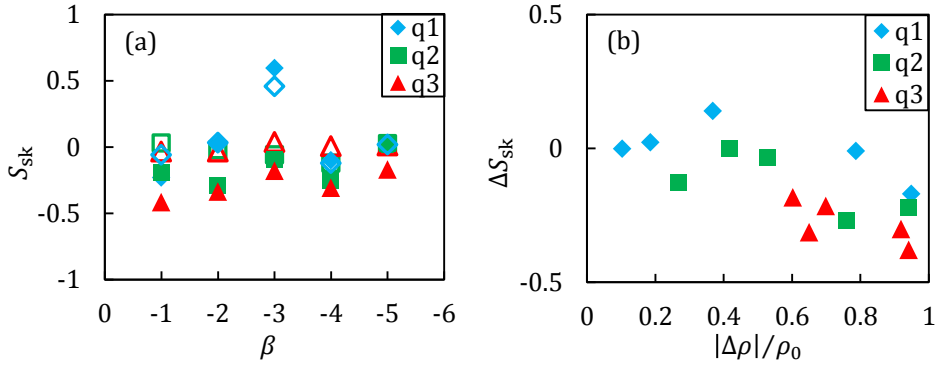

Figure 5.8 (a) The values of skewness of the original (void symbols) and equilibrated (filled symbols) surface roughness. (b) The changes of kurtosis due to the equilibration process.

The rough surfaces were investigated in more detail by analyzing their PSDs. Because the roughness of the substrates was periodic in the lateral directions, there was no need to average the roughness around the edges. Moreover, the highest frequency cutoff was defined using the shortest possible

wavelength in the fcc structure, i.e. $q_S = 2\pi/\lambda_{min}$. Figure 5.9 shows the PSDs of a number of selected systems. As the results show, the equilibrated surfaces lost their high frequency content, i.e. the sharp steps and edges; however, this deviation is not spread over the whole range of wavenumbers, but starts at a specific wavenumber designated as q_{dev} in the remainder of this paper: the equilibrated surfaces preserved their PSD values for wavenumbers smaller than q_{dev}. *The presence of q_{dev} for all of the substrates is evidence that the surface roughness at the atomic scale has fractal characteristics with three segments.*

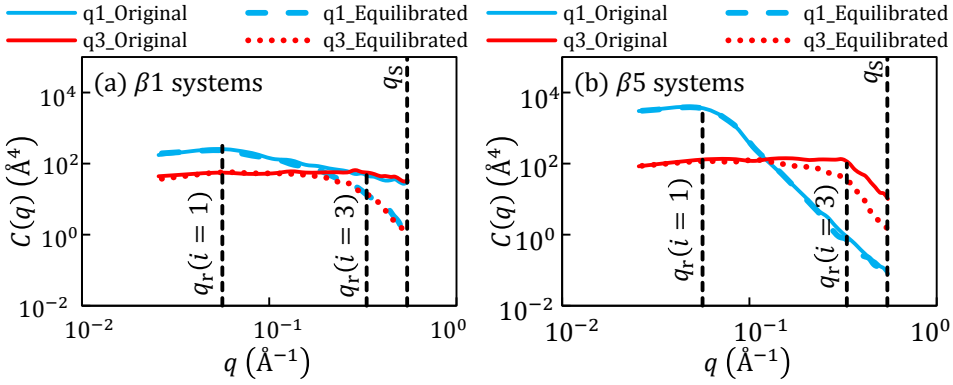

Figure 5.9 The PSDs of a number of selected systems of (a) $\beta = -1$, and (b) $\beta = -5$. Note that the $q2$ systems are not included in the figure for purposes of clarity. The small dashed lines show different parameters: q_S with a value of $\pi/\sqrt{2}a_0$ indicates the validity limit of the PSDs, $q_r(i)$ points to the roll-off wavenumber of the original PSDs, and q_{dev} in (a) shows the wavenumber at which the PSDs of the equilibrated surfaces deviate from the original PSDs.

In order to investigate this deviation, q_{dev} was defined as the smallest wavenumber at which $\left|\frac{C_{relaxed}-C_{original}}{C_{original}}\right| = 0.5$. Figure 5.10 shows the estimated values of q_{dev}. The results show that q_{dev} increases as the surface becomes smoother, which means that a smoother surface loses its original roughness features at higher frequencies compared to a rougher surface. Moreover, comparing the q_{dev} with the corresponding q_r shows whether the PSD has lost its original roll-off wavenumber or not: for $q_{dev} > q_r$ the roll-off wavenumber of the PSD would not change due to equilibration. Based on the results, it can be concluded that assigning lower values of q_r decreases q_{dev}, which means

that the equilibration process does not affect the surface for a wider range of wavenumbers. Moreover, the $q3$ systems showed the smallest values of q_{dev} equal to ~0.2 $\mathrm{Å}^{-1}$.

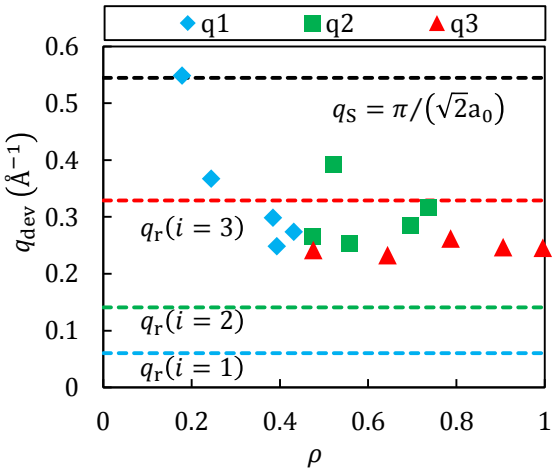

Figure 5.10 The estimated values of q_{dev} as a function of roughness parameter ρ. The q_{r} values are also shown for comparison.

Although q_{dev} points to the deviations of the PSD before and after equilibration, it is important to realize that the original PSD has a great impact even on the deviated section. This influence is illustrated in Figure 5.11, which compares the PSDs of two of the roughest surfaces, i.e. $q3\_\beta1$ ($\rho = 0.87$) and $q3\_\beta5$ ($\rho = 0.61$). This comparison reveals that these two surfaces had very similar high frequency features; however, it is easily noticeable how the original $q_{\mathrm{r}}(i = 3)$ affected the shape of the PSD for wavenumbers between $q_{\mathrm{r}}(i = 3)$ and the corresponding q_{dev}.

Assuming a constant PSD exponent for the high frequencies of the surface roughness, the value of β was estimated. In this estimation, the wavenumbers were bounded between $q_{\mathrm{S}} = \pi/\sqrt{2}\mathrm{a}_0$ and the corresponding q_{dev}. It should be noted that this estimation was done only for the systems for which $q_{\mathrm{dev}} \geq q_{\mathrm{r}}$, i.e. systems $q1$ and $q2$. The results (summarized in Figure S6) suggest a trend of decreasing β for increasing roughness ρ.

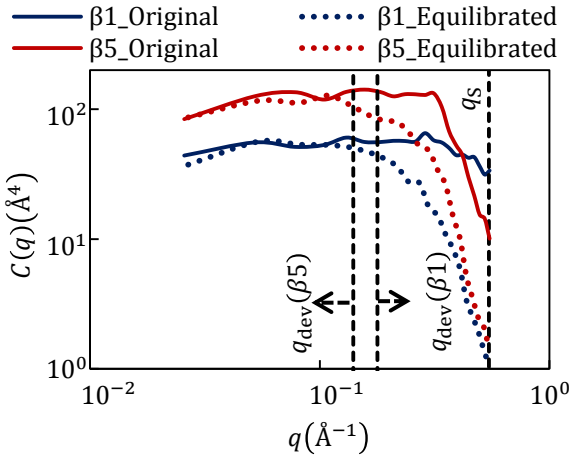

Figure 5.11 The PSDs of the $q3\_\beta1$ and $q3\_\beta5$ systems. Note that the results are copied from Figure 5.9.

5.5.3 Effects of crystal orientation

The effects of crystal orientation were studied for four limiting systems, namely $q1\_\beta1$, $q3\_\beta1$, $q1\_\beta5$, and $q3\_\beta5$, corresponding to the minimum and maximum values of q_r and β. The results were the same as the ones reported in Figure 5.7, and the crystal orientation had negligible effects on the relative changes of roughness (see Figure S7). Moreover, the minimum lateral correlation length was found to be $\zeta_{min} \cong \sqrt{2}a_0$ and independent from the crystallographic orientation.

While the values of the RMS roughness, RMS gradient, and lateral correlation length were found to be independent from the crystallographic orientations, the skewness and kurtosis of the rough surfaces with higher values of β, i.e. those of the $\beta1$ system, showed dependency on the crystallographic orientations (see Figure S8). The results showed the smallest ranges of ΔS_{sk} and ΔS_{ku} for the systems with direction of [111] and [110] along their z axis, respectively.

Moreover, the PSDs of the rough surfaces were analyzed, and the values of q_{dev} were estimated (summarized in Figure S9). The results show that, for almost all systems, changing the crystal orientation from [100] to, either, [110] or [111] resulted in larger values of q_{dev}; however, the value of q_{dev} for the $q3$ systems was smaller than $q_r(i = 3)$ for all directions, meaning that the equilibrated surfaces had lost their originally assigned roll-off wavenumber,

regardless of the crystal orientation along the z axis.

5.5.4 Crystal defects due to equilibration process

While the focus of this work is to study surface roughness and its changes due to the equilibration process, the substrates were also analyzed to investigate whether the changes resulted in the generation and emission of dislocations. The analyses of all systems with $z = [100]$ revealed that a few dislocation lines were generated only in the $q1\_\beta3$ system with a total length of 10 nm (see Figure 5.12). Moreover, the generated dislocations did not grow, and stayed attached to the rough surface, signifying that much thinner substrates can be used for purposes of equilibration. Furthermore, the stress analysis showed that the equilibrated blocks were free of any locally accumulated stress, indicating that the thickness of the blocks was not a constraint to control the movement of the dislocations. A detailed discussion on this issue can be found in the supplementary information.

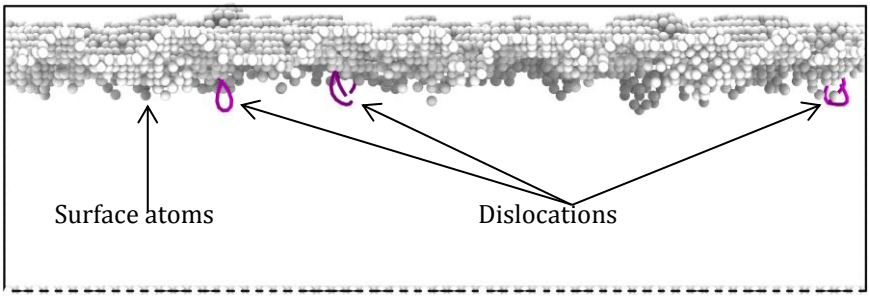

Figure 5.12 The surface atoms and the generated dislocation lines of the equilibrated $q1\_\beta3$ system. The outlines indicate the size of the simulation box.

5.5.5 Effects of temperature

In order to investigate the sensitivity of the results to temperature, the most stable system, $q1\_\beta5$, was selected and equilibrated at different temperatures ranging between absolute zero and the melting point of the simulated material, which is reported to be $T_{\mathrm{m}} = 1281$ K [91]. Figure 5.13 shows the potential energy of the equilibrated systems as a function of temperature. In order to visibly show the melting point, the heat capacity was estimated as $\Delta E/\Delta T$, where ΔE and ΔT are the changes in the potential energy

and temperature between two data points. The sudden jump in the heat capacity between $T/T_{\mathrm{m}} = 0.8$ and $T/T_{\mathrm{m}} = 1.0$ indicates the melting of the system [90].

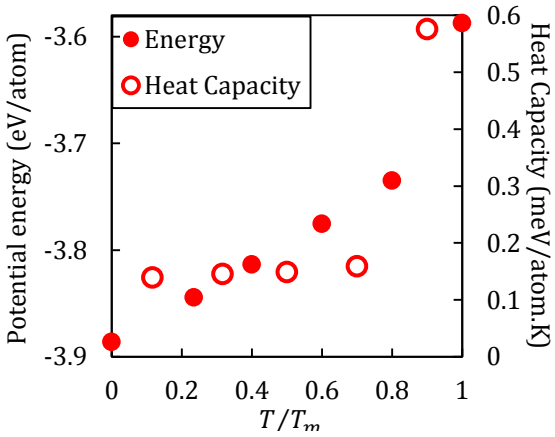

Figure 5.13 The equilibrated potential energy and heat capacity of the systems as a function of temperature.

For the systems at temperatures lower than $T/T_{\mathrm{m}} = 0.8$, the surface atoms were identified as described in section 5.5.1. For the molten system, however, this method would not work because the molten structure affects the potential energy and its distribution throughout the system. Therefore, the surface atoms were detected via a gridding algorithm: the system was divided into bins of size a_0 along the x and y directions, and within each bin, the atom with the maximum z value was selected as the surface atom. The lateral correlation length and PSD of each rough surface was calculated, and the values of ρ and q_{dev} were estimated, as shown in Figure 5.14.

Figure 5.14 (a) shows the calculated roughness of the surface analyzed with two different lateral resolutions (LR) of $1\mathrm{a}_0$ and $5\mathrm{a}_0$. The lateral resolution indicates the lateral distance between two adjacent sampled data; $LR = 1\mathrm{a}_0$ was selected to be consistent with the grid spacing used in the rough surface generating algorithm (see section 4.1), and $LR = 5\mathrm{a}_0 \cong 2$ nm was selected to be comparable with the lateral resolution of measuring devices [117]. The results with $LR = 1\mathrm{a}_0$ show that the roughness slightly increases by changing the equilibrating temperature from 0 K to $0.6T_{\mathrm{m}}$, followed by a slight decrease for $T/T_{\mathrm{m}} = 0.8$, and a sudden drop at the melting point. The mean roughness

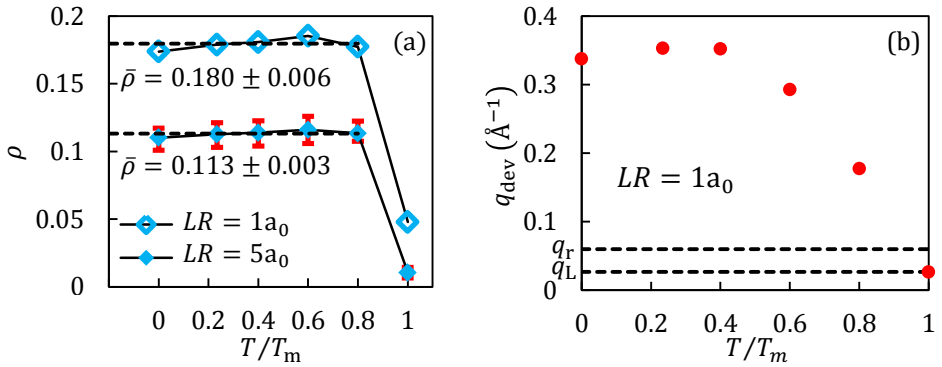

Figure 5.14 (a) Roughness, and (b) deviation wavenumber as functions of equilibrating temperature.

value of the surface at $T/T_m \leq 0.8$ was calculated to be $\bar{\rho} = 0.180$ with an error of 3.3%. Although the dependence of roughness on temperature for $T/T_m \leq 0.8$ was very small, it was not negligible: as the temperature was increased, the system experienced a thermal expansion, which was achieved by the repositioning of the atoms. Due to the PBCs along the lateral directions and the supporting atomic layer at the bottom of the system, which was fixed along the z-axis, the thermal expansion was restricted to only move the free rough surface. The surface atoms with higher potential energy values were the most favorable for changing their positions. As a consequence of the thermal expansion and repositioning process, the roughness could slightly change, and, also, more atoms could be identified as surface atoms; therefore, more data points would be accessible for fitting the surface. Figure 5.15 illustrates the identified surface atoms of the system along the path $0 \leq x \leq L$ at $y = 0.5L$. This figure shows how the thermal expansion affected the spatial coordinates of the surface atoms: for the selected path, the change in the temperature from 0 K to $0.6T_m$ resulted in the identification of 54 and 71 surface atoms, respectively. The higher number of identified surface atoms is related to thermally invoked atomic steps on the free surface, which result in a higher roughness; see Appendix H for a detailed discussion on this behavior.

All of the identified surface atoms were used for fitting a surface as described in section 5.4.3. The results were reported as $LR = 1a_0$ for the case that all of the data points of the fitted surface were analyzed at once; this holds for all of the reported results of this work, with the exception of Figure 5.14 (a), where the results for $LR = 5a_0$ were reported for comparison. For the case of $LR = 5a_0$, the first noticeable result was a lower average roughness

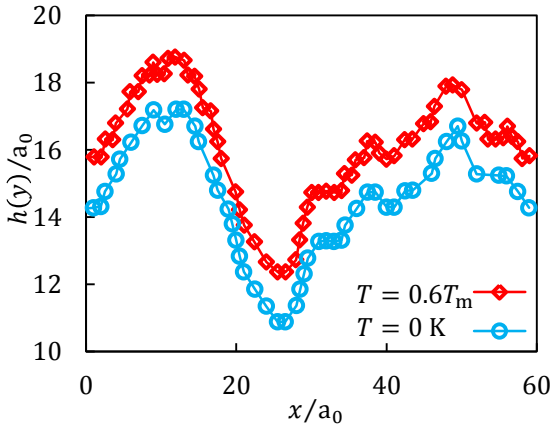

Figure 5.15 The identified surface atoms of the system along the path $0 \leq x \leq L$ at $y = 0.5L$ at two temperatures of 0 K and $0.6T_m$.

compared to the case of $LR = 1a_0$: the average roughness was obtained to be $\bar{\rho}(LR = 5a_0) = 0.113$ compared to $\bar{\rho}(LR = 1a_0) = 0.180$ at $T/T_m \leq 0.8$. Furthermore, the larger sampling lateral resolution made it possible to analyze the surface more than once, and the results were reported with the corresponding measurement errors. Figure 5.14 (a) shows that the calculated roughness values for $LR = 5a_0$ at $T/T_m \leq 0.8$ were more or less in the same range regardless of temperature, without any meaningful difference. In another words, an LR of $5a_0$ is large enough to cover any meaningful changes of roughness at a temperature range of $T/T_m \leq 0.8$. On the other hand, the changes of roughness would become clearer by studying the q_{dev} values, as shown in Figure 5.14 (b); the deviating wavenumber is temperature-independent for $T/T_m \leq 0.4$. At higher temperatures, the value of q_{dev} decreases. At the melting point, q_{dev} reaches the value of q_L, indicating that the surface of the molten substrate has lost its original roughness features.

Figure 5.16 shows the atomic structure of the substrates at $T/T_m = 0$ and $T/T_m = 1$; this figure confirms that the very low value of $\rho \cong 0.05$ indicates that the surface is nearly flat. Although the roughness parameter ρ is close to its theoretical minimum of zero (see section 5.2), it does not reach this value at the melting point due to the presence of thermally excited capillary waves. Instead, the roughness parameter is calculated to be $\rho \cong 0.07$ at the melting point for the simulated systems, as discussed in detail in Appendix H.

Studying the effects of temperature shows that the deviating wavenumber is temperature-independent for $T \leq 0.4T_m$.

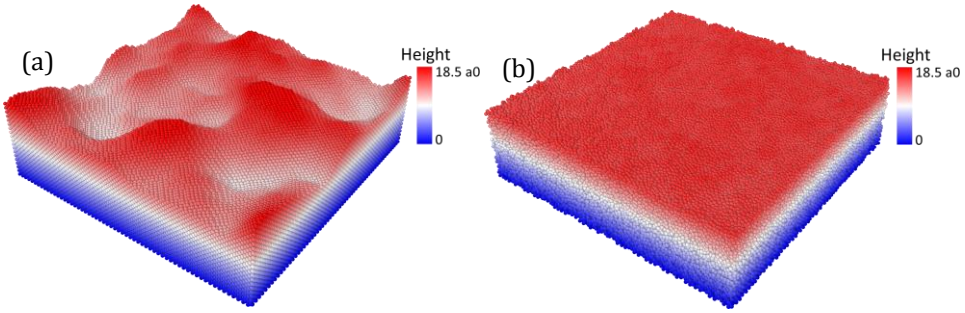

Figure 5.16 The atomic structure of the equilibrated substrate at (a) $T/T_{\mathrm{m}} = 0$ and (b) $T/T_{\mathrm{m}} = 1$. The atoms are colored based on their height values.

5.5.6 Generating pseudo-stable systems

In order to generate a pseudo-stable rough substrate, two different methods can be proposed based on the results of the investigated systems: one would be to set the cutoff wavenumber of the PSD to some value smaller than or equal to the minimum of the deviating wavenumbers, i.e. $q_{\mathrm{S}} \leq \min(q_{\mathrm{dev}}) \cong 0.2\ \text{Å}^{-1}$. This value translates into a wavelength of $\lambda \cong 8\mathrm{a}_0$ and, although not being related to any critical length in an fcc structure, it can be compared with the current lateral resolution of atomic-force microscopy (AFM) utilizing carbon nanotube tips, which can resolve features as smalls as ~2 nm [117]. For an fcc structure, however, the lateral resolution is relevant down to the interatomic spacing, where the PSD cutoff wavenumber needs to be defined by means of the shortest possible wavelength. Therefore, another method needs to be applied for resolving the deviation issue: the PSD can be described via expanding (5.2) into a three-segment PSD:

$$C(\mathbf{q}) = \begin{cases} C_0 & q_{\mathrm{L}} \leq \|\mathbf{q}\| < q_{\mathrm{r}} \\ C_0(\|\mathbf{q}\|/q_{\mathrm{r}})^{\beta_1} & q_{\mathrm{r}} \leq \|\mathbf{q}\| \leq q_{\mathrm{dev}} \\ C_1(\|\mathbf{q}\|/q_{\mathrm{dev}})^{\beta_2} & q_{\mathrm{dev}} \leq \|\mathbf{q}\| \leq q_{\mathrm{S}} \\ 0 & \text{elsewhere} \end{cases} \tag{5.4}$$

with

$$C_1 = C_0(q_{\mathrm{dev}}/q_{\mathrm{r}})^{\beta_1}\,. \tag{5.5}$$

Following the discussion in Appendix F and using (F.1), in order to generate a rough surface tuned to an assigned value of σ_{rms}, the value of C_0 needs to be calculated from

$$C_0 = \frac{\sigma_{\mathrm{rms}}^2}{2\pi} V^{-1}, \tag{5.6}$$

with

$$V = \frac{q_{\mathrm{r}}^2 - q_{\mathrm{L}}^2}{2} + q_{\mathrm{r}}^{-\beta_1} \left(\frac{q_{\mathrm{dev}}^{2+\beta_1} - q_{\mathrm{r}}^{2+\beta_1}}{2+\beta_1} + q_{\mathrm{dev}}^{\beta_1-\beta_2} \frac{q_{\mathrm{S}}^{2+\beta_2} - q_{\mathrm{dev}}^{2+\beta_2}}{2+\beta_2} \right). \tag{5.7}$$

In order to examine the applicability of the proposed methods, three different surfaces were generated: one surface using (5.2) with $q_{\mathrm{S}} \cong 0.2\ \text{Å}^{-1}$, and one using (5.3) with $q_{\mathrm{S}} \cong 0.2\ \text{Å}^{-1}$ and $\zeta = 5\mathrm{a}_0$; the PSD exponent for these two surfaces was selected to be $\beta = -3.5$. The third surface was generated using (5.4) with $q_{\mathrm{dev}} \cong 0.2\ \text{Å}^{-1}, q_{\mathrm{S}} = 2\pi/\lambda_{\mathrm{min}}, \beta_1 = -3.5$, and $\beta_2 = -4.5$ (see Figure S6). The RMS roughness for all of surfaces was selected to be $\sigma_{\mathrm{rms}} = 2\mathrm{a}_0$. The generated surfaces were used for building corresponding substrates as described in section 5.4.1, and the substrates were relaxed at zero Kelvin via the conjugate gradient algorithm [114], as described in section 5.4.2. The reason for relaxing the systems at zero Kelvin is based on the findings of section 5.5.5: the changes of the surface roughness are temperature-independent for $T \leq 0.4T_{\mathrm{m}}$.

Figure 5.17 shows the PSDs of the rough surfaces before and after the equilibration process: the results show no difference between the original and equilibrated PSDs. In other words, both of the proposed methods can be used to generate pseudo-stable rough substrates.

Furthermore, the applicability of the proposed methods was studied via another set of three surfaces, where all parameters were the same as the previous ones, but their RMS roughness was set to a larger value of $\sigma_{\mathrm{rms}} = 5\mathrm{a}_0$. The PSDs of the rough surfaces are shown in Figure 5.18 : while there is no difference between the original and equilibrated PSDs for wavenumbers smaller than $0.2\ \text{Å}^{-1}$, deviations can be detected for larger wavenumbers.

5.6 Conclusions

The results of this investigation show that rough surface topography needs to be defined in a physically meaningful manner for implementation in atomistic simulations. Thermodynamically, rough surfaces under equilibration tend to have their atomic steps and edges removed in order to lower the potential energy of the system, and reach the local minimum of energy; as a result, the equilibration procedure smoothens the rough surfaces as the

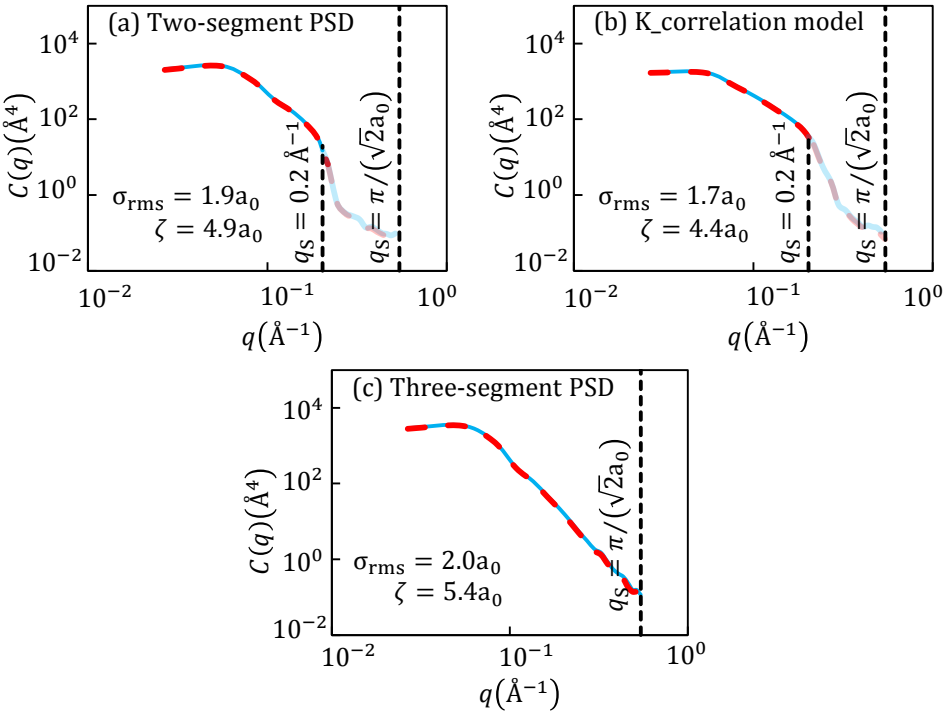

Figure 5.17 The PSDs of the surface roughness of the generated (continuous line) and equilibrated substrates (dashed line). The surfaces were generated using (a) the two-segment PSD (5.2), (b) the K-correlation model (5.3), and (c) the extended PSD model in the form of (5.4) It should be noted that the PSDs used for generating surfaces in (a) and (b) had a cutoff of $q_S = 0.2$ Å^{-1}; however, for analyzing the surfaces, a natural cutoff of $q_S = 2\pi/\lambda_{min}$ was used. That is why the plots are shown with a different shading between the assigned cutoff and the natural one.

changes of skewness and kurtosis of the equilibrated surfaces under investigation in this work confirm.

In this chapter, different quasi-fractal rough surfaces were generated, which were used for constructing rough atomistic blocks of gold with different crystal orientations. Then, the blocks were relaxed and equilibrated at different temperatures. The surface roughness of the equilibrated substrates was analyzed and compared with the corresponding original rough surface. In order to study the surface roughness, a hybrid roughness parameter was defined as $\rho = \sigma_{rms}\overline{g}/\zeta$, which has a value of $\rho = 0$ for a perfectly flat surface, and increases as the surface becomes randomly rougher.

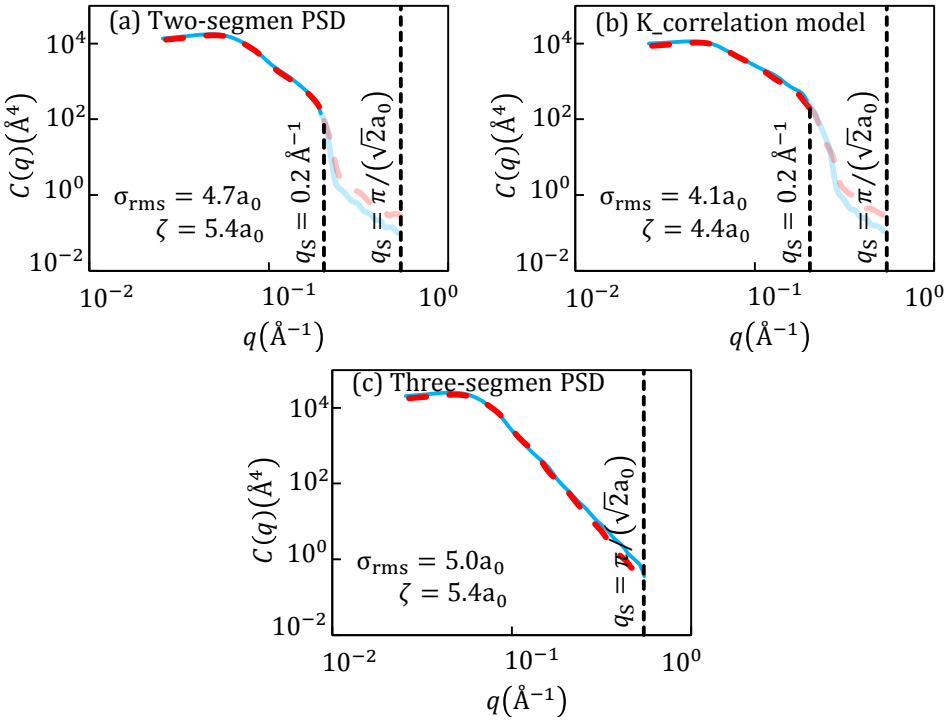

Figure 5.18 The PSDs of the surface roughness of the generated (continuous line) and equilibrated substrates (dashed line). The surfaces were generated using (a) the two-segment PSD (5.2), (b) the K-correlation model (5.3), and (c) the extended PSD model in the form of (5.4). For the explanation of different values of q_S on (a) and (b), the readers are referred to the caption of Figure 5.17 .

It was found that rougher surfaces experience larger roughness changes, and the dependence of these changes on crystal orientation is negligible. Moreover, the changes in the surface roughness were found to be temperature-independent for $T/T_m \leq 0.4$.

Furthermore, the rough surfaces were analyzed through their PSDs. It was found that the substrates could hold their original PSDs up to a wavenumber denoted as q_{dev}, where the deviation occurred for larger wavenumbers. A minimum value of $0.2\ \text{Å}^{-1}$ was found for this deviating wavenumber, i.e. $q_{dev} \geq 0.2\ \text{Å}^{-1}$. This finding was used for proposing two different methods to generate pseudo-stable rough substrates: one is to set the high frequency cutoff to the obtained minimum value for the q_{dev}, i.e. $q_S = 0.2\ \text{Å}^{-1}$. This

situation can be amenable to comparisons with measurements performed with an AFM utilizing carbon nanotube tips featuring a high lateral resolution of ~2 nm [117]. This method was tested for different systems, where the results showed no differences in their PSD before and after the relaxation process. The other method for generating rough surfaces was obtained by defining a three-segment PSD, described in (5.4). The method was tested for two different RMS roughness values of $2a_0$ and $5a_0$. Analyzing the PSDs showed that, for the substrate with $\sigma_{\mathrm{rms}} = 2a_0$, there were no changes in the surface roughness due to the relaxation process; however, the substrate with $\sigma_{\mathrm{rms}} = 5a_0$ showed deviations at high wavenumbers larger than $q_{\mathrm{dev}} = 0.2\ \text{Å}^{-1}$. The detected deviations in the final simulations (see Figure 5.18) for wavelengths larger than $q_{\mathrm{S}} = 0.2\ \text{Å}^{-1}$, indicate that, if the lateral resolution needs to be finer than 2~3 nm, the system has to be relaxed regardless of its initial roughness, otherwise the rough surface representation would be non-physical.

The results of the current investigation reveal that rough surfaces used in atomistic simulations need to be properly equilibrated, regardless of their initial roughness, unless lateral resolutions finer than $\sim 8a_0$ are not of interest. It should be noted that this statement would be valid only for the roughness of free surfaces, i.e. before the occurrence of any type of contact; the changes of the surface roughness due to contact are not the focus of this research and have been studied extensively [8, 66, 70, 78-80, 102].

Finally, for the relaxation process, the initial block does not need to be thick, because dislocation emissions, if any, tend to be extremely limited during equilibration. Moreover, if the simulation temperature is lower than $0.4T_{\mathrm{m}}$, molecular statics (resembling 0 K), instead of molecular dynamics, can be employed to relax the rough substrate.

Chapter 6

Concluding remarks

In this chapter, the main contributions of this thesis are summarized in a list, and a number of possible topics are suggested for carrying forward the present work.

6.1 Contributions

This thesis has studied different topics of nanotribology by means of classical MD simulations. Its main contributions can be summarized as follows:

- The contact between different types of single asperities and flat substrates was studied, and the MD simulation results were compared with the corresponding models of continuum contact mechanics, i.e. the Hertzian theory for non-adhesive contacts, and the JKR and DMT models for adhesive ones. The comparisons showed that, as long as the deformation is purely elastic, the continuum contact mechanics models could correctly predict the contact force and the real contact area.

- In the study of the contact between a single asperity and a flat surface, the crystal structure of the deformed bodies was investigated, and it was found that the reversibility of the deformation alone is not a sufficient criterion for deciding on the applicability of the continuum contact mechanics models for describing the contacts. The results showed that the generated dislocations in the early stages of indentation resulted in reversible plastic deformation. In other words, if the load is removed in the early stages of deformation, the internally stored force induces a reverse motion of defects, and results in a complete recovery. Therefore, while the deformation of the system is reversible at this stage, the generation of dislocations initiates some atomic steps at the interface of the contact. These atomic steps have minor effects on the indenter's force, but noticeably increased the real contact area.

- In order to study the contact area, it is important to decide whether the focus is the real contact area or the projected contact area. Based on this decision, different methods of analysis can be utilized: studying the contact based on the contact energy, which is accessible in atomistic simulations, yields the real contact area, while the projection of non-contacting atoms yields the projected contact area. Moreover, there is an intermediate solution to this problem, in which the contacting atoms can be identified by means of a contact distance. Using this method, both, the real contact area, from the product of the number of contacting atoms and the atomic "contact area" $N_{ca}A_a$, as well as the projected contact area, via analyzing the graphical projection of the identified atoms, can be estimated.

- Assuming a constant value for the atomic contact distance d_c throughout the whole course of the indention process, the normalized radial distribution function $g(r)$ is found to be the most reliable tool for calibrating d_c, because the effect of temperature on the contact distance is already reflected in the calculated $g(r)$, while this is not the case for calibrating d_c using the distance at the minimum of the potential energy. Moreover, if the contact distance is going to be calibrated solely from the minimum of the interacting potential energy at contact, the method would fail for non-pairwise potentials.

- By studying the $g(r)$ of the NPT ensemble for different atomistic systems, it was proposed that the distance where the first peak of the $g(r)$ reaches its maximum is a valid approximation for defining the diameter of an individual atom: the validity of this proposition was tested via comparing the results of MD simulations and continuum theories of the sphere on flat problem, both, for non-adhesive and adhesive cases.

- By scrutinizing the sphere on flat problem for, both, adhesive and non-adhesive contacts, the atomic contact distance was found to be variable. For the non-adhesive case, the contact distance was calibrated at the latest valid point, i.e. while the deformation was purely elastic, and before the small size of the system noticeably affected the material's response. In doing so, the contact distance was found to be a function of the asperity radius. The results, however, suggested that the contact distance is not only a function of the

asperity radius, but is also a function of the distance between the asperity and the flat substrate. This initial finding was verified for the case of adhesive contact: the results showed that the contact distance remained constant away from the instances of pull-in and pull-off, while its value increased for the initial and ending stages of the contact, i.e. prior to pull-in and after pull-off, respectively.

- Non-adhesive contact between atomistic single asperities with different radii and a flat substrate in the elastic deformation regime was examined in the context of Hertzian theory. The results showed that, at the early stage of indentation, i.e. ~4 Å of indentation depth in our studies, the contact modulus E^* was not constant, but a function of the indenter's radius and the indentation depth.

- The non-adhesive contact between two different rough surfaces and a flat one was studied, and the results were compared with the theories of Greenwood-Williamson [82] and Persson [83, 84]. The results showed that both theories overestimate the projected contact area, even with the initiation of plastic deformation in the atomic system, which would increase the real contact area of the MD simulations. Moreover, the results showed that the Persson theory could correctly predict the projected contact area, if the diffusion coefficient of this theory, denoted as G, was estimated via the fitting of a double Gaussian function to the interfacial pressure distribution of the system, which is accessible in atomistic simulations.

- A number of rough substrates were analyzed, and it was found that the atomic systems cannot hold every arbitrarily defined topography: the high frequency roughness would be smoothened because it is thermodynamically unstable. In order to define a pseudo-stable rough surface, a number of solutions were proposed. Furthermore, the results showed that the surface roughness of the substrates is temperature-independent for temperatures equal to and lower than $0.4T_{\mathrm{m}}$, where T_{m} is the melting point of the material in the Kelvin scale. From a practical point of view, this finding is highly valuable, because if the roughness is temperature-independent for a given system, the rough substrate can be relaxed via molecular statics, resembling 0 K, instead of having to equilibrate the substrate by molecular dynamics.

6.2 Recommendations

In this research we investigated a number of problems in nanotribology by means of classical MD simulations, and compared the results with the corresponding continuum theories. Although we have analyzed different problems, from the definition of contact to the applicability of continuum mechanics theories at the atomic scale, and proposed solutions to define a physically meaningful roughness for atomic blocks, several issues and problems still remain to be addressed in future work. In order to be specific, we propose the following lines of research, in which the current work can be considered as a starting point.

- It is of interest to study the applicability of elastic-plastic contact models, whether analytical or empirical solutions, e.g. [118-120], to the nanoscale. In case that these models cannot correctly capture the behavior of contacts at the atomic scale, MD simulation results could be used for establishing empirical fits or phenomenological models.

- For nano devices, a relevant issue is to study the contact between an indenter and a polycrystalline substrate. If the substrate is considered to be a nano coating, the effects of the finite size have practical impacts on the results.

- Studying the roughness of fracture surfaces generated via atomistic simulations of fracture processes will add to our knowledge of the natural roughness of surfaces at the atomic scale.

- By studying the sphere on flat problem, the results showed the dependence of the atomic contact distance d_c on, both, the effect of the indenter's size R for the non-adhesive, and the penetration depth d for the adhesive cases. It would be of interest to carry out a full investigation on the non-adhesive and adhesive cases, in order to describe d_c as a function of, both, R and d.

Appendix A. Sliding contacts of lubricated randomly rough surfaces*

A.1 Introduction

The friction of contacting interfaces is a function of surface roughness, normal load, temperature, sliding velocity, and environmental parameters: e.g., under boundary lubrication, the frictional behavior changes as a function of wettability, viscosity, and density of the applied lubricant, by practically decreasing the possibility of dry (solid/solid) contact. Many atomistic studies of rough contacts adopt simplified sinusoidal shapes for the roughness, and model the interface as that between a deformable surface and a rigid flat; however, as shown in Chapter 5, roughness has a random nature down to the atomic scale. This appendix presents some early results on the frictional behavior of lubricated rough contacts.

A.2 Simulation Methodology

Figure A1 summarizes the simulation setup and the contact process, which was performed in two phases: normal and sliding contacts. The following sections discuss the details of the simulations.

A.2.1 Setup

A pair of Gaussian randomly rough surfaces was generated with a root-mean square roughness and correlation length of 10 Å and 8 Å, respectively. These were used for constructing two atomic blocks of fcc-nickel with the (100) lattice planes normal to the z direction. The solid structure was built with a length of $40a_0 \cong 14.1$ nm in the lateral directions, with $a_0 = 3.52$ Å being the lattice constant of nickel, and a minimum thickness of 2.5 nm for each block. Each of the two bodies was divided into three layers: rigid,

* This appendix has been originally published in conference abstracts of "TriboUK 2015 (England, April 2015)", and "The international conference on understanding and controlling nano and mesoscale friction (COSTnanoTribo), (Turkey, June 2015)".

thermostatic, and free deformable. Moreover, different numbers of n-hexadecane molecules, i.e. 0, 192, 576, and 960, formed a lubricant film. The molecules were modeled through the TraPPE potential energy, while the embedded-atom method potential database developed by Zhou et al. was used for governing the nickel atoms. Also, the Lennard-Jones (LJ) potential was used for calculating the interactions between the non-bonded atoms of the lubricant molecules, as well as the molecules and the substrates. It should be noted that the LJ parameters for nickel were collected from the Shu and Davies database.

The equations of motion were solved using the velocity-Verlet algorithm [38]. Periodic boundary conditions were applied to the lateral directions. The weak coupling thermostat [39] was applied to the thermostat layers to keep the temperature at 300 K.

A.2.2 Procedure

First, the case of normal contact was studied: the rigid layer of a block was fixed, and the other was moved to apply a pressure of 0.5 kPa. This process was performed for a total simulation time of 3 ns, which was found to be long enough for the potential energy to reach a steady-state. Following normal contact, the rigid layer was moved with a constant velocity of 25 m/s along the x axis for 3 ns.

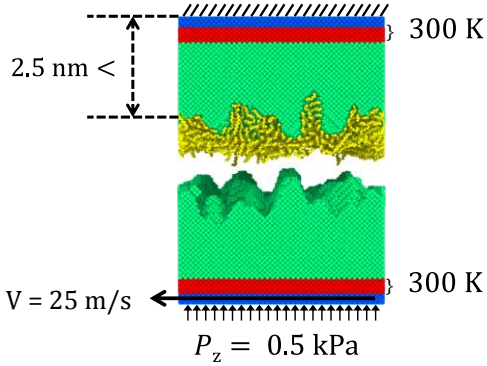

Figure A1 The atomistic system setup with 960 n-Hexadecane chains, and the details of the contact parameters. It should be noted that the process started with a normal contact, and the sliding contact was simulated only after the potential energy of the system reached a steady-state. In this figure, the atoms of the alkane chains and of the fixed, thermostatic, and Newtonian groups are colored as yellow, blue, red, and green, respectively.

A.3 Identifying the solid/solid contacting atoms

In lubricated systems, the dry contact may form at different spots if the substrates are not fully covered with the lubricant molecules. These contacting atoms can be identified through defining a contact distance as described in Chapter 3. This method, however, is applicable only for the normal contact phase, in which none of the atoms would leave their original block due to the contact. On the other hand, as soon as the sliding process starts, a number of atoms from each block would stick to the other block, and the system may experience a huge amount of atom transfer. Consequently, the contact distance loses its reliability, because each atom would be recognized as a member of its original substrate, whether it has transferred away from it or not. In order to solve this problem, different approaches can be used based on the mean velocity of atoms [9] or the detection of atom transfer [8], as discussed in Chapter 3. Following the method described therein, a potential cutoff of $PE_c = -3.965$ eV was defined to identify solid/solid contacting atoms in boundary lubrication. This method needs less computational resources than the method proposed by Spijker et al. [8], and also suffers less from fluctuations compared to the proposed method of Eder et al. [9]. However, there is a main and important limitation in this method: if the system contains different elements, it is highly possible that the method will fail. Chapter 3 provides a detailed review of this method.

A.4 Results and discussion

Changing the lubricants' volume affected the shearing force as well as the stability of the system. The corresponding results are summarized in Figure A2. Moreover, as illustrated in Table A1, it was found that larger volumes of lubricant localized the dry interactions, and lowered the area of the dry contacting spots, where the atom transfer process occurs. By applying the potential energy cutoff, the non-contacting atoms were identified with ease (see Table A2). The results show that the contacting spots decreased by using larger amounts of lubricant, whether the contact was normal or frictional. Furthermore, the non-contacting area shrunk significantly due to the movement of atoms induced by friction.

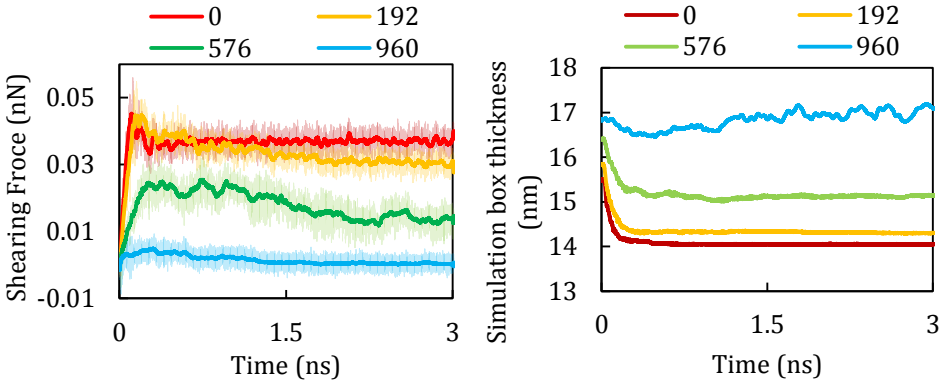

Figure A2 The effects of the amount of applied lubricant on (left) shearing force, and (right) simulation box thickness.

Table A1 Side view of the contacting system: the explanation of the colors can be found from the caption of Figure A1. The black strip shows the position of a number of selected atoms before and after the sliding process. Note that the thickness of the system increases for larger amounts of lubricant; the lubricant's chains are not shown.

No. of lubricant molecules	0	192	576	960
Beginning of sliding process	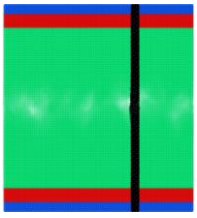	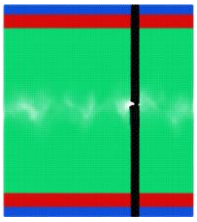	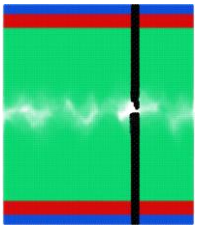	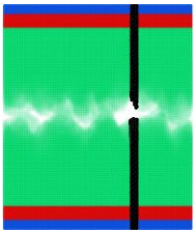
End of sliding process	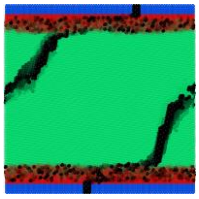	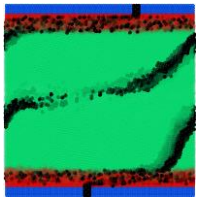	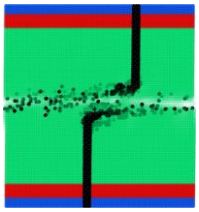	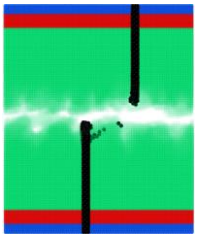

Table A2 Top view of the non-contacting surface atoms (black dots) via their potential energies. Note that the white area indicates the contacting area.

No. of lubricant molecules	0	192	576	960
Beginning of sliding process	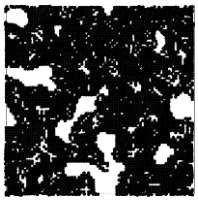	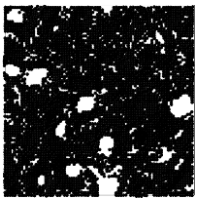	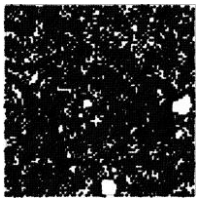	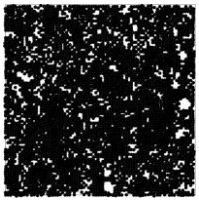
End of sliding process	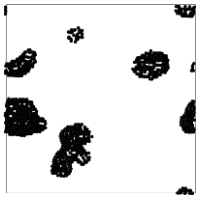	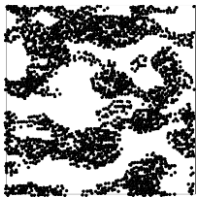		

Appendix B. Contacts with limited adhesion*

B.1 Introduction

The difficulties in defining the atomic contact distance for, both, adhesive and non-adhesive contacts were discussed in detail in Chapters 2, 3 and 4. It was shown that non-adhesive contacts can be calibrated with the Hertz formula (Chapter 4). On the other hand, adhesive contacts do not need to be calibrated through continuum mechanics solutions: the normalized radial distribution function (RDF) can be used for defining the contact distance; the results would be in agreement with the continuum mechanics solutions, as long as the contact does not deviate from some of the continuum mechanics assumptions, namely that the system is homogenous and that plastic deformation has not been initiated. It should be noted that, in this method, i.e. defining contact distance using RDF, there is one assumption: the atoms of the contacting surfaces are the same as the ones used for calculating the RDF. In other words, if the RDF describes a system composed of a pure element, the contacting surfaces should be pure as well. In real contacts, however, it is unlikely to have fully clean surfaces, for example, due to oxidation. This issue can greatly affect the adhesive forces: in case of oxidation, the adhesion would be lowered. This issue can be addressed differently in the simulations by:

1- Introducing different elements into the system. As a result, the contacting surfaces would interact following their potential energies, and the contact distance could be defined using the corresponding RDFs.

2- Changing the potential energy values only between the interacting surfaces, in order to artificially incorporate this effect. Using this method, the interacting forces between the contacting surfaces would be different from the forces between the atoms of the substrates. In other words, the contact behaves differently from what the calculated RDFs would suggest.

* This appendix has not been presented/published elsewhere yet.

The second method is more favorable for MD simulations, e.g. see [8, 70, 78, 79, 102], mainly because it would be computationally less expensive than method 1. The incapability of using RDFs for this case, however, makes the analysis of contacts no longer straightforward. In this appendix, the sphere-on-flat elastic contact problem was addressed for the case of limited adhesion. The results were then compared with the JKR theory.

B.2 A short review of the JKR theory

The JKR theory, among others, was briefly reviewed in Chapter 2. It was developed by incorporating the effect of adhesion in the Hertz theory via an additional pressure distribution [14]:

$$p_{(l)} = p_0\left(1-\left(\frac{l}{r}\right)^2\right)^{1/2} - \acute{p}_0\left(1-\left(\frac{l}{r}\right)^2\right)^{-1/2}, \tag{B.1}$$

where r is the contact radius, and l is the radial distance from the center of the contact, ranging between 0 and r. The first term of the right hand side is the Hertzian repulsive pressure distribution, and the second term is the pressure distribution responsible for adhesion inside the contact area. For contact between two spheres, the values of p_0 and $\acute{p}_0$ would be $2rE^*/\pi R$and $\sqrt{2\Gamma E^*/\pi r}$, respectively.

Johnson et al. [14] solved the pressure distribution for the case of two contacting spheres, and showed that the effectively acting loading force (F_{JKR}) is larger than the normal applied load ($F_\perp$):

$$F_{\mathrm{JKR}} = F_\perp + F_\Gamma \pm (2F_\Gamma F_\perp + F_\Gamma^2)^{1/2}, \tag{B.2}$$

with $F_\Gamma = 3\Gamma\pi R$. Furthermore, they discussed that the positive sign should be considered for a stable solution. Using this theory, the radius of the contact area can be described as:

$$r = \left((4R/3E^*)\left(F_\perp + F_\Gamma \pm (2F_\Gamma F_\perp + F_\Gamma^2)^{1/2}\right)\right)^{1/3}, \tag{B.3}$$

which results in a pull-off force of $F_{\mathrm{po}} = -3/2\,\Gamma\pi R$. Comparing F_{po} and F_Γ, it can be shown that $F_\Gamma = -2F_{\mathrm{po}}$. Therefore, (B.2) can be rewritten as:

$$r = \left((4R/3E^*)\left(F_\perp + -2F_{\mathrm{po}} \pm 2\left(-F_{\mathrm{po}}F_\perp + F_{\mathrm{po}}^2\right)^{1/2}\right)\right)^{1/3}. \tag{B.4}$$

For the case of $F_\perp = F_{\mathrm{po}}$, the radius of the contact area would be

$$r_{F_\perp = F_{\mathrm{po}}} = \left((4R/3E^*)\left(-F_{\mathrm{po}}\right)\right)^{1/3}. \tag{B.5}$$

Furthermore, the indentation depth d would be obtained as

$$d = \frac{r^2}{R} - \left(2\frac{\pi\Gamma r}{E^*}\right)^{1/2}, \tag{B.6}$$

which can be rewritten by inserting F_{po} in it as follows:

$$d = \frac{r^2}{R} - 2\left(-\frac{rF_{\mathrm{po}}}{3E^*}\right)^{1/2}. \tag{B.7}$$

Moreover, it can be shown that, for the case of $F_\perp = F_{\mathrm{po}}$, the following holds:

$$d_{F_\perp = F_{\mathrm{po}}} = -\frac{1}{3}\left(-\frac{3F_{\mathrm{po}}}{4E^*\sqrt{R}}\right)^{2/3}. \tag{B.8}$$

B.3 Simulation Methodology

Two sets of simulations were performed: one for the single asperity contact, and one for the calculation of the work of adhesion. The schematics of the systems are depicted in Figure B1.

The systems were generated from fcc-calcium with a lattice constant of $a_0 = 5.5884$ Å [91]. The movements of the deformable atoms were governed by the EAM potential database developed by Sheng et al. for calcium [91]. For the contacting surfaces, the standard LJ potential was used, with $\varepsilon = 0.21445$ eV and $\sigma = 3.5927$ Å [71]; in order to simulate the limited adhesion, however, the depth of the potential well was modified to be $c\varepsilon$, with $c \in \{0, 0.1, 0.2, \dots, 1\}$. Moreover, a cutoff radius of $r_{\mathrm{cutoff}} = 2.5\sigma$ was applied to the potential, with the standard GROMACS shift function [121] between a distance of $r_{\mathrm{shift}} = 2\sigma$ and r_{cutoff}; this shift function assures that there is no jump of energy and force at the cutoff

The equations of motion were solved via the velocity-Verlet algorithm [38]. The temperature of the assigned layers was set to 300 K using Berendsen's thermostat [39]. The crystalline direction of [111] was defined as the z coordinate direction, and periodic boundary conditions were applied along the lateral directions.

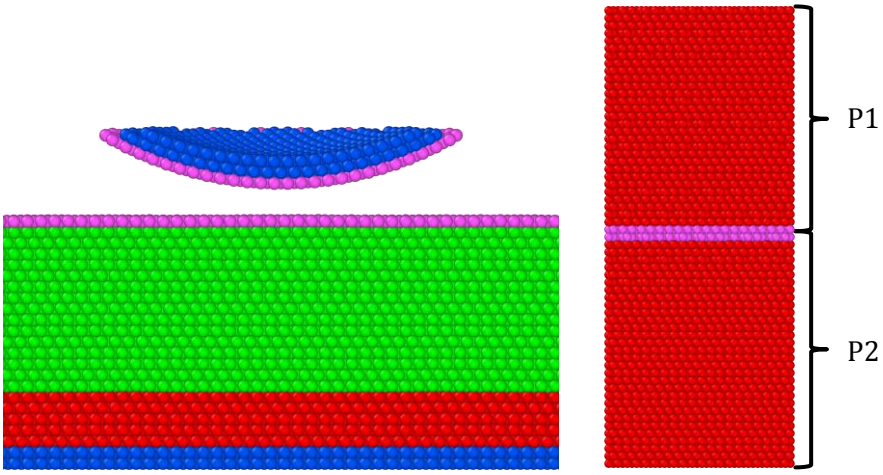

Figure B1 Side view of (left) the sphere-on-flat contacting system, and (right) the system used for calculating the work of adhesion. In both figures, the colors blue, red, green, and purple indicate the rigid, thermostatic, Newtonian, and surface layers (from bottom to top in the flat body). Also, P1 and P2 indicate the two different parts that were placed side by side as needed for the calculation of Γ (see Chapter 2).

B.3.1 Single asperity contact

The contact was simulated by moving an atomistic rigid spherical cap with a radius of $R = 100$ Å toward an atomically flat substrate with a constant velocity of 1 m/s. The initial clearance was set to 3σ. Following a relaxation time of 0.5 ns, the indenter was moved down (toward the substrate) for 9 Å, and 5 Å away from the substrate afterwards.

B.3.2 Work of adhesion

The method described in Chapter 2 was used for calculating the work of adhesion. It should be noted that, by setting the value of $c = 0$, a system is replicated for which the two sections are far from each other.

B.4 Results and discussion

B.4.1 Work of adhesion

Figure B2 shows the work of adhesion as a linear function of c. Aside from this value, the interacting energy between the surface layers of the contacting parts (E_{L1}) was also measured (the purple layers of Figure B1 (b)).

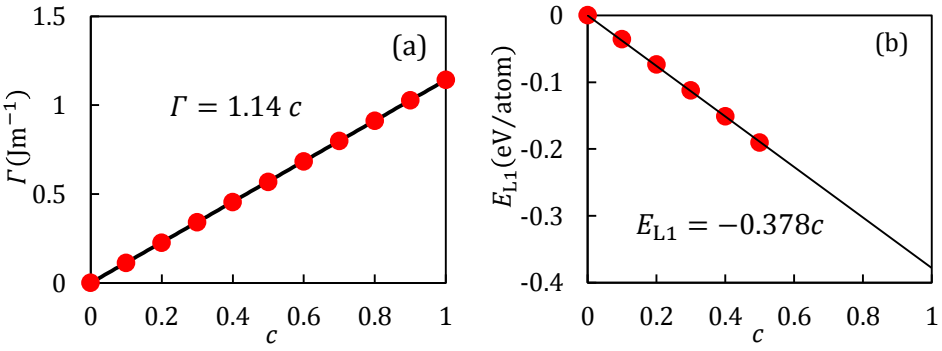

Figure B2 (a) The work of adhesion, and (b) the interacting energy per atom of the contacting surface layers.

B.4.2 Overview of the contact results

Figure B3 shows the $F - d$ curve of the contacting systems with $c = 0.5$ and $c = 0.6$. The results show that the contacting systems with $c \geq 0.6$ exhibit plastic deformation; therefore, the analyses were limited to the systems with $0.1 \leq c \leq 0.5$; these did not show any plastic deformation or adhesion hysteresis. Table B1 summarizes the measured values of the pull-off forces for each system. By calculating the values of $\chi = -F_{\mathrm{po}}/\pi R\Gamma$, it can be shown that the systems' contacting behavior tends to the JKR limit (see Figure B4).

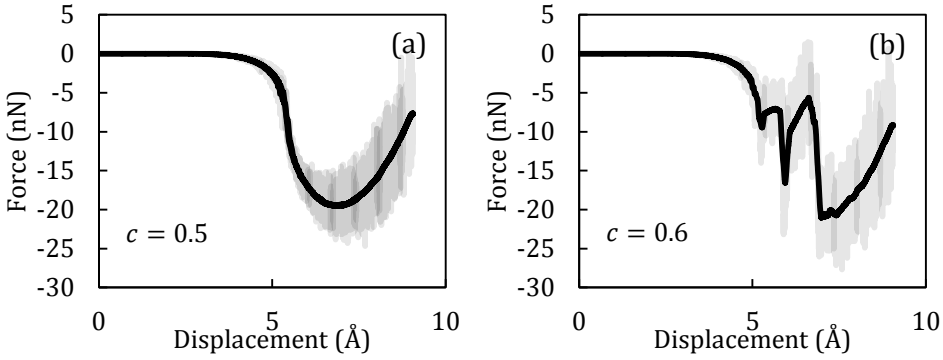

Figure B3 The normal applied force of the contacting systems with (a) $c = 0.5$ (for the whole course of loading and unloading), and (b) $c = 0.6$ (for the movement of the indenter toward the substrate) as functions of displacement. It should be noted that $d = 0$ Å points to the initial position of the indenter.

Table B1 The measured pull-off forces of the simulated contacting systems.

c	0.1	0.2	0.3	0.4	0.5
F_{po} (nN)	-3.98	-8.71	-12.64	-16.16	-19.56

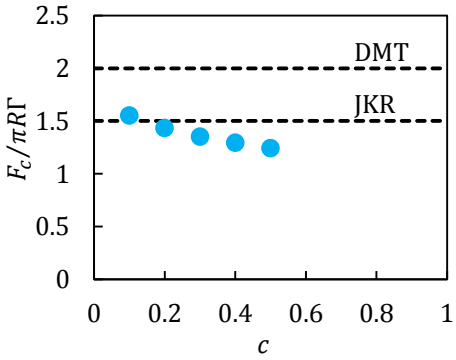

Figure B4 The comparison between the simulated systems with the limiting cases of JKR and DMT.

B.4.3 $F - d$ curves

The $F - d$ curves were calibrated by means of the JKR solution for $d_{F_\perp = F_{\mathrm{po}}}$ using (B.8). This method can calibrate the indentation depth, which is the same as the penetration depth in the continuum mechanics theories: these two parameters are the same, mainly because, in continuum mechanics theories, the contact is defined to start from the moment that the distance between two contacting bodies is zero. At the atomic scale, however, there is always a minimum distance between the centers of atoms. Therefore, these two parameters, namely indentation depth and penetration depth, should be distinguished: the indentation depth is related to the position of the indenter, and the penetration depth is related to the displacement of the deformed substrate. While this value might be inaccessible in experimental setups, it can be easily measured from the simulation.

Figure B5 shows the results for the indentation depths calibrated with the JKR solution for $d_{F_\perp = F_{\mathrm{po}}}$, the penetration depths measured directly from the simulations, and the JKR solutions calculated from (B.7). The results confirm the applicability of the proposed calibrating method. Moreover, the results show that, while the indentation depth deviates from the JKR solution for distances larger than $d_{F_\perp = F_{\mathrm{po}}}$, the behavior of the substrate, which was reflected in the penetration depth, was close to the JKR solution.

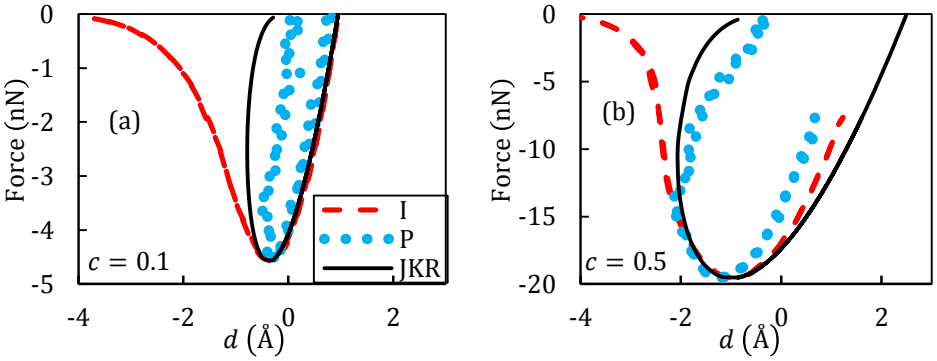

Figure B5 The force of the systems with (a) $c = 0.1$, and (b) $c = 0.5$ as functions of the calibrated indentation depth (I: red dashed lines) and penetration depth (P: blue dots). The continuous black lines represent the JKR solutions for the contacting systems. It should be noted that the penetration depth values were smoothened using a moving average filter with a span of 5% of the data points. Also note that the force axes ranges are different.

B.4.4 The radius of the contact area

In order to calculate the contact radius, the contact area should first be estimated, which can be done with, either, method **B** (counting the contacting atoms), or method **C** (measuring the contact energy), discussed in detail in Chapter 3. It should be noted that the projection of the non-contacting atoms (method **A**) would be inapplicable, due to the limited changes in the potential energy of the contacting atoms. Also, in both methods, the number of the contacting atoms and the contact area were translated via the contact area of an individual calcium atom, which is $A_a \cong 12.19$ Å^2 (see Chapter 4).

In order to use method **B**, first, a contact distance d_c should be defined for identifying the contacting atoms. Therefore, as the first step, d_c needs to be defined and calibrated. This can be done using the JKR theory, or the contact energy.

B.4.4.1 Method B1: calibration of the contact distance using the JKR theory

The value of d_c can be calibrated by comparing the simulation results with the JKR theory at pull-off, where the contact radius can be obtained from (B.5). Then, the contact area can be calculated as $A_{\mathrm{JKR}} = \pi r_{\mathrm{JKR}}^2$. Dividing this value by A_a, the reference number of contacting atoms at the pull-off ($N_{ca,\mathrm{B1}}$) can be estimated. Comparing this value with the simulation results at the pull-off, the contact distance can be defined such that the number of the contacting atoms matches the calibrating value of $N_{ca,\mathrm{JKR}}$.

B.4.4.2 Method B2: calibration of the contact distance using the contact energy

The calibration of d_c at the pull-off can be done by considering the interacting energy of the surface atoms of the contacting systems ($E_{\mathrm{L1,C}}$), which was calculated from surface layer (purple) atoms in Figure B1. The reference value of $N_{ca,E}$ would be $N_{ca,\mathrm{B2}} = E_{\mathrm{L1,C}} \times E_{\mathrm{L1}}$ at the pull-off, withE_{L1} reported in Figure B2(b). The rest of the procedure would be the same as described in section B.4.4.1.

B.4.4.3 Method C: measuring the contact radius using the contact energy

This method can be directly applied via $N_{ca,\mathrm{C}} = E_{\mathrm{L1,C}} \times E_{\mathrm{L1}}$ through all the simulation, and not only at the pull-off.

B.4.4.4 Comparison between the utilized methods

The results of the three described methods are shown in Figure B6. These show that, by calibrating the contact distance with the JKR solution at the pull-off, the system can be well described by the JKR theory for contact above the pull-off. This stability was investigated, and reported below; however, first, it is interesting to compare the results of method B1 with methods B2 and C. As Figure B6 (a) shows, the JKR theory underestimated the contact area for the whole range of the contact; however, Figure B6 (b) shows that, as c increases, the contact area tends toward the JKR solution. When analyzing all systems, it was found the simulation results were in a good agreement with the JKR solution for $0.3 \leq c \leq 0.5$.

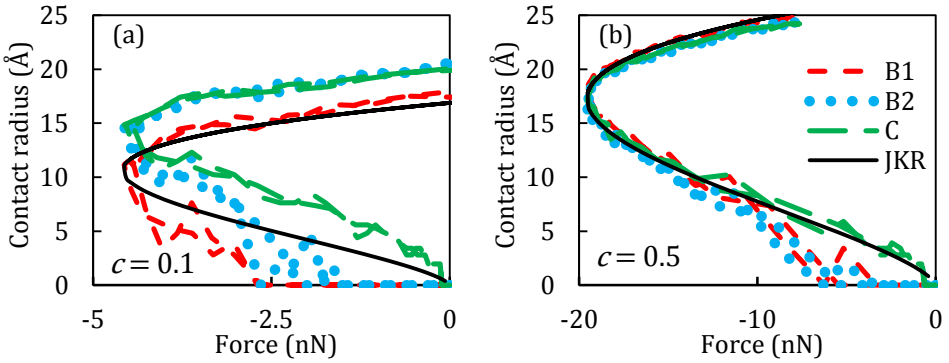

Figure B6 The calculated contact radii for the systems with (a) $c = 0.1$, and (b) $c = 0.5$ using the three described methods, in comparison to the JKR solution. Note that the force axes ranges are different.

Another important result, presented in Figure B6, is the difference between the contact radius for contact beyond the pull-off: methods B1 and B2 measured contact radii of zero for the initial/ending stages of the contact, while method C and the JKR solution yield non-zero contact radii for any non-

zero force. Considering method C to be the correct solution for the simulated systems, the contact distance was estimated for the whole simulation using the reference number of contacting atoms $N_{ca,C}$. The results for two of the systems with $c = 0.1$ and $c = 0.5$ are shown in Figure B7. As the results indicate, the contact distance changes for the initial/ending stages of the contact, i.e. the contact beyond the pull-off. The contact distance, however, would be constant away from the pull-in/pull-off stages. This indicates that the pull-off is an appropriate position for the calibration of the contact distance, because the value of d_c would not change for larger normal loads. This behavior is true whether the calibration was done using the JKR theory (method B1), or the contact energy (method B2). This is the reason for the stability of the simulation results with the JKR solution.

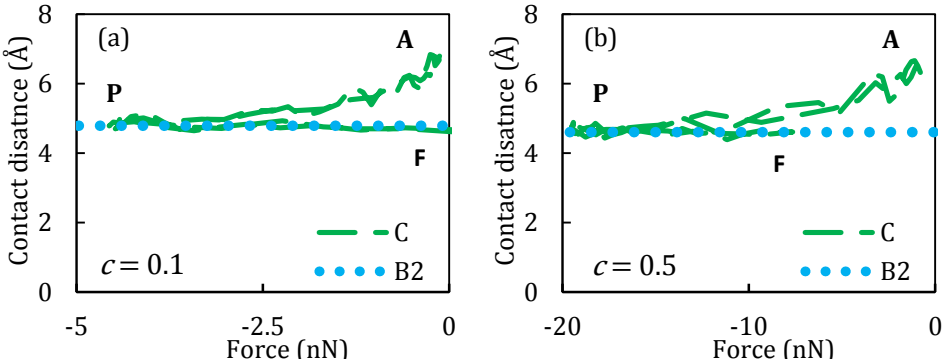

Figure B7 The calculated contact distances for the systems with (a) $c = 0.1$, and (b) $c = 0.5$ using the reference number of contacting atoms measured from method C ($N_{ca,C}$). Point **A** indicates the inception of contact. Then, the force decreases due to the adhesion, until the system reaches point **P**. Following this point, the repulsive force results in an increase in the total force, up to point **F** for the simulated system. The results show that the contact distance does not change while the system is between points **P** and **F**.

Appendix C. Contact pressure dependence on the interacting potential*

The pressure distribution of a contact between a rigid indenter and a deformable substrate depends on the applied interacting potential energy. In Chapter 4, the non-adhesive interactions were modelled by applying the non-adhesive part of the LJ potential; however, this was not the only solution. One can model short-range repulsion via the standard LJ potential, by cutting the potential at its minimum, and adding a constant to assure that the interacting force and energy go smoothly to zero at the cutoff. Figure C1 shows the contact pressure distribution for two cases of interacting potentials. Moreover, the interacting potential energy affects the indenter's responses; these effects are summarized in Table C1 and Figure C2.

The results show that, as the interacting potential energy approximates a hard-wall interaction, the fitted values of E^* increase to the bulk value of $E^* = 28.57$ GPa with a higher rate; however, for larger indentation depths, i.e. $d > 4$ Å in this study, the indenters' responses were found to be very similar, and independent from the interacting potential energy.

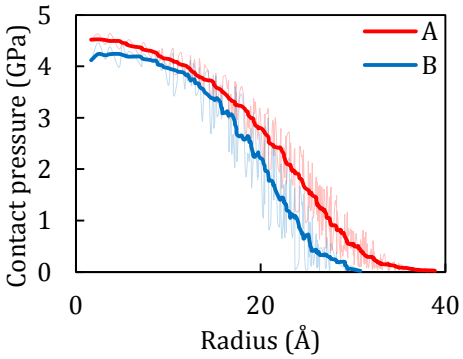

Figure C1 The interfacial contact pressure distribution between a rigid indenter of $R = 100$ Å and a deformable body. The non-adhesive contact was modeled with (A) the repulsion part of the LJ, and (B) cutting and shifting the LJ at its minimum.

* This is an appendix to Chapter 4.

Table C1 The values of the contact pressure threshold (P_c), contact distance (d_c), and the corrective shifts of displacement (δ_d) and force (δ_F)

Case	P_c (GPa)	d_c (Å)	δ_d (Å)	δ_F (nN)
A	1.335	4.964	5.721	0.620
B	1.190	4.826	6.786	0.002

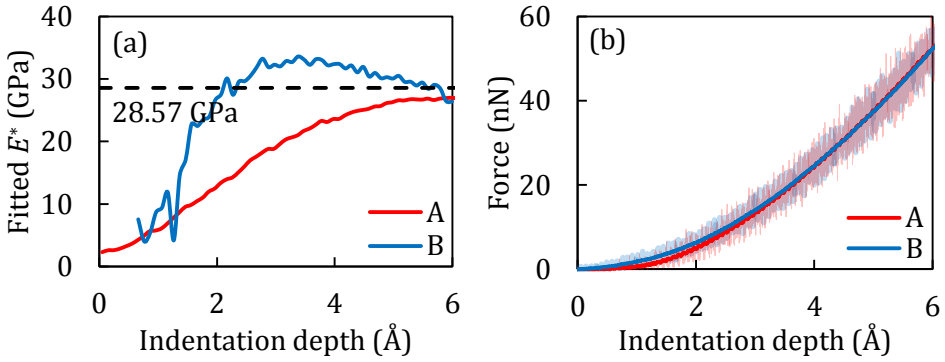

Figure C2 (a) The fitted values of E^*, and (b) the force-indentation depth curves for cases A and B.

Appendix D. Contact-induced stress fields*

Applying periodic boundary conditions (PBCs) along the desired directions is a classical method in MD simulations used to avoid the edges imposed by the finite size of the simulated system. In some systems, however, such as the ones investigated in chapter 4, PBCs are not applicable in the directions normal to a free surface. Consequently, the system behavior, including its mechanical response, could be affected by the finite system size in the directions where PBCs are not applied.

In the study of Chapter 4, an atomistic fixed layer providing the necessary mechanical support to the deformable bodies was used along the plane parallel to the free surface. As a result, the mechanical response of the systems would be affected by that fixed layer if the stress fields crossed the deformable body and reached the fixed layer. Allowing for this behavior could be relevant for thin layers, but not for bulk materials as was intended in the study. In order to remove this boundary effect, one may simulate the system using Green's function MD (GFMD) [11], smartblock MD [12], or by coupling MD with other techniques such as the finite element method (FEM), e.g. via the Atoms-to-Continuum package of LAMMPS; given sufficient computational resources, it is also possible to simulate an extremely large system using classical MD [122]. In this work, classical MD was used, and the results were collected up to the point before which the stress fields were affected by the fixed layer. This condition was tested through the calculation of the contact influenced stress values (CS) by subtracting the stress values of each atom at the end of the equilibration process (S_{eq}) from their corresponding value at each time step (S_t), i.e. $CS_t = S_t - S_{\mathrm{eq}}$, where CS_t indicates the values of CS at time step t. Then, the system was meshed along one of the lateral axes, and the maximum values of CS were collected. By examining these data, it was possible to identify the instances at which the stress fields reached the fixed layers. Table D1 shows the stress fields of a number of the contacting systems, at the last step of data extraction.

* This is an appendix to Chapter 4.

Table D1 The representation of the atomic structures of the contacting systems (normal to the x axis), and their contact-induced stress fields. The atoms are represented in the left column as circles with different colors: fixed (blue), thermostatic (red), non-constrained (green), and the indenter as white. The right column shows the projection of the maximum values of the contact induced stress (CS) values on a plane normal to the x axis: dark blue indicates the minimum of value of 0, and dark red indicates the maximum of the values, which was 0.9 GPa, 8.5 GPa, and 10.2 GPa, for the cases of single asperity, GW rough surface, and random rough surface, respectively.

	Atomic structure	Contact induced stress field
Single asperity (1000 Å)	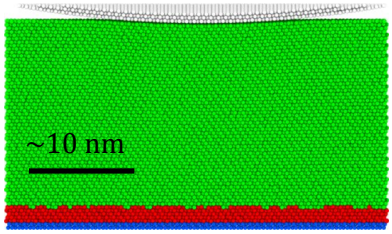	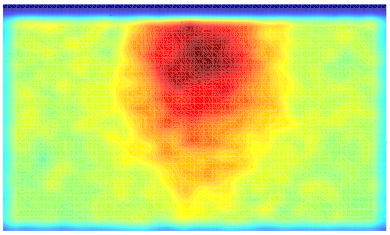
GW-type rough surface	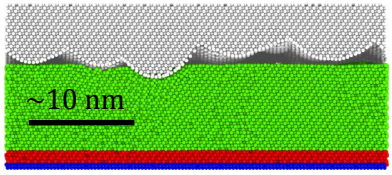	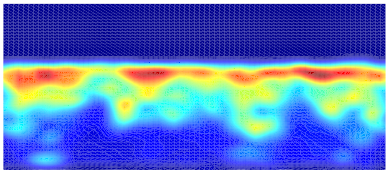
Randomly rough surface	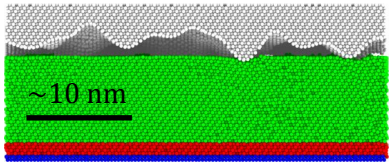	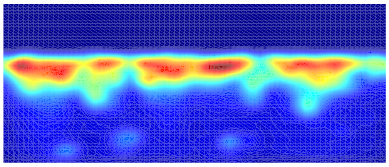

Appendix E. The exponent of PSD*

For self-affine fractal profiles, the slope of the PSD would be [123]

$$\beta = -(2H + D_S), \tag{E.1}$$

where H is the Hurst exponent, and D_S is the spatial dimension of the projected fractal, i.e. $D_S = 2$ for a fractal surface and $D_S = 1$ for a fractal line. The Hurst exponent describes the raggedness of the profile, with a lower value leading to a rougher profile. The value of the Hurst exponent is bounded as $0 < H < 1$. Considering the range of the Hurst exponent, one may conclude that $\beta \in (-2, -4)$ for a fractal surface. The definition of the PSD in the form of (5.2), however, does not apply such a restriction on the values of β. On the other hand, if β exceeds the abovementioned limitation, the value of H would vary outside the range of (0,1); therefore, H loses its general meaning of the Hurst exponent [124]. This is the main reason why the PSD exponent is not expressed in terms of H or D_S in the current study.

* This is an appendix to Chapter 5.

Appendix F. The spectral moments of PSD*

The spectral moments of the PSD can be calculated from [125]

$$m_n = A_n \int_0^{+\infty} q^{1+n}\, C(q) \mathrm{d}q, \tag{F.1}$$

with

$$A_n = \int_0^{2\pi} (\cos\omega)^n \, d\omega. \tag{F.2}$$

For $n = 0, 2$, and 4, A_n equals 2π, π, and $3\pi/4$, respectively. Considering the definition of $C(q)$ for $q_\mathrm{L} \le q \le q_\mathrm{S}$ based on (5.2), (F.1) can be solved and reformulated as follows:

$$m_n = A_n C_0 q_r^{2+n} I_n, \tag{F.3}$$

with

$$I_n = \frac{1 - M_\mathrm{L}^{2+n}}{2+n} - \frac{1 - M_\mathrm{S}^{2+n+\beta}}{2+n+\beta}, \tag{F.4}$$

where $M_\mathrm{L} = q_\mathrm{L}/q_\mathrm{r}$, and $M_\mathrm{S} = q_\mathrm{S}/q_\mathrm{r}$. These formulae are important for the generation of rough surfaces; a rough surface can be generated by solving (5.1), where the values of $h(\mathbf{q})$ should be converted from the values of $C(\mathbf{q})$ in the form of (5.2). In order to solve (5.2), the values of q_L, q_r, q_S, β, and C_0 need to be defined beforehand. The values of these variables can be assigned arbitrarily, provided they do not violate the conditions of $q_\mathrm{L} < q_\mathrm{r} < q_\mathrm{S}, \beta < 0$, and $C_0 > 0$. The value of C_0, however, can be defined such that the generated surface will possess a specific spectral moment. Considering that $m_0 = \sigma_\mathrm{rms}^2$ [104], and $m_2 = \frac{1}{2}\overline{g}^2$ [126], the parameter C_0 can be defined as $C_0 = \sigma_\mathrm{rms}^2 (A_0 I_0 q_\mathrm{r}^2)^{-1}$ and $C_0 = \frac{1}{2}\overline{g}^2 (A_2 I_2 q_\mathrm{r}^4)^{-1}$, respectively. In order to generate a surface with given values of σ_rms and $\overline{g}$, however, C_0 will need to have a unique solution, resulting in a distinctive roll-off wavenumber of $q_\mathrm{r} = (\overline{g}/\sigma_\mathrm{rms})\sqrt{I_0/I_2}$, which cannot be solved analytically. Therefore, in this study, C_0 was estimated based on the PSD's zeroth moment, in order to generate rough surfaces with a specific value of σ_rms.

---

* This is an appendix to Chapter 5.

Appendix G. The mean gradient for a limiting case of nominally flat rough {100} planes in an fcc structure*

For an atomistic nominally flat rough surface, a limiting case would be a saw-tooth rough surface, with every other atom removed along each of the lateral directions. In the surface analysis methods adapted in this work, the atomistic rough surfaces were projected on a uniformly gridded plane. The estimated surface for the abovementioned limiting case is shown in Figure G1. It can be shown that the local gradient on each grid point is $\sqrt{2}$. Consequently, the mean gradient of this limiting case would be $\sqrt{2}$.

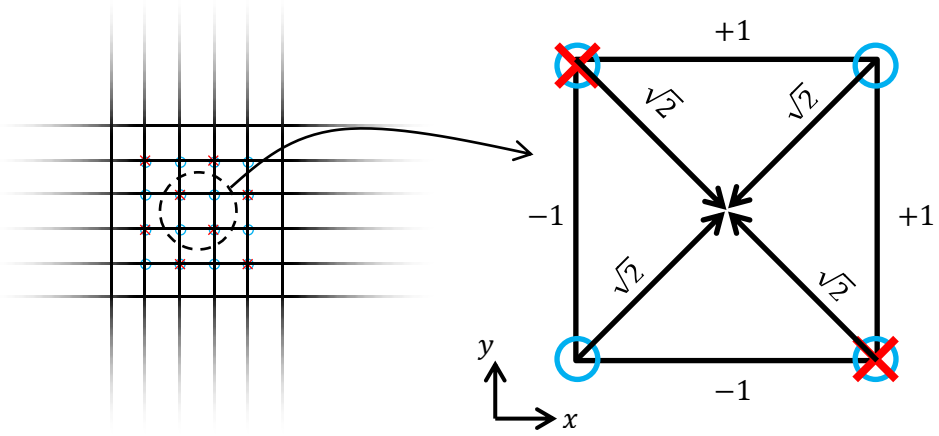

Figure G1. (Left) The uniformly gridded plane for the limiting case of an atomistic nominally flat rough surface along the {001} planes of an fcc structure, where every other atom is removed along each direction of x and y. Note that no grid was assigned for the faced-centered atoms in the surface analysis of the current work. (Right) A selected grid of the saw-tooth rough surface. The numbers on the edges indicate the calculated slopes along the x and y axes. The numbers on the arrows indicate the local gradients at each grid point.

* This is an appendix to Chapter 5.

Appendix H. Roughness of molten gold due to capillary waves*

The interface undulation between any two fluids can be described by capillary wave theory; see [127] for a short review, and [128] for a deep discussion on the applicability of this theory in MD simulations. While this theory is most relevant for interfaces between fluids, one may argue that it is still applicable for the cases studied in this research, i.e. free surfaces. In capillary wave theory, the thermally excited height fluctuation spectrum $h_{\mathrm{CW}}(q)$ of an isotropic crystallographic surface can be expressed by:

$$\langle |h_{\mathrm{CW}}(q)|^2 \rangle = \frac{k_B T}{\gamma L^2} q^{-2}, \tag{H.1}$$

where k_B is the Boltzmann constant, and γ is the surface energy of the free surface expressed in the dimensions of energy over area. Considering the relation $C(q) = (L/2\pi)^2 \langle |h(q)|^2 \rangle$ (see section 5.2), the power spectral distribution of the thermally agitated capillary waves can be written as

$$C_{\mathrm{CW}}(q) = \frac{1}{4\pi^2} \frac{k_B T}{\gamma} q^{-2}. \tag{H.2}$$

The RMS roughness of the thermally agitated capillary waves can be obtained from m_0 (see Appendix F) to be

$$\sigma_{\mathrm{rms,CW}} = \left(\frac{1}{2\pi} \frac{k_B T}{\gamma} \ln\left(\frac{L}{\delta}\right) \right)^{0.5}. \tag{H.3}$$

Therefore, the total RMS roughness of the surface can be estimated as

$$\sigma_{\mathrm{rms}} = \sqrt{\sigma_{\mathrm{rms,0}}^2 + \sigma_{\mathrm{rms,CW}}^2}. \tag{H.4}$$

Considering (H.3) and the proportionality of $\sigma_{\mathrm{rms,CW}} \propto \sqrt{T}$, one may argue that the roughness would be higher as the equilibration temperature increases. This would be in accord with the reported results in section 5.5.5.

As the temperature rises, the material softens and cannot withstand the local stresses due to the initial surface roughness, as is particularly visible for the case of $T = T_{\mathrm{m}}$; however, the generated capillary waves do not allow the

* This is an appendix to Chapter 5.

surface to have a roughness parameter of $\rho = 0$. In order to estimate the roughness parameter of the free surface at the melting point, one can assume that the surface roughness is solely due to capillary waves. Therefore, the RMS roughness can be calculated via (H.3). Moreover, the mean gradient can be calculated from m_2 (see Appendix F) to be

$$\overline{g}_{\mathrm{CW}} = \left(\pi \frac{k_B T}{\gamma} (\delta^{-2} - L^{-2}) \right)^{0.5}. \tag{H.5}$$

Furthermore, the autocovariance function of the power spectral distribution in the form of (H.2) can be calculated using the zero-order Hankel transform of $C(q)$, which results in

$$\mathrm{var}(r) = \frac{1}{2\pi} \int_{q_L}^{qs} C(q) J_0(qr) q dq, \tag{H.6}$$

where J_0 is the zero-order Bessel function of the first kind. Then, the autocorrelation function can be calculated as $R(r) = \mathrm{var}(r)/\mathrm{var}(\delta)$.

For the simulated material, the melting point and the (100) surface energy are 1281 K and 1.225 J/m^2, respectively [91]. Inserting these values into (H.3), (H.5), and (H.6), yields values for the RMS roughness, mean gradient, and lateral correlation length of $\sigma_{\mathrm{rms,CW}} = 0.6\mathrm{a}_0$, $\overline{g}_{\mathrm{CW}} = 0.5$, and $\zeta_{\mathrm{CW}} = 4.7\mathrm{a}_0$, respectively. It should be noted that the lateral correlation length was estimated from the numerical solution of (H.6) (see Figure H1). Thus, the roughness parameter of the molten system can be calculated as $\rho_{\mathrm{CW}} \cong 0.07$, which is very close to the measured value of $\rho \cong 0.05$ for the system at the melting point (see section 5.5.5).

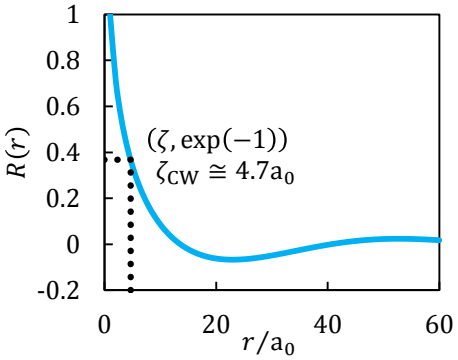

Figure H1 The autocorrelation function of the thermally agitated capillary waves on a free surface of a gold substrate at the melting point.

Supplementary Materials for Chapter 5

S1. The normalized radial distribution function of the NPT ensemble of the simulated gold

The normalized radial distribution function, $g(r)$, of the simulated gold [91] was calculated for two purposes: one was to determine the contact area of a single atom: it is shown that the position of the first peak of a $g(r)$ plot (d_{fp}) can be considered as the atomic diameter d_a. Moreover, the $g(r)$ plot was used for deciding on the thickness of the rough blocks: in an infinite system $g(r) \to 1$ as $r \to \infty$; therefore, a distance where $g(r) \to 1$ can be assumed to be large enough to resemble $r \to \infty$. Following the method described in Chapter 3, a system of gold with a size of L^3, with $L \cong 15\mathrm{a}_0$, was simulated by applying zero external pressure at 300 K, and the required $g(r)$ plot was calculated. As shown in Figure S1, the atomic diameter was estimated to be $d_a = 2.88$ Å. Moreover, the results show that a distance of $\sim 10\mathrm{a}_0$ was large enough for its $g(r)$ to reach the steady-state value of 1.

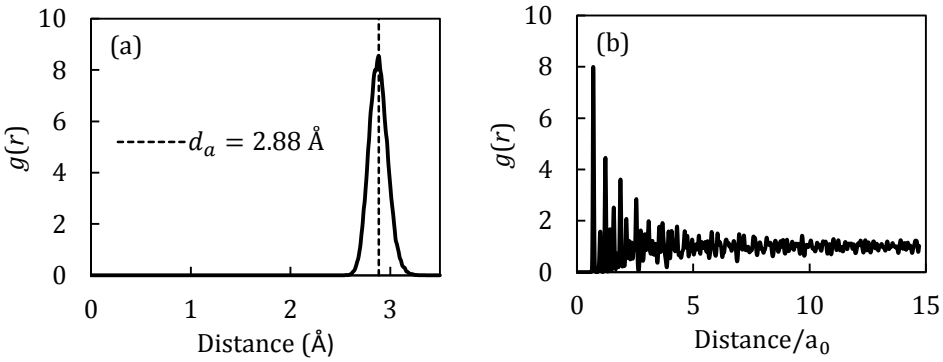

Figure S1 The $g(r)$ plot of the NPT ensemble for the simulate gold at 300 K, under zero external pressure. The difference between (a) and (b) is on their range of distances.

S2. The distribution of internal von Mises stress

In order to analyze the internal stress of the studied systems, first, an NPT ensemble was simulated and the distribution of internal stress values was analyzed: this was done by the "compute stress/atom" command in LAMMPS, which computes the symmetric stress tensor for each atom. Using the provided stress tensor and the estimated contact area of an individual atom, $A_a \cong 6.5$ Å^2 (see S1), the von Mises stress was calculated. In the next step, two of the systems, namely $q3\_\beta5$ and $q1\_\beta5$, which were the roughest and smoothest studied surfaces, respectively, were selected for stress analysis. The von Mises stress values were calculated in the same way as described previously. Figure S2 shows the normalized probability distribution function of the systems' internal von Mises stress. As the results show, the stress distribution of the studied rough blocks deviated from the NPT ensemble on the high-stress tail. This is directly related to the two free surfaces of the simulated blocks: one flat surface at the bottom, and one rough surface at the top; however, the rough surface did not result in any distinctive accumulated stress in the PDFs.

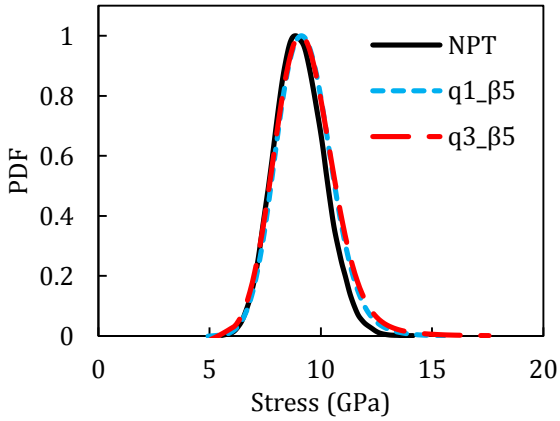

Figure S2 The normalized probability distribution function of the systems' internal von Mises stress. It should be noted that the wide range of the internal stress values are due to the thermal fluctuations of atoms; the range would be narrower at lower temperatures.

S3. Supplementary figures for the systems with z = [100] at 300 K

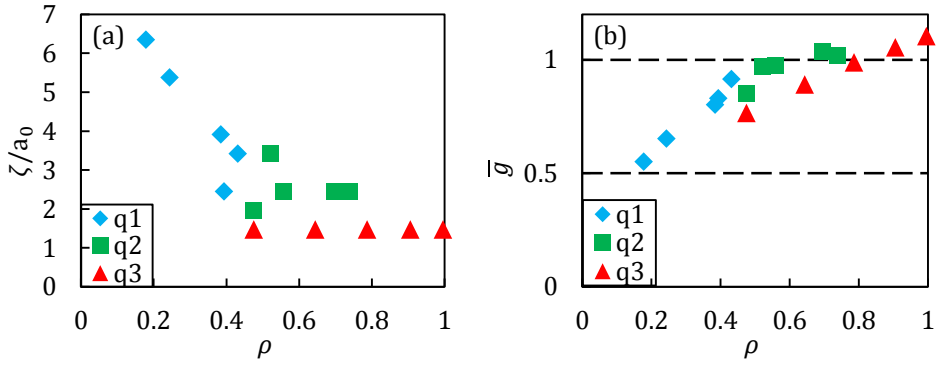

Figure S3 (a) The lateral correlation length normalized by the lattice constant, and (b) the RMS gradient as functions of the roughness parameter ρ.

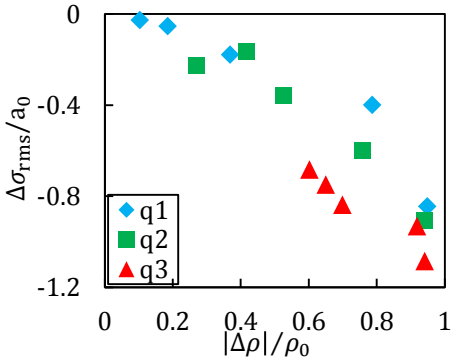

Figure S4 The changes of the RMS roughness due to the equilibration process.

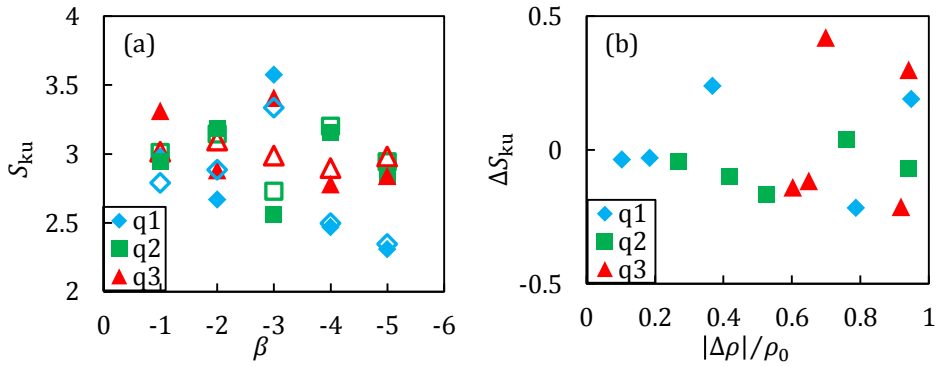

Figure S5 (a) The values of kurtosis of the original (void symbols) and equilibrated (filled symbols) surface roughness, and (b) the changes of kurtosis due to the equilibration process.

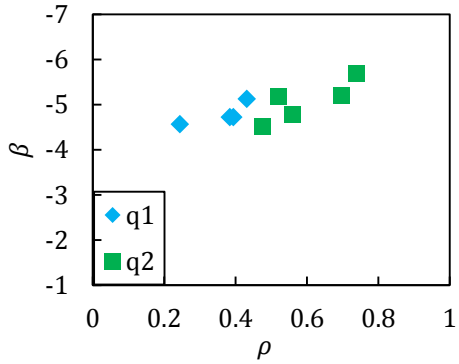

Figure S6 The PSD exponents of the equilibrated $q1$ and $q2$ substrates as a function of the roughness parameter ρ. The maximum value of β was obtained to be -4.5. Note that β decreases from the bottom to the top of the vertical axis.

S4. Supplementary figures for the crystal orientation effect

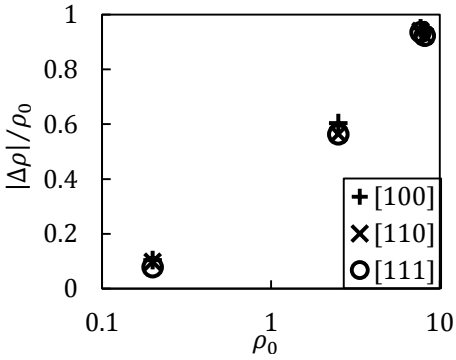

Figure S7 The relative changes of roughness parameter ρ as a function of ρ_0 for the systems with different crystallographic orientations.

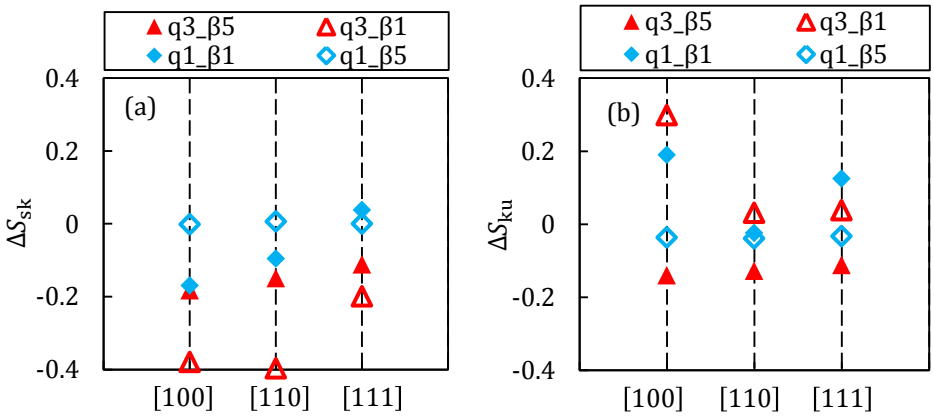

Figure S8 The changes of (a) skewness, and (b) kurtosis for the systems with different crystallographic orientations.

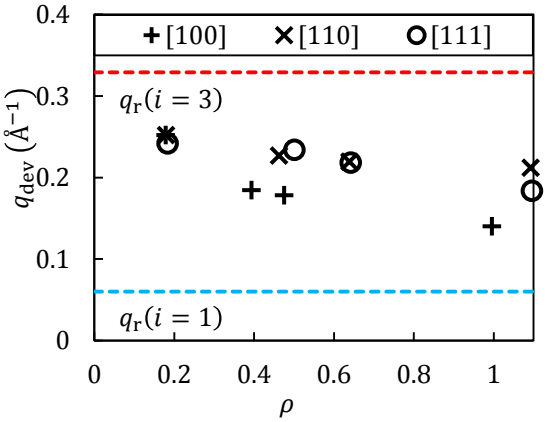

Figure S9 The estimated values of q_{dev} for the system with different crystallographic orientations.

References

[1] N. Koumura, R.W.J. Zijlstra, R.A. van Delden, N. Harada, B.L. Feringa, Light-driven monodirectional molecular rotor, Nature, 401 (1999) 152-155.

[2] R.W. Carpick, N. Agrait, D.F. Ogletree, M. Salmeron, Measurement of interfacial shear (friction) with an ultrahigh vacuum atomic force microscope, Journal of Vacuum Science & Technology B, 14 (1996) 1289-1295.

[3] B. Luan, M.O. Robbins, The breakdown of continuum models for mechanical contacts, Nature, 435 (2005) 929-932.

[4] Y. Mo, K.T. Turner, I. Szlufarska, Friction laws at the nanoscale, Nature, 457 (2009) 1116-1119.

[5] Y. Mo, I. Szlufarska, Roughness picture of friction in dry nanoscale contacts, Physical Review B, 81 (2010) 035405.

[6] S. Cheng, M.O. Robbins, Defining contact at the atomic scale, Tribology Letters, 39 (2010) 329-348.

[7] J.N. Israelachvili, 18-Friction and lubrication forces, in: Intermolecular and surface forces (Third Edition), Academic Press, San Diego, (2011) 469-499.

[8] P. Spijker, G. Anciaux, J.-F. Molinari, The effect of loading on surface roughness at the atomistic level, Computational Mechanics, 50 (2012) 273-283.

[9] S. Eder, A. Vernes, G. Vorlaufer, G. Betz, Molecular dynamics simulations of mixed lubrication with smooth particle post-processing, Journal of Physics-Condensed Matter, 23 (2011) 175004.

[10] E. Gnecco, E. Meyer, Fundamentals of Friction and Wear on the Nanoscale, Springer, (2015).

[11] C. Campñá, M.H. Müser, Practical Green's function approach to the simulation of elastic semi-infinite solids, Physical Review B, 74 (2006).

[12] C. Yang, U. Tartaglino, B.N.J. Persson, A multiscale molecular dynamics approach to contact mechanics, European Physical Journal E, 19 (2006) 47-58.

[13] I. Szlufarska, M. Chandross, R.W. Carpick, Recent advances in single-asperity nanotribology, Journal of Physics D: Applied Physics, 41 (2008) 123001.

[14] K.L. Johnson, K. Kendall, A.D. Roberts, Surface energy and the contact of elastic solids, Proceedings of the Royal Society of London. A. Mathematical and Physical Sciences, 324 (1971) 301-313.

[15] B.V. Derjaguin, V.M. Muller, Y.P. Toporov, Effect of contact deformations

on the adhesion of particles, 53 (1975) 314-326.
[16] S.K. Roy Chowdhury, H.M. Pollock, Adhesion between metal surfaces: The effect of surface roughness, Wear, 66 (1981) 307-321.
[17] M.D. Pashley, J.B. Pethica, D. Tabor, Adhesion and micromechanical properties of metal surfaces, Wear, 100 (1984) 7-31.
[18] N. Agraït, G. Rubio, S. Vieira, Plastic Deformation in Nanometer Scale Contacts, Langmuir, 12 (1996) 4505-4509.
[19] Y. Kadin, Y. Kligerman, I. Etsion, Jump-in induced plastic yield onset of approaching microcontacts in the presence of adhesion, Journal of Applied Physics, 103 (2008) 013513.
[20] L. Kogut, I. Etsion, Adhesion in elastic–plastic spherical microcontact, Journal of Colloid and Interface Science, 261 (2003) 372-378.
[21] J. Song, D.J. Srolovitz, Adhesion effects in material transfer in mechanical contacts, Acta Materialia, 54 (2006) 5305-5312.
[22] F.A. Gilabert, M.A.S. Quintanilla, A. Castellanos, J.M. Valverde, Adhesive elastic plastic contact: theory and numerical simulation, ZAMM - Journal of Applied Mathematics and Mechanics / Zeitschrift für Angewandte Mathematik und Mechanik, 87 (2007) 128-138.
[23] B. Luan, M.O. Robbins, Contact of single asperities with varying adhesion: Comparing continuum mechanics to atomistic simulations, Physical Review E, 74 (2006) 026111.
[24] H. Hertz, Über die Berührung fester elastischer Körper (On the contact of rigid elastic solids), Journal für die reine und angewandte Mathematik, 92 (1881) 156-171.
[25] K.L. Johnson, Contact mechanics, Cambridge University Press, (1987).
[26] R.S. Bradley, LXXIX. The cohesive force between solid surfaces and the surface energy of solids, The London, Edinburgh, and Dublin Philosophical Magazine and Journal of Science, 13 (1932) 853-862.
[27] V.M. Muller, B.V. Derjaguin, Y.P. Toporov, On two methods of calculation of the force of sticking of an elastic sphere to a rigid plane, Colloids and Surfaces, 7 (1983) 251-259.
[28] D. Maugis, Adhesion of spheres: the JKR-DMT transition using a dugdale model, 150 (1992) 243-269.
[29] D. Tabor, Surface forces and surface interactions, International Conference on Colloids and Surfaces, 58 (1977) 2-13.
[30] B.V. Derjaguin, V.M. Muller, Y.P. Toporov, On the role of molecular forces in contact deformations (critical remarks concerning Dr. Tabor's report), Journal of Colloid and Interface Science, 67 (1978) 378-379.
[31] D. Tabor, On the role of molecular forces in contact deformations (Critical remarks concerning Dr. Tabor's report), Journal of Colloid and

Interface Science, 67 (1978) 380.
[32] B. Derjaguin, V. Muller, Y. Toporov, On different approaches to the contact mechanics, Journal of Colloid and Interface Science, 73 (1980) 293.
[33] D. Tabor, Role of molecular forces in contact deformations, Journal of Colloid and Interface Science, 73 (1980) 294.
[34] V.M. Muller, V.S. Yushchenko, B.V. Derjaguin, On the influence of molecular forces on the deformation of an elastic sphere and its sticking to a rigid plane, Journal of Colloid and Interface Science, 77 (1980) 91-101.
[35] J.E. Jones, On the determination of molecular fields. II. from the equation of state of a gas, Proceedings of the Royal Society of London. Series A, 106 (1924) 463-477.
[36] J.J. Vlassak, M. Ciavarella, J.R. Barber, X. Wang, The indentation modulus of elastically anisotropic materials for indenters of arbitrary shape, Journal of the Mechanics and Physics of Solids, 51 (2003) 1701-1721.
[37] S. Plimpton, Fast parallel algorithms for short-range molecular dynamics, Journal of Computational Physics, 117 (1995) 1-19.
[38] W.C. Swope, H.C. Andersen, P.H. Berens, K.R. Wilson, A computer simulation method for the calculation of equilibrium constants for the formation of physical clusters of molecules: Application to small water clusters, The Journal of chemical physics, 76 (1982) 637-649.
[39] H.J.C. Berendsen, J.P.M. Postma, W.F. van Gunsteren, A. DiNola, J.R. Haak, Molecular dynamics with coupling to an external bath, The Journal of chemical physics, 81 (1984) 3684-3690.
[40] A. Stukowski, Visualization and analysis of atomistic simulation data with OVITO–the Open Visualization Tool, Modelling and Simulation in Materials Science and Engineering, 18 (2010) 015012.
[41] A. Stukowski, K. Albe, Extracting dislocations and non-dislocation crystal defects from atomistic simulation data, Modelling and Simulation in Materials Science and Engineering, 18 (2010) 085001.
[42] A. Stukowski, V.V. Bulatov, A. Arsenlis, Automated identification and indexing of dislocations in crystal interfaces, Modelling and Simulation in Materials Science and Engineering, 20 (2012) 085007.
[43] A. Stukowski, Structure identification methods for atomistic simulations of crystalline materials, Modelling and Simulation in Materials Science and Engineering, 20 (2012) 045021.
[44] A. Stukowski, Computational analysis methods in atomistic modeling of crystals, JOM, 66 (2014) 399-407.
[45] X.W. Zhou, R.A. Johnson, H.N.G. Wadley, Misfit-energy-increasing

dislocations in vapor-deposited CoFe/NiFe multilayers, Physical Review B, 69 (2004) 144113.
[46] R. Hill, The elastic behaviour of a crystalline aggregate, Proceedings of the Physical Society of London Section A, 65 (1952) 349-355.
[47] D.J. Oliver, W. Paul, M.E. Ouali, T. Hagedorn, Y. Miyahara, Y. Qi, P.H. Grütter, One-to-one spatially matched experiment and atomistic simulations of nanometre-scale indentation, Nanotechnology, 25 (2014) 025701.
[48] C.L. Kelchner, S.J. Plimpton, J.C. Hamilton, Dislocation nucleation and defect structure during surface indentation, Physical Review B, 58 (1998) 11085-11088.
[49] C.J. DaSilva, J.P. Rino, Atomistic simulation of the deformation mechanism during nanoindentation of gamma titanium aluminide, Computational Materials Science, 62 (2012) 1-5.
[50] J.N. Israelachvili, 10 - Unifying concepts in intermolecular and interparticle forces, in: Intermolecular and surface forces (Third Edition), Academic Press, San Diego, (2011) 191-204.
[51] K.E. Ryan, P.L. Keating, T.D.B. Jacobs, D.S. Grierson, K.T. Turner, R.W. Carpick, J.A. Harrison, Simulated adhesion between realistic hydrocarbon materials: effects of composition, roughness, and contact point, Langmuir, 30 (2014) 2028-2037.
[52] D. Hull, D.J. Bacon, Chapter 5 - Dislocations in Face-centered Cubic Metals, in: Introduction to Dislocations (Fifth Edition), Butterworth-Heinemann, Oxford, 2011, pp. 85-107.
[53] D. Rodney, R. Phillips, Structure and strength of dislocation junctions: An atomic level analysis, Physical Review Letters, 82 (1999) 1704-1707.
[54] V. Boyko, R. Garber, A. Kossevich, Reversible crystal plasticity, Springer Science & Business Media, (1997).
[55] W.C. Oliver, G.M. Pharr, Measurement of hardness and elastic modulus by instrumented indentation: Advances in understanding and refinements to methodology, Journal of Materials Research, 19 (2004) 3-20.
[56] E.T. Lilleodden, J.A. Zimmerman, S.M. Foiles, W.D. Nix, Atomistic simulations of elastic deformation and dislocation nucleation during nanoindentation, Journal of the Mechanics and Physics of Solids, 51 (2003) 901-920.
[57] A. Ukwatta, A. Achuthan, A molecular dynamics (MD) simulation study to investigate the role of existing dislocations on the incipient plasticity under nanoindentation, Computational Materials Science, 91 (2014) 329-338.

[58] F. Aqra, A. Ayyad, Surface energies of metals in both liquid and solid states, Applied Surface Science, 257 (2011) 6372-6379.
[59] D. François, A. Pineau, A. Zaoui, Mechanical behaviour of materials, Springer, (1998).
[60] K.L. Johnson, Mechanics of adhesion, Tribology International, 31 (1998) 413-418.
[61] F.P. Bowden, D. Tabor, The friction and lubrication of solids, Oxford University Press, London, (1964).
[62] L. Pei, S. Hyun, J.-F. Molinari, M.O. Robbins, Finite element modeling of elasto-plastic contact between rough surfaces, Journal of the Mechanics and Physics of Solids, 53 (2005) 2385-2409.
[63] M.T. Knippenberg, P.T. Mikulski, J.A. Harrison, Effects of tip geometry on interfacial contact forces, Modelling and Simulation in Materials Science and Engineering, 18 (2010).
[64] E.D. Reedy, Jr., Thin-coating contact mechanics with adhesion, Journal of Materials Research, 21 (2006) 2660-2668.
[65] S. Solhjoo, A.I. Vakis, Single asperity nanocontacts: comparison between molecular dynamics simulations and continuum mechanics models, Computational Materials Science, 99 (2015) 209-220.
[66] S. Solhjoo, A.I. Vakis, Molecular dynamics simulations of rough contact with fractal and statistical surface generation, in: ASME 2014 12th Biennial Conference on Engineering Systems Design and Analysis, American Society of Mechanical Engineers, (2014) V003T014A002.
[67] S. Wenner, Molecular dynamics simulations of nanoscale mechanical processes, MSc thesis, University of Oslo, Norway, (2010).
[68] W.S. Rasband, ImageJ, U. S. National Institutes of Health, Bethesda, Maryland, USA, 1997-2014. (http://imagej.nih.gov/ij)
[69] M.S. Daw, M.I. Baskes, Embedded-atom method - derivation and application to impurities, surfaces, and other defects in metals, Physical Review B, 29 (1984) 6443-6453.
[70] X. Zheng, H. Zhu, A.K. Tieu, B. Kosasih, Roughness and lubricant effect on 3d atomic asperity contact, Tribology Letters, 53 (2014) 215-223.
[71] Z. Shu, G.J. Davies, Calculation of the lennard-jones n-m potential-energy parameters for metals, Physica Status Solidi a-Applied Research, 78 (1983) 595-605.
[72] M. Waldman, A.T. Hagler, New combining rules for rare-gas van-der-Waals parameters, Journal of Computational Chemistry, 14 (1993) 1077-1084.
[73] C. Desgranges, J. Delhommelle, Evaluation of the grand-canonical partition function using expanded Wang-Landau simulations. III. Impact

of combining rules on mixtures properties, Journal of Chemical Physics, 140 (2014).
[74] J. Delhommelle, P. Millie, Inadequacy of the Lorentz-Berthelot combining rules for accurate predictions of equilibrium properties by molecular simulation, Molecular Physics, 99 (2001) 619-625.
[75] R.A. Johnson, Alloy models with the embedded-atom method, Physical Review B, 39 (1989) 12554-12559.
[76] W. Shinoda, M. Shiga, M. Mikami, Rapid estimation of elastic constants by molecular dynamics simulation under constant stress, Physical Review B, 69 (2004) 134103.
[77] M.K. Yeo, Y.H. Jang, Molecular dynamics simulation of a nanoscale sliding layer system, Wear, 269 (2010) 206-212.
[78] P. Spijker, G. Anciaux, J.-F. Molinari, Dry sliding contact between rough surfaces at the atomistic scale, Tribology Letters, 44 (2011) 279-285.
[79] X. Zheng, H. Zhu, A. Kiet Tieu, B. Kosasih, A molecular dynamics simulation of 3D rough lubricated contact, Tribology International, 67 (2013) 217-221.
[80] S. Solhjoo, A.I. Vakis, Normal contacts of lubricated fractal rough surfaces at the atomic scale, in: TriboUK 2015, Loughborough, England, (2015) 36.
[81] S. Solhjoo, A.I. Vakis, Lubricated normal and sliding contact of fractal rough surfaces at the atomic scale, in: The International Conference on Understanding and Controlling Nano and Mesoscale Friction (COSTnanoTribo), Istanbul, Turkey, (2015) 46.
[82] J.A. Greenwood, J.B.P. Williamson, Contact of nominally flat surfaces, Proceedings of the Royal Society of London.Series A.Mathematical and Physical Sciences, 295 (1966) 300-319.
[83] B.N.J. Persson, Elastoplastic contact between randomly rough surfaces, Physical Review Letters, 87 (2001).
[84] B.N.J. Persson, Theory of rubber friction and contact mechanics, The Journal of chemical physics, 115 (2001) 3840-3861.
[85] M.H. Müser, W.B. Dapp, The contact mechanics challenge: problem definition, arXiv (2015) 1512.02403.
[86] E. Gnecco, E. Meyer, Rough contacts, in: Elements of friction theory and nanotribology, Cambridge University Press, (2015) 75-89.
[87] V.A. Yastrebov, G. Anciaux, J.-F. Molinari, From infinitesimal to full contact between rough surfaces: Evolution of the contact area, International Journal of Solids and Structures, 52 (2015) 83-102.
[88] A.P. Rigazzi, The effects of roughness on the area of contact and on the elastostatic friction, PhD thesis, Università della Svizzera Italiana,

(2014).
[89] C. Yang, B.N.J. Persson, Molecular dynamics study of contact mechanics: Contact area and interfacial separation from small to full contact, Physical Review Letters, 100 (2008).
[90] S. Solhjoo, A. Simchi, H. Aashuri, Molecular dynamics simulation of melting, solidification and remelting processes of aluminum, Iranian Journal of Science and Technology-Transactions of Mechanical Engineering, 36 (2012) 13-23.
[91] H.W. Sheng, M.J. Kramer, A. Cadien, T. Fujita, M.W. Chen, Highly optimized embedded-atom-method potentials for fourteen fcc metals, Phys.Rev.B, 83 (2011) 134118.
[92] B.R. Brooks, R.E. Bruccoleri, B.D. Olafson, D.J. States, S. Swaminathan, M. Karplus, CHARMM -a program for macromolecular energy, minimization, and dynamics calculations, Journal of Computational Chemistry, 4 (1983) 187-217.
[93] D. Bergstrom, J. Powell, A.F.H. Kaplan, The absorption of light by rough metal surfaces - a three-dimensional ray-tracing analysis, Journal of Applied Physics, 103 (2008).
[94] M. Yaghoobi, G.Z. Voyiadjis, Atomistic simulation of size effects in single-crystalline metals of confined volumes during nanoindentation, Computational Materials Science, 111 (2016) 64-73.
[95] K. Xiong, H.M. Lu, J.F. Gu, Atomistic simulations of the nanoindentation-induced incipient plasticity in Ni_3Al crystal, Computational Materials Science, 115 (2016) 214-226.
[96] B.N.J. Persson, O. Albohr, U. Tartaglino, A.I. Volokitin, E. Tosatti, On the nature of surface roughness with application to contact mechanics, sealing, rubber friction and adhesion, Journal of Physics-Condensed Matter, 17 (2005) R1-R62.
[97] S. Hyun, L. Pei, J.-F. Molinari, M.O. Robbins, Finite-element analysis of contact between elastic self-affine surfaces, Physical Review E, 70 (2004).
[98] J.P. Ewen, S. Echeverri Restrepo, N. Morgan, D. Dini, Nonequilibrium molecular dynamics simulations of stearic acid adsorbed on iron surfaces with nanoscale roughness, Tribology International, 107 (2017) 264-273.
[99] S. Solhjoo, A.I. Vakis, Continuum mechanics at the atomic scale: Insights into non-adhesive contacts using molecular dynamics simulations, Journal of Applied Physics, 120 (2016) 215102.
[100] S.J. Eder, G. Feldbauer, D. Bianchi, U. Cihak-Bayr, G. Betz, A. Vernes, Applicability of macroscopic wear and friction laws on the atomic length

scale, Physical Review Letters, 115 (2015) 025502.
[101] H.T. Zhu, X. Zheng, P.B. Kosasih, A.K. Tieu, Tribo-surface charge and polar lubricant molecules on friction and lubrication under multiple 3D asperity contacts, Wear, 332 (2015) 1248-1255.
[102] P. Spijker, G. Anciaux, J.-F. Molinari, Relations between roughness, temperature and dry sliding friction at the atomic scale, Tribology International, 59 (2013) 222-229.
[103] S. Solhjoo, A.I. Vakis, Definition and detection of contact in atomistic simulations, Computational Materials Science, 109 (2015) 172-182.
[104] P.R. Nayak, Random process model of rough surfaces, Journal of Lubrication Technology, 93 (1971) 398-407.
[105] B. Bhushan, A. Majumdar, Elastic plastic contact model for bifractal surfaces, Wear, 153 (1992) 53-64.
[106] J.J. Wu, Characterization of fractal surfaces, Wear, 239 (2000) 36-47.
[107] C. Borri, M. Paggi, Topology simulation and contact mechanics of bifractal rough surfaces, Proceedings of the Institution of Mechanical Engineers Part J-Journal of Engineering Tribology, 230 (2016) 1345-1358.
[108] J. Bae, I.J. Lee, A bifractal nature of reticular patterns induced by oxygen plasma on polymer films, Scientific Reports, 5 (2015) 10126.
[109] G. Palasantzas, Roughness spectrum and surface width of self-affine fractal surfaces via the k-correlation model, Physical Review B, 48 (1993) 14472-14478.
[110] M. Pelliccione, T.-M. Lu, Evolution of thin-film morphology, Springer, (2008).
[111] M.P. Allen, D.J. Tildesley, Computer simulation of liquids, Clarendon Press, (1989).
[112] J.M. Haile, Molecular dynamics simulation: elementary methods, Wiley, (1992).
[113] http://lammps.sandia.gov/doc/fix_nh.html.
[114] E. Polak, G. Ribiere, Note sur la convergence de méthodes de directions conjuguées, Revue Francaise D Informatique De Recherche Operationnelle, 3 (1969) 35-43.
[115] I. Amidror, Scattered data interpolation methods for electronic imaging systems: a survey, Journal of Electronic Imaging, 11 (2002) 157-176.
[116] E.S. Gadelmawla, M.M. Koura, T.M.A. Maksoud, I.M. Elewa, H.H. Soliman, Roughness parameters, Journal of Materials Processing Technology, 123 (2002) 133-145.
[117] C.V. Nguyen, K.J. Chao, R.M.D. Stevens, L. Delzeit, A. Cassell, J. Han, M. Meyyappan, Carbon nanotube tip probes: stability and lateral resolution

in scanning probe microscopy and application to surface science in semiconductors, Nanotechnology, 12 (2001) 363-367.
[118] M.R. Brake, An analytical elastic-perfectly plastic contact model, International Journal of Solids and Structures, 49 (2012) 3129-3141.
[119] L. Kogut, I. Etsion, Elastic-plastic contact analysis of a sphere and a rigid flat, Journal of Applied Mechanics-Transactions of the Asme, 69 (2002) 657-662.
[120] R.L. Jackson, J.L. Streator, A multi-scale model for contact between rough surfaces, Wear, 261 (2006) 1337-1347.
[121] http://lammps.sandia.gov/doc/pair_gromacs.html.
[122] A.V. Verkhovtsev, A.V. Yakubovich, G.B. Sushko, M. Hanauske, A.V. Solov'yov, Molecular dynamics simulations of the nanoindentation process of titanium crystal, Computational Materials Science, 76 (2013) 20-26.
[123] G. Dougherty, Digital image processing for medical applications, Cambridge University Press (2009).
[124] R. Pohrt, V. Popov, M. Heß, Normal contact of rough surfaces, in: Method of dimensionality reduction in contact mechanics and friction, Springer Berlin Heidelberg, (2014) 143-164.
[125] B. Lorenz, Contact mechanics and friction of elastic solids on hard and rough substrates, Forschungszentrums Jülich (2012).
[126] W. Manners, J.A. Greenwood, Some observations on Persson's diffusion theory of elastic contact, Wear, 261 (2006) 600-610.
[127] D. Aarts, M. Schmidt, H.N.W. Lekkerkerker, Direct visual observation of thermal capillary waves, Science, 304 (2004) 847-850.
[128] J.J. Hoyt, Z.T. Trautt, M. Upmanyu, Fluctuations in molecular dynamics simulations, Mathematics and Computers in Simulation, 80 (2010) 1382-1392.

Summary

This thesis presents a number of nanotribological problems investigated by means of classical molecular dynamics (MD) simulations, within the context of the applicability of continuum mechanics contact theories at the atomic scale. Along these lines, three different themes can be recognized herein: measuring the contact area in atomistic simulations, the applicability of continuum mechanics theories for describing nanocontacts, and the topography of rough surfaces at the atomic scale.

First, different methods for measuring the contact area in atomistic simulations are addressed, and a distinction is made between the real and the projected contact area. In one approach, a potential energy cutoff is defined for the detection of non-contacting atoms, whose projection is used for the estimation of the projected contact area. In another approach, the contact energy is measured and quantified as the real contact area. Also, a third approach based on the identification of contacting atoms via a contact distance, which is the method most commonly used in atomistic studies, is investigated. Once contacting atoms are identified, the real contact area can be obtained as the product of the number of contacting atoms and the contact area of an atom. Furthermore, the applicability of the radial distribution function in defining the contacting distance and the contact area of an atom is discussed.

Following the calculation of the contact area, different normal contact problems, namely sphere-on-flat (adhesive and non-adhesive) and rough-on-flat (non-adhesive), are studied. The non-adhesive sphere-on-flat contacts are simulated using, both, non-atomistic and atomistic indenters. The results of the system with a continuous non-atomistic indenter show that Hertzian theory of non-adhesive elastic contacts can describe the indentation response for the elastic and reversible plastic deformations. The investigation of the non-adhesive atomistic spherical indenters, however, shows that, for very shallow indentation depths, a revision of the concept of a contact modulus in Hertzian theory of non-adhesive contacts is required. Moreover, it is found that adhesive contacts deviate from the continuum mechanics theories as soon as a dislocation is generated in the deformed material, even if the plastic deformation is still reversible. Furthermore, the rough-on-flat problem is investigated by comparing the MD simulation results with the well-known Greenwood-Williamson and Persson solutions; while both theories overestimate the projected contact area of the simulated systems, the Persson theory is closer to the MD simulation results, provided that its magnification dependent “diffusion coefficient” is obtained from fitting a double Gaussian

function to the interfacial pressure distribution of the contacting system.

Finally, the surface roughness of pure gold blocks is investigated. Each block is generated with a random topography. Then, the block is equilibrated, and the resulting roughness is studied. The results show that the blocks cannot hold every arbitrarily defined topography, and the high frequency roughness is smoothened as it is thermodynamically unstable. Moreover, it is found that the surface roughness is not sensitive to the crystallographic orientation of the block. The equilibration processes of the rough blocks are carried out at different temperatures, and it is found that the surface roughness of the substrates is temperature-independent for temperatures equal to and lower than forty percent of the material's melting point in the Kelvin scale. Finally, it is shown that the surface roughness of molten blocks can be obtained via atomistic simulations, as well as capillary wave theory.

Samenvatting

Dit proefschrift presenteert een aantal nanotribologische problemen die onderzocht zijn door middel van klassieke moleculaire dynamica (MD) simulaties, binnen de context van de toepasbare continuummechanische contacttheorieën op de atomaire schaal. Hierin kunnen drie verschillende thema's herkend worden: het meten van het contactgebied in atomaire simulaties, de toepasbaarheid van continuummechanische theorieën voor het beschrijven van nanocontacten en de topografie van ruwe oppervlakken op de atomaire schaal.

Om te beginnen worden verschillende methoden voor het meten van het contactgebied in atomaire simulaties behandeld, waarbij een onderscheid wordt gemaakt tussen het ware contactgebied en het geprojecteerde contactgebied. Een eerste benadering is gebaseerd op de potentiële energie van het contactgebied, om zo contactloze atomen te detecteren en het geprojecteerde contactgebied te schatten. Een tweede benadering is gebaseerd op het meten en kwantificeren van het ware contactgebied. Een derde benadering is gebaseerd op het identificeren van in contact staande atomen door middel van een contactafstand, hetgeen gebruikelijk is in atomaire studies. Zodra de in contact staande atomen geïdentificeerd zijn is het mogelijk om het ware contactgebied te bepalen. Deze kan worden benaderd als het product van het aantal in contact staande atomen en het contactgebied van een atoom. Bovendien wordt de toepasbaarheid van de radiale verdelingsfunctie voor het bepalen van de atomaire contactafstand en het contactgebied besproken.

Na de berekening van het contactgebied worden twee normale contactproblemen onderzocht: sphere-on-flat (zowel met als zonder adhesie) en rough-on-flat (zonder adhesie). Het sphere-on-flat contact zonder adhesie wordt gesimuleerd met behulp van zowel atomistische als niet-atomistische indenters. De resultaten van het systeem met een niet-atomistische indenter laten zien dat de Herziaanse elastische contacttheorie zonder adhesie gebruikt kan worden om het elastische en omkeerbare plastische gedrag op het meetpunt te beschrijven. Het gedrag van het atomische meetpunt zonder adhesie laat echter zien dat, voor ondiepe indrukkingen, een herziening van de Herziaanse theorie nodig is. Bovendien blijkt dat contacten met adhesie afwijken van de continuummechanische theorieën zodra er een dislocatie ontstaat in het vervormde materiaal, zelfs als deze plastische vervorming nog omkeerbaar is. Het rough-on-flat contactprobleem is onderzocht door MD simulaties te vergelijken met de bekende Greenwood-Williamson and Persson oplossingen: terwijl beide theorieën een overschatting van het geprojecteerde

contactgebied laten zien, is de Persson theorie beter vergelijkbaar met de MD simulaties. Voorwaarde van deze vergelijking is dat de “diffusie coëfficiënt” is verkregen door een dubbele Gaussian functie te fitten op de drukverdeling op het grensvlak van het contactsysteem.

Als laatste is de oppervlakteruwheid van puur goud onderzocht. Gouden blokken met een willekeurige topografie zijn gegenereerd, waarna aan de blokken de evenwichtsvoorwaarde is opgelegd en de ruwheid onderzocht kon worden. De resultaten laten zien dat de blokken niet elke willekeurige topografie ondersteunen, aangezien de thermodynamische instabiliteit een afvlakkend effect heeft. Verder blijkt dat de oppervlakteruwheid niet gevoelig is voor de kristallografische oriëntatie van de blokken. De evenwichtsvoorwaarde van de blokken is opgelegd onder verschillende temperaturen, waaruit blijkt dat de oppervlakteruwheid van de substraten temperatuur onafhankelijk is voor temperaturen gelijk aan en lager dan veertig procent van de smelttemperatuur in Kelvin. Als laatste is aangetoond dat de oppervlakteruwheid van gesmolten blokken verkregen kan worden via zowel atomistische simulaties als de capillaire golf theorie.

Epilogue

I started my PhD program almost four years ago, but it did take me roughly thirty-two years to reach to the point of writing these lines.

My deepest admiration goes to my supervisors Yutao T. Pei and Antonis I. Vakis for giving me the opportunity to pursue my PhD, and all their kind efforts and guidance through the program. I was the first PhD student of APE group, and also the first one supervised by Antonis. Honestly speaking, I was not sure how things will go on, since this was the first PhD experience in the group, but it turned out to be a productive and enjoyable experience. Also, I thank them for the freedom I was given for exploring different topics, especially hot deformation that is completely different from the topic of this thesis, over which we published a paper together.

Dear Antonis, I am exceptionally pleased to have had you as my daily supervisor. When I started my PhD, I knew nothing about contact mechanics! And you helped and guided me to gain the required knowledge. I was hoping for a smooth journey then, but it was just the beginning! Through our numerous insightful scientific discussions, we proposed new solutions, since some of the popular solutions in the literature were not satisfying. I tried my best, and I hope you also have been happy with our collaboration! I am grateful that your patience, passion, and encouragement have influenced me, both, professionally and personally.

Dear Yutao, you were always available for any discussion and conversation. As our group started to work, we had our own weekly group meetings, in which I learnt a lot from your critical thinking on various problems and projects. It was a pleasure to closely work with you.

A distinctive acknowledge is owed to Claudio de Persis, who was my promoter before the establishment of the APE group. Above that, I really appreciate his constant friendly attitude toward me, especially in our conversations in the lunch time at the Bernoulliborg, where the food could keep us full of awe!

My especial thanks go to the committee members, Erik van der Giessen, Lucia Nicola, and Jean-François Molinari, for proofreading the thesis and suggesting constructive comments.

I extend my heartfelt thanks to Martin H. Müser. You helped me a lot to correctly simulate the problem described in the contact mechanics challenge.

Once the challenge was over and you distributed the first draft among the authors, I was amazed to see how close my results were with the reference solution. Also, thanks for inviting and hosting me as a visiting student in your lab. Although the visit became unexpectedly too short due to the delays on trains, I learnt a lot from our discussions.

Moreover, I thank Ramin Ebrahimi for supervising me on my bachelor's project, over which we published a few papers together. Dear Ramin, thanks for guiding me to take my first steps of becoming a scientific researcher. I also thank Abdolreza Simchi and Hossein Aashuri for showing me the beauty of molecular dynamics simulations. Dear Hossein, I am really grateful for your constant support during my master's project.

Thank you, my dear friends and paranymphs, Pooya and Taraneh. I have not defended, now that I am writing these lines; but, I am sure you will be the best supports during my defense.

I thank all APE group members for their support. Especially, I thank Mark Kamps for translating the summary of the thesis to Dutch, and Ranko Toljaga for proofreading it. Zhen, Jing, Liqiang, and Huatang, thanks for the conversations we occasionally had on different subjects, from our cultural backgrounds to our PhD projects. Ali and Taraneh, it was really a pleasure to meet you. Among all, I acknowledge the time we arranged a late bus to reach Schiermonnikoog! Emad, now that you admit the temperature is good enough to take off our hats, we should arrange some outdoor group activities in the next few months.

Dear Sietse, thank you for helping me on the cluster. Dear Frederika, it was a privilege for me to start my job by being your office mate. Ik heb er goede tijd gehad. Dear Inge and Johanna, thank you for your helps, especially whenever I needed to fill in forms. Also, I thank all of my friends in DTPA, SMS, and other divisions of ENTEG.

Coming to Groningen was my very first time of leaving my homeland. I expected it to be somehow interesting and somewhat scary; but, it was not. It was only interesting! I was so fortunate to meet great people, and make good friends to cheer my life up. Matin, thank you for telling me that I needed a *ghablameh*, and showing me the university. Abraham and Karla, I cannot imagine my time here without your kindness. Elsita, it is hard for me to describe the value of your presence in Winschoterdiep. I had a great time with you and Nicolas in Thessaloniki. Shahrzad, you were, and are, always full of

energy! Thank you for the delicious *Tahchin*, the taste of which will be never forgotten!

As the time went on, I was fortunate to meet Nima and Shaghayegh. I really enjoyed our times, especially our trip to Kiani beach resort, together with Pantea. Thank you, Nima, for all of our conversations that made our eyes filled with tears of laughter. Singing along your guitar playing has always been a great joy, especially when we recorded "*to kaz mehnate digaran bighami, to ke khoshkeli!*" We were exceptionally good at Pandemic, and could not stop playing, even in the Shaghayegh's defense eve! Shaghayegh-e mehraboon, I do not know how to express my thankfulness for having me in your place almost all the time. And *aa khoda*! I never forget our trip to Hamburg with you, Nima, and Sepideh.

Then, the era of Pooya arose! You called me and asked if I want to join for a trip to Brussels, and my answer was "are we leaving today or tomorrow?" And, it was the beginning of our trips. First, we went to explore the areas around the city with our noisy bikes! Then, we went to Hamburg and Thessaloniki with bus and airplane. Then, you got your driving license, and we went to the next level, road trips! *Hamino mikhasti?* We went from Prague to Como, and from Metz to Bratislava. To be honest, I would have never travelled that much, if it was not for the trips I had with you and Neda, in which we were trapped by the great voice of Neda singing "*boti taze ba sharabe kohan!*" Neda, thank you for introducing me to GICA. where I sang in a choir for the very first time, and I found my new friends. Thank you, David, for letting me to join the choir. Leon and Sybren, your voices were my lead on every single note. Then Babak joined the choir, and we performed a number of concerts. Thank you, Babak, for all of our community meetings in your place, where I met a lot of my to-be friends, and also our other conversations on politics, economics, cosmology, subatomic physics, metaphysics, meditation, psychology, sociology, literature, TED-talks, movies, quality versus quantity, and New-Orleans neighborhood! You also joined weekly meetings of our *FarsiReadings* group for a couple of times. Pooya, MohammadReza, Saeideh, and I started the group to sit together and read stories. MohammadReza, with your patience and kindness, it is always a pleasure to talk to you on any topic! Thanks to you and Saeideh, we were introduced to Moaddab and Shahla, Andries and Lineke, and Akbar, who elevated the quality of the meetings. Moreover, Saeideh, I was so thrilled that you liked how I play flute recorder, and decided on learning that; so, we sat and practiced together. Words on music and *FarsiReadings* remind me of Solmaz, who I met first on a Tennis court! Well, I left the game shortly after, but we stayed to be friends. Solmaz, I enjoyed seeing you paint, such that I

bought my first set of water color. Along these lines, I thank Tjardo, Héctor, Bao, and Martin; you are all awesome musicians, and I really enjoyed my unique singing experience in our exclusive band. Also, I thank Setareh, András, and Pouriya. It is always a pleasure for me to listen to the music you play. Pejman. I always enjoy listening to your guitar, and playing the games you bring from the communities outside of Groningen, especially *kalameh dar sabad*, which we played a lot at Pantea's. Pantea, thanks for the memorable evenings at your place, which was full of laughter and Persian food!

Farnoush, thank you for giving me hints on practicing piano, and having me in your place in Marburg. Ati and Pooria, thank you for the time we had together in Barcelona. Reza and Pariya, I never forget that evening that you found out I am that guy in the Zumba classes! Hesam and Zahra, I am waiting for more gatherings in Stadspark. Samaneh, Laaya, Talieh, we had a good time biking around the city. As the sun is shining again, we should do that more often. Hadi and Danial, I enjoyed our time to time conversations. Tjardo and James, thank you for taking my hands, so I could have my very first steps on ice. I got the chance to go for ice skating only two years later, and this time, Vlad, *dadash*, it was you, who patiently taught me how to stand on my own. Thank you for showing me that roundish blue church in Bratislava. Martina, thank you for making me a nice time in Prague.

My friends outside Groningen, you made this journey possible. Omid and Ehsan, we are friends for almost two decades, now. Omid, I am not sure I would have the same story, if you had not found out that we were accepted in Mollasadra high school. Ehsan, I am partly shaped through our long discussions on philosophy. Amir, among all stories of dormitories, I acknowledge the first time we tried to find a ticket to go back to Shiraz, and after a few hours, we could get the very last ones! Marzooli, a big thank is owed to you, for your impact on my social behavior. Sepideh, you showed me the beauty of Tehran. If it was not for you, I would have never stepped in any museum. I got this PhD position because of you, Elnazi. Thanks for letting me know about this position, and having me in your place in Turin.

I also thank the rest of my friends and teachers, whose names cannot be listed here due to the page limit, but whose support was essential for writing these lines.

Aza, thanks for all of our calm and lovely moments, which are hard to describe. It is not due to my limited vocabulary, but the limit of vocabulary itself, that I cannot translate my feelings into words. I am extremely delighted for our conversations in languages of painting, playing and singing, which have made life to be colorful and musical!

While I met all of my friends in different points of my life, Soroosh, Salma, Peiman, and Mehran were there for me from the very first moments. You guys are absolutely the bests. Thank you, Soroosh and Salma, for all laughter we had and have. Soroosh, you taught me how to bike, which is an essential skill for living in the Netherlands! Salma joonam, we should go to Kish island, once more, and take a bus to visit the island, instead of riding flat bikes for 7 hours! Reza, thanks for your liveliness, and shouts of "*Shadi bia!*" Our lovely Sogol is so lucky to have you two. Thanks Mehran, for your constant support. I hope you enjoy your retirement. My deepest appreciation goes to you, Peiman. Thank you for all the things you taught me, from the basic details of daily life to understanding music. No matter where I am, you are always in my heart.

Mamanbozorg, while I was in Shiraz, it was my habit to drop by your house, where you told me stories of *Shah o Parioon* and some memories from your childhood, which amazed me by the details that you could remember. I wish I was by your side when you were leaving. I miss you so much.

And no journey starts without a beginning. Maman, Baba, merci for all you have done. Maman, if I want to name one luck in my whole life, it is being your son. You colored my life with music, painting, photography, poetry, and more. You taught me how to be logically persistent. Baba, you were always reading books. This should be why I always have books around.

It did take me roughly thirty-two years to reach to the point of writing these lines, but it also took billions and billions of years of the universe. So, Thank you! I am so glad of being.

"*Never, oh! Never, nothing will die.*"

(Alfred Tennyson)

30 May 2017

Groningen)